

Aus dem Deutschen Krebsforschungszentrum  
Wissenschaftlicher Vorstand: Prof. Dr. med. Dr. h.c. Michael Baumann  
Kaufmännischer Vorstand: Ursula Weyrich  
Abteilung Medizinische Physik in der Strahlentherapie  
Abteilungsleiter: Prof. Dr. rer. nat. Oliver Jäkel

An abdominal phantom with anthropomorphic  
organ motion and multimodal imaging  
contrast for magnetic-resonance-guided  
radiotherapy

Inauguraldissertation  
zur Erlangung des Doctor scientiarum humanarum (Dr. sc. hum.)  
an der  
Medizinischen Fakultät Heidelberg  
der  
Ruprecht-Karls-Universität

vorgelegt von  
Artur Weidner, M.Sc.  
aus  
Stawropol, Russland

2024

Dekan: Prof. Dr. Michael Boutros

Doktorvater: Prof. Dr. rer. nat. Oliver Jäkel

# Table of Contents

1	Introduction .....	1
2	Material and Methods .....	5
2.1	Image-guided radiation therapy .....	5
2.2	Motion management .....	6
2.3	Requirements and application of phantoms .....	6
2.4	State of the art and science of anthropomorphic phantoms .....	7
2.5	Basic principles of magnetic resonance imaging.....	12
2.5.1	Typical relaxation times for abdominal organs and structures .....	14
2.6	Basic principles of computed tomography .....	15
2.7	Magnetic resonance guided radiotherapy .....	16
2.7.1	EBT3 Films .....	17
2.8	Directional Terms in anatomy .....	18
2.9	Anatomy of the diaphragm.....	19
2.10	Breathing-induced organ motion.....	20
2.11	Abdominal phantom container and motion control.....	22
2.11.1	Linear stage unit .....	23
2.11.2	Programmable logic controller (PLC) .....	24
2.11.3	Motion control of the phantom.....	25
2.11.4	Design of the phantom container .....	26
2.12	Manufacturing of the organ models .....	27
2.13	Phantom filling and assembling.....	32
2.14	Experimental Setup .....	36
2.14.1	Experimental setup overview .....	36
2.14.2	First experimental setup .....	37
2.14.3	Second experimental setup.....	38
2.14.4	Third experimental setup with EBT3 films .....	39
2.14.5	EBT3 film evaluation.....	40
2.14.6	Dose offset determination of the EBT3 films.....	40
2.15	MRI measurements .....	42

2.15.1	Quantitative T1 and T2 relaxation time .....	42
2.15.2	Acquisition of MRI cine measurements.....	44
2.15.3	PACS patient scans and starVIBE 991 MRI sequence .....	45
2.16	Image analysis.....	47
2.16.1	Evaluation of quantitative T1 and T2 relaxation times .....	47
2.16.2	Analysis of breathing data .....	47
2.17	Breathing simulation .....	51
2.18	Contrast stability phantom.....	51
2.19	Evaluation of contrast stability .....	53
2.20	Phantom measurements.....	54
2.21	Calculation of relative organ movement .....	54
3	Results.....	56
3.1	Evaluation of contrast stability .....	56
3.1.1	Long term experiment.....	56
3.1.2	Temporal contrast stability of the organ models .....	58
3.2	Tissue-equivalent values for MRI and CT imaging .....	59
3.2.1	Comparison between the phantom and patient imaging data .....	63
3.3	Evaluation of breathing motion .....	67
3.3.1	Organ motion evaluation of first experimental setup.....	67
3.3.2	Organ motion evaluation of the second experimental setup .....	69
3.3.3	End-to-end test with breathing motion and a liver tumor model.....	76
4	Discussion.....	82
4.1	Long-term experiment.....	82
4.2	Temporal contrast stability of organ models .....	83
4.3	Evaluation of organ models for experiments.....	84
4.4	Comparison between the phantom's MRI and CT imaging data .....	84
4.5	Organ motion of the 1st experimental setup .....	85
4.6	Evaluation of the 2nd experimental setup .....	86
4.6.1	Automatic movement detection using starVIBE 991 sequence.....	87
4.7	End-to-end test .....	88
5	Conclusion.....	90

6	Summary .....	91
7	Bibliography .....	95
8	Appendix .....	103
8.1	List of Publications .....	103
8.2	List of Figures .....	105
8.3	List of Tables .....	107
8.4	List of Abbreviations .....	108

# 1 Introduction

The continuous development and research in medicine and medical technology are improving the diagnosis and treatment of diseases. These new insights lead to the development of novel devices and pharmaceuticals. This results in an improvement in quality of life and a growing life expectancy in general. Cancer, however, was responsible for 10 million deaths in 2019, making it the second major cause of death worldwide (Hannah Ritchie und Max Roser 2023). In Germany, a total of 493,200 people were diagnosed with cancer and 230,223 people died due to cancer in the year 2017 (RKI 2023). Considering these numbers, it becomes clear that it is important to further research and improve the treatment of cancer. Several treatment methods have been established over the years, including chemotherapy, surgery, and radiation therapy, to control and/or cure cancer (curative approach) or to relieve the pain and suffering of patients (palliative approach).

External beam radiation therapy (RT) is a non-invasive method that kills cancer cells through ionizing radiation (either x-rays or particle radiation). The radiation damages the DNA of the cells to stop cancer cell proliferation, resulting in the death of the cells. The tumors become smaller or even disappear completely. The cell-damaging effect of RT is not specific, i.e. healthy tissue cells are also affected. Depending on the degree of damage, however, most healthy tissue cells can repair radiation damage to the DNA more efficiently than cancer cells. Therefore, it is important to know the exact location and size of the tumor in order to generate a treatment plan, leading to a dose distribution that is localized ideally to the tumor volume and spares normal tissue. This is accomplished by immobilizing the patient and different imaging procedures that are able to visualize the tumor and provide information about the surrounding healthy tissue and organs at risk (OAR). For this purpose, three-dimensional (3D) imaging modalities are used, such as X-ray computed tomography (CT) and magnetic resonance imaging (MRI). The generated images are used to identify the tumor and the OAR. After that, an individual treatment plan is generated for every patient by varying the number and shape of beams, the direction and the delivered dose. However, several uncertainties will still be present, such as the patient's positioning or the anatomical changes between two consecutive treatment fractions. These are called inter-fractional anatomical changes. The breathing-induced organ movement, for example, also causes additional uncertainties (intra-fractional changes) for tumors in the lung or the abdominal region, which also have to be taken into account. To compensate for inter-

fractional changes, images are taken prior to the treatment and compared to reference images from the treatment planning. If necessary, the patient's position can be corrected. In addition, MRI may be used to identify the target volume as well as the OARs, as this imaging modality provides significantly better soft tissue contrast than CT (Noel et al. 2015). This procedure is also known as image-guided radiation therapy (IGRT). IGRT can be easily implemented for non-moving targets. Tumors in the thorax, abdominal and pelvic regions, however, are more challenging to treat, as they move due to respiratory motion and peristalsis (Dhont et al. 2020; Korreman 2015). One approach is to add an additional treatment margin around the clinical target volume (CTV) (the so-termed internal target volume, or ITV), in order to cover the CTV at all motion states. This, however, leads to a higher risk of radiation toxicity in the surrounding healthy tissue and more critical in OAR. Consequently, new treatment techniques are being developed, such as adaptive radiotherapy (ART) in combination with IGRT. With the increasing importance of new treatment techniques and newly developed hybrid devices such as combining an MRI scanner and a linear accelerator (MR-Linac), suitable phantoms and validation tools are becoming increasingly more important. Ideally, anthropomorphic phantoms are needed, which provide contrast in multimodal imaging and additionally physiological breathing motions (Kurz et al. 2020). These can be used to develop new treatment methods that consider the organ motion, validate the image processing algorithms that are needed during the adaptive process, and dosimetrically validate the entire treatment, for example, in an end-to-end test. An end-to-end test in medical physics comprehensively assesses the entire imaging and treatment process, from initial acquisition, planning and to final delivery. In radiation therapy, this involves simulating a patient's treatment process, typically using a phantom. It includes CT scan acquisition, treatment planning, machine calibration, patient setup, and radiation dose delivery. The aim is to ensure accurate calculation of radiation doses, precise administration of doses by the treatment machine, and accurate patient setup and alignment

There are already commercial and non-commercial phantoms available, which are, however, either anthropomorphically shaped, multimodal or deformable. The ADAM (Anthropomorphic Dynamic breAthing Model) phantom (Pallotta et al. 2019) is deformable and able to simulate breathing motion but provides only monomodal image contrast. This phantom is used for the evaluation of motion management systems in the CT and is not suitable for MRI, as it contains ferrous materials and does not

provide tissue-equivalent contrast in the MRI (Pallotta et al. 2019). Another example is the ModusQA Phantom (Modus QA 2021). It offers MR (magnetic resonance) compatibility and provides motion management. This phantom is used for quality assurance and, therefore, compartments can be filled with different components. It is also possible to simulate breathing motion. Thus, the phantom does not include any anthropomorphically shaped organ models; it only provides cylindrically shaped organ models. The triple modality 3D abdominal phantom (Model 057A; CIRS Inc.) provides contrast in MRI, CT and ultrasound. It also includes anthropomorphically shaped organ models and is designed to perform image-guided needle insertion interventions but does not provide the possibility of breathing motion simulation. Therefore, phantoms are needed that provide a combination of anthropomorphically shaped organ models, organ motion in a composite and multimodal contrast in CT and MRI. Phantoms that provide those features and are capable of arbitrary breathing motion simulation are especially important for magnetic resonance guided radiation therapy (MRgRT) to investigate, validate and develop new treatment methods in the presence of intra-fractional motion (Thorwarth und Low 2021). The lack of anthropomorphic phantoms that can simulate breathing motion and, at the same time, the highly complex and demanding treatment planning process for such cases, indicates the need for experimental setups of this kind.

The aim of this thesis is to develop a solution that fills this gap. Certain demands were specified for the experimental setup to meet the abovementioned requirements. Consequently, an abdominal phantom is intended to be developed, free from ferromagnetic materials, incorporating anatomically similar organ models, and providing anthropomorphic contrast in both MRI and CT. To achieve these contrasts, an already developed formula (Elter et al. 2021) can be used that makes it possible to adjust tissue-equivalent imaging contrast for both imaging modalities. Next, the multimodal contrast stability needs to be investigated over a period of time to ensure a long-term use. The fabrication of organ models by using 3D printed casting molds ensures reproducibility and additionally allows for the manufacturing of anthropomorphic organ shapes. Furthermore, a motion control that is compatible with MRI and is capable of simulating arbitrary breathing curves in real time is needed. The experimental setup should be able to provide breathing-induced organ motion in a compound and it should be possible to evaluate the motion of each individual organ model. Patient and volunteer data should be considered in order to provide reference

data of different breathing types. To enable the management of organ motion and investigate intra-fractional organ displacement and its influence on tumor displacement, the phantom should facilitate the insertion of different tumor models.

In conclusion, the objective of this thesis is to develop an abdominal phantom that incorporates (i) consistent breathing motion for imaging, (ii) organ motion induced by respiration in a composite structure, (iii) realistic contrast in both MRI and CT scans, (iv) organ models shaped in an anthropomorphic manner, and (v) a motion control unit compatible with MRI. Moreover, this approach involves conducting measurements with a simulated respiratory motion under diverse breathing modalities, e.g., shallow, free and deep breathing utilizing the developed phantom. These measurements should be performed through magnetic resonance imaging (MRI) data acquisition. The subsequent analysis will focus on assessing the respiratory amplitude and the dynamic movement of the organ models. A comparative study with focus on data relevant from scientific studies will be carried out to discern patterns and anomalies. The evaluation encompasses both static considerations, emphasizing the maximum amplitude of movement, and a temporal analysis to measure the motion trajectory of each individual organ over time. In addition to the dynamic assessment, dosimetry measurements will be performed and subjected to comprehensive analysis. The methodology involves the insertion of dosimetric EBT3 films into a liver tumor model. Subsequently, the model will undergo irradiation utilizing the MR-Linac while the phantom undergoes controlled simulated breathing movements.

This multifaceted approach aims to yield insights into the complex interplay between simulated breathing dynamics and organ response. The experimental configuration should be modular, facilitating dosimetry measurements and supporting comprehensive end-to-end studies.

## 2 Material and Methods

This chapter covers a range of essential elements in the field of radiation therapy as well as the methodologies and materials used in this thesis. From the use of advanced techniques like IGRT to ensure precise treatment to strategies for motion management in response to patient and organ motion, this chapter delves into the development of state-of-the-art abdominal phantoms and anthropomorphic phantoms for accurate testing and quality assurance. The fundamentals of Magnetic Resonance Imaging and Computed Tomography are explained, in addition to MRgRT, which offers real-time imaging for improved precision. Gafchromic™ EBT3 film basics are introduced for dosimetry, and the importance of understanding the anatomy of the diaphragm in managing breathing-induced organ motion during treatment is discussed. The experimental setup is explained, featuring the use of Gafchromic™ EBT3 film for irradiation and Magnetic Resonance Imaging for high-quality measurements and an end-to-end test. In-house developed Python algorithms are employed for image analysis. Additionally, a contrast stability phantom is used to maintain contrast stability for all used imaging modalities and to ensure reliability throughout the experiments.

### 2.1 Image-guided radiation therapy

The main goal of radiation therapy is to apply a sufficient therapeutic dose to the tumor while sparing the healthy tissue and the OAR. To accomplish this, information about the size and location of the tumor as well as information about the surrounding tissue needs to be considered. Therefore, several imaging techniques including CT and MRI are used to acquire 3D image data prior to the treatment to localize the target volume and generate a treatment plan on this basis. This procedure allows for a more accurate positioning of the patient and dose delivery to the target. A major advantage of this procedure is that it allows for the treatment of tumors that are located near OAR due to its high precision. While inter-fractional motion can be compensated by imaging before the fraction, intra-fractional motion poses a challenge, since respiratory organ movement during the treatment has to be taken into account. Recently developed devices such as the MR-Linac are providing imaging throughout the treatment in order to take intra-fractional motion into consideration (Henke et al. 2018). In addition, it provides superior soft tissue contrast and, therefore, better distinction between tumor and healthy tissue by using MRI instead of CT. The

different techniques used to manage intra-fractional motion in radiation therapy (RT) are discussed in more detail below.

## **2.2 Motion management**

The challenges that are associated with moving tumors led to the development of methods to counteract these effects or mitigate their effect. Therefore, motion compensation techniques have been developed and established to minimize the dose to surrounding healthy tissue and at the same time to deposit the dose into the tumor volume. Especially tumors located in the lung or the abdominal region, e.g. in the liver, pancreas, kidneys or spleen underlie motion due to breathing (Kim et al. 2007; Keall et al. 2006; Korreman 2015). The adaptive radiotherapy attempts to compensate the organ motion by gating (Jiang 2006) or tracking (Kubiak 2016; Caillet et al. 2017). Gating is accomplished by irradiating the tumor while it is located at a specified position during the breathing cycle; tracking, on the other hand, follows the tumor motion trajectory during the irradiation. Both methods involve coaching the patient to ensure specific and reproducible breathing pattern (Thiyagarajan et al. 2016) and are sometimes combined with the implantation of fiducial markers, which can be visualized by using X-ray imaging (Shah et al. 2013). Patients who suffer from lung cancer often show severe impairments of the lung function and sometimes do not tolerate these techniques. Fiducial markers are implanted surgically near the tumor to provide tracking, but this procedure is invasive and may be associated with pain and even sepsis for the patient (Gill et al. 2012). Recent developments that combine an MRI and a linear accelerator (Linac) in the MR-Linac provide non-invasive monitoring of intra-fractional organ motion by means of real-time imaging during the treatment. A continuous image acquisition during the treatment allows for precise gating or tracking of the tumor, without fiducial markers.

## **2.3 Requirements and application of phantoms**

Phantoms in general are used to mimic specific parts of the human body and/or to evaluate different irradiation techniques (DeWerd und Kissick 2014b). Basic quality assurance phantoms that are supposed to be used daily for dose measurements are kept geometrically simple. They provide the possibility to insert ionization chamber dosimeters to measure the dose and investigate corrections to the dose application, if necessary. Since the field of radiation therapy is still developing and various improvements in the past few years have resulted in a higher accuracy and new

treatment methods, the development of medical phantoms has also evolved rapidly. Furthermore, imaging technologies have been improving and the evaluation of new imaging methods for IGRT (like MRI) is becoming more difficult with simple and non-anthropomorphic phantoms, as these approaches neither provide organ-like shapes nor anthropomorphic contrast. Anthropomorphic phantoms can provide an experimental setup with suitable contrast in the imaging modalities and, by choosing a design that mimics human anatomy, it can be comparable to a patient. Phantoms can be used to simulate respiratory motion and provide improvement in IGRT (Kostiukhina et al. 2017). That is why the need for anthropomorphic and realistic phantoms is increasing, since they offer a high potential for the evaluation, analysis and validation of advanced treatment workflow procedures (Filippou und Tsoumpas 2018; Tino et al. 2019).

Their intended use varies depending on the area of application. Dosimetry phantoms, for example, are used to validate treatment plans, dose distribution and their dosimetric accuracy. Additionally, dosimetry studies can be combined with a simulation of physiological changes during different treatment fractions in order to investigate how, e.g., the filling of the bladder influences the dose administered to the prostate, depending on the bladder's filling grade (Niebuhr et al. 2019). In this case, the phantom does not only mimic the desired physiological properties but also provides realistic physical properties, like tissue-equivalent electron density, in order to calculate a treatment plan. Anthropomorphic phantoms provide the possibility to apply actual beams and evaluate the applied dose in order to verify the dose exposure of healthy tissue or OAR. Not only the dose delivery techniques but also the accompanied imaging techniques need validation, as they are used in the IGRT. Phantoms can be used to simulate breathing motion in order to assure the quality of the imaging devices or test new technologies (DeWerd und Kissick 2014b). To ensure that, phantoms should be able to provide (i) multimodal contrast and be reusable, (ii) anthropomorphic shapes of the desired organs and regions (iii) breathing induced motion of organs in a composite.

## **2.4 State of the art and science of anthropomorphic phantoms**

As outlined in the introduction, phantoms that provide a combination of anthropomorphic shape, multimodality, deformability or the possibility to simulate breathing motion have already been developed. However, none of these phantoms provide a combination of all of these requirements at the same time. These phantoms

are either commercially available or have been published in scientific journals. Additionally, some phantoms allow for dosimetric measurements. One of these already established anthropomorphic phantom is the Alderson Radiation Therapy Phantom (RSD Breathing Phantom 2024) (Fig. 1 A, B). It has already been used for over 30 years for different dosimetry studies. Many studies have been conducted based on this phantom, specifically the commercially available dynamic breathing phantom from Radiology Support Devices, Inc. The phantom represents the human thorax region with skin, ribcage, spine and lungs (Testphantom für Strahlentherapie - RS-1500 - Radiology Support Devices - Oberkörper 2024). The material used is tissue-equivalent and provides attenuation coefficients that correspond to human tissue. Additionally, an electro-pneumatic motion controller can simulate tumor motion inside the lung. It also makes it possible to program different motion patterns and breathing rates in order to precisely plan individual treatments of patients.

Another phantom that provides anthropomorphic internal organs and motion is the polyvinyl alcohol (PVA) liver phantom (Jong et al. 2019) (Fig.2 C). It consists of a 3D printed ribcage, PVA supporting abdomen and a PVA liver. An actuator is responsible for sinusoidal breathing motion, and the liver model is moved inside the ribcage (Jong et al. 2019).

The deformable abdominal phantom presented by Matrosic et al. (Matrosic et al. 2019; Matrosic et al. 2020) (Fig. 2 A) aims for the validation of real-time image guidance and provides a setup for a deformable 3D dosimeter. The phantom consists of an acrylic outer shell with an insert made from polyvinyl chloride plastisol (PVCP). Recesses have been designed to allow the insertion of deformable 3D dosimeters. A programmable motion stage and a plunger are used to perform deformation. Nevertheless, this phantom only provides simple geometrical shapes of organ models, for example, a sphere as a liver model or a square like geometry to mimic the spine.

Another phantom is the anthropomorphic abdominal phantom for deformable image registration (Liao et al. 2017) (Fig. 2 B, C). The outer shell is made from a deformable gel that encases a liver, spleen, stomach, left and right kidney, a spine and two tumor models. Additionally, two ionization chambers can be inserted into the phantom. The deformation is accomplished by means of four connected blood pressure cuffs that are wrapped around the phantom and generate a surrounding pressure to induce deformation (Liao et al. 2017). The organs as well as the outer shell provide contrast

and equivalent Hounsfield unit (HU) values in the CT. Nevertheless, this phantom is not suitable for MRI due to the fact that it does not provide tissue-equivalent contrast and contains ferrous materials.

New emerging techniques such as the MR-Linac and the MRgRT offer excellent soft tissue contrast and real-time imaging in order to apply precise doses. Therefore, phantoms should also provide equivalent contrast for MRI and should be capable of simulating breathing motions as well as breathing-induced organ motion to test new techniques and provide further developments.

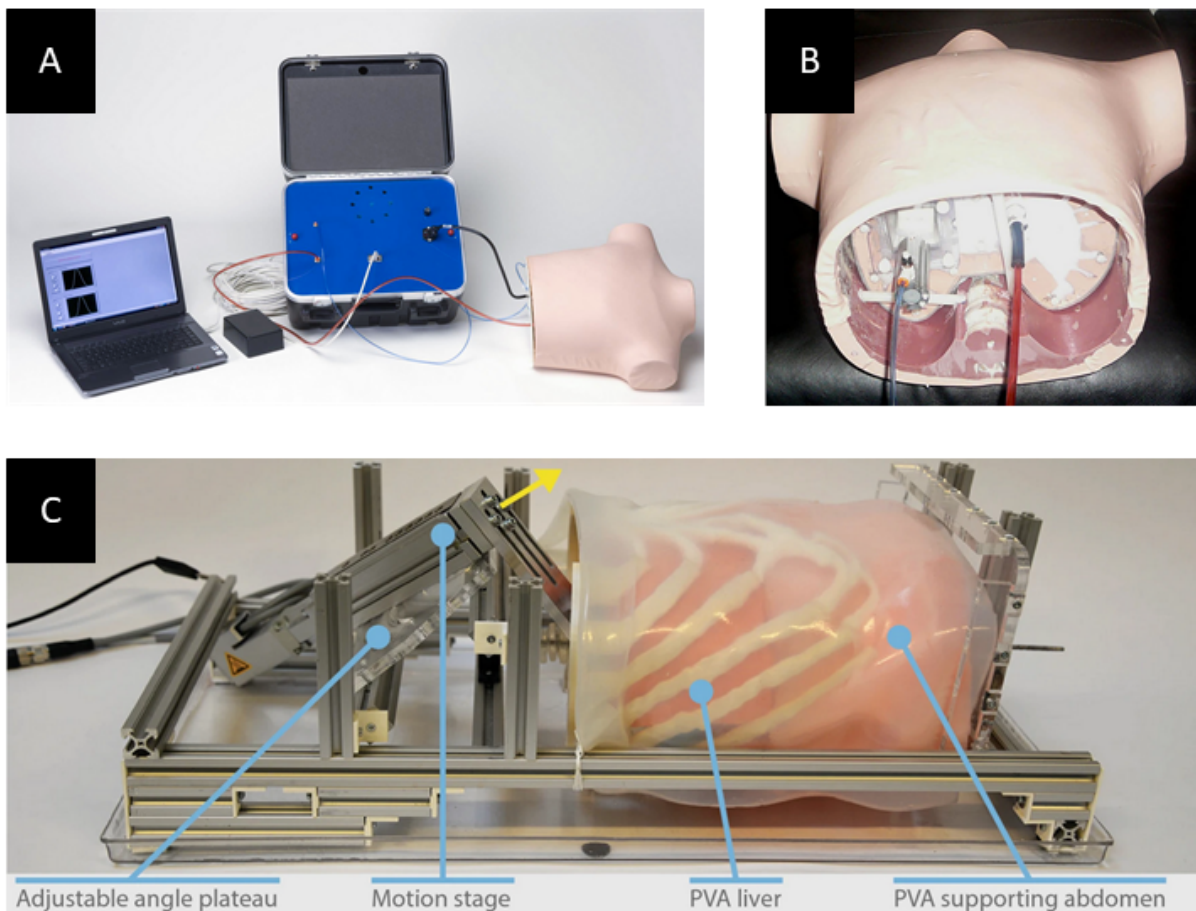


Figure 1: Anthropomorphic phantoms: (A) shows the Alderson Radiation Therapy Phantom experimental setup. The inside of the phantom's thorax is shown in (B) (RSD Breathing Phantom 2024). The polyvinyl alcohol liver phantom and its motion stage is shown in (C) (Jong et al. 2019).

However, there are also phantoms available that are compatible with MRI, such as the ModusQA Phantom (Modus QA 2021). Breathing motion is implemented by means of a piezoelectric motor and the phantom can be filled with components to serve different needs for imaging. The linear stage is capable of motions  $\pm 20$  mm along the z-axis.

Additionally, non-linear motions such as customized trajectories and rotation are possible. For instance, the phantom only provides cylindrically shaped fillable components that can be moved and no organ shapes or any anthropomorphic abilities.

The triple modality 3D abdominal phantom (CIRS 2021) (Model 057A; CIRS Inc.) is not only compatible with MRI, CT and ultrasound but it also contains anthropomorphic organ shapes. The outer casing is made of plastic. The phantom comprises a liver, partial kidneys, an abdominal aorta, a spine and ribs. Additionally, six lesions are located in the kidneys and the liver. A peritoneum made of flexible silicone allows for ultrasound examinations. This phantom is used for applications such as imaging protocol developments, image fusion or biopsy insertions. However, it lacks the possibility to provide breathing motion.

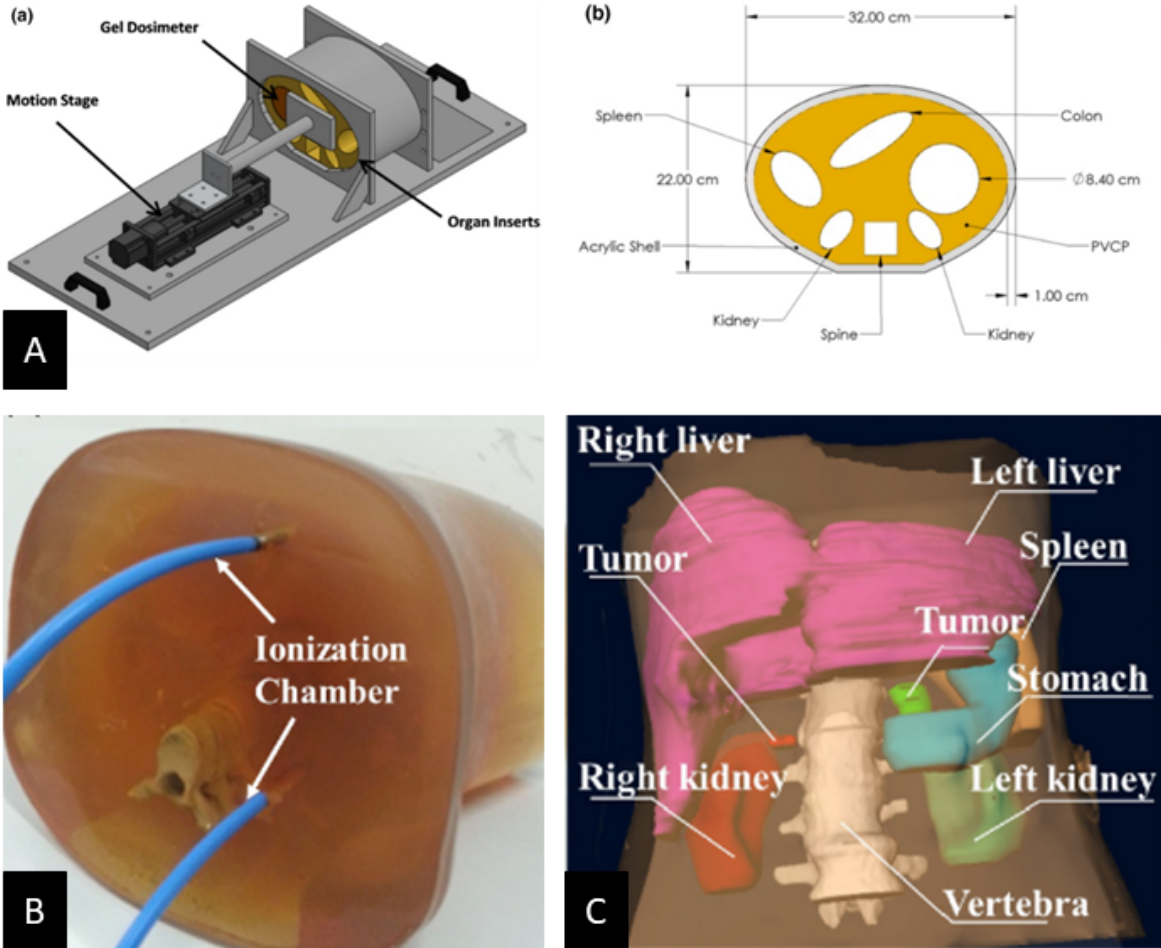


Figure 2: Construction image of the deformable abdominal phantom with its motion stage is shown in A (a). An axial cut through the abdominal phantom demonstrating the geometrical shapes that represent the organ models is shown in A (b) (Matrosic et al. 2019; Matrosic et al.

2020). The deformable phantom with two ionization chambers inserted into the phantom's outer shell, which is made of deformable gel, is shown in B. In C, the segmentation is represented with the corresponding labeling of the individual organs that are housed inside the phantom (Liao et al. 2017).

In conclusion, a number of phantoms have already been developed that provide an experimental setup for dosimetry, validation of real-time imaging, treatment plan validation and imaging protocol development. However, these phantoms provide either only one or a combination of some of the desired properties or are compatible with only one imaging technique. Therefore, there is a need for anthropomorphic phantoms that are capable of reproducible breathing motion simulation, organ-equivalent multimodal contrast and MR compatibility. The aim of this thesis is to provide an abdominal phantom with reproducible breathing motion, respiratory induced organ motion in composite, stable contrast in MRI and CT, anthropomorphically shaped organ models and a motion control unit that is compatible with MRI. The experimental setup should be modular in order to allow for different dosimetry measurements in the future and end-to-end studies.

Table 1: Comparison between different phantoms and their properties.

<b>Phantom</b>	<b>Alderson RSD Breathing Phantom (Fig. 1 A, B)</b>	<b>PVA Liver Phantom (Fig. 1 C)</b>	<b>Deformable abdominal phantom (Fig. 2 A)</b>	<b>Anthropomorphic Abdominal Phantom (Fig. 2 B, C)</b>
<b>Anatomical body parts</b>	Human thorax	Rib cage, liver	Abdomen with simple organ shapes	Liver, spleen, stomach, left and right kidney, a spine and two tumor models
<b>Breathing motion</b>	Different motion patterns	Sinusoidal breathing	Programmable motion	Deformation accomplished by means of blood pressure cuffs
<b>Tumor / Dosimeter</b>	Tumor in lung with motion	Not applicable	3D dosimeter insertion	2 ionization chambers
<b>Equivalent HU values for CT</b>	Yes	Yes	Yes	Yes
<b>MRI compatible</b>	No	No	No	No

## 2.5 Basic principles of magnetic resonance imaging

Magnetic resonance imaging is a tomographic imaging modality without ionizing radiation that provides excellent contrast of soft tissue. For that reason, it is used in applications such as the imaging of brain tumors and the abdominal region (Reiser et al. 2008). The basic principle of MRI is based on the interaction of nuclear spins in the presence of an external magnetic field  $B_0$ . The spins align either parallel or antiparallel to  $B_0$  and, based on the Boltzmann distribution, the number of spins in parallel direction exceeds the number of spins in antiparallel direction. This energetically favorable alignment results in a small measurable net magnetization  $M_z$ . In the

equilibrium state, the spins are not completely aligned with  $B$  but precess around  $B_0$  with the Larmor frequency  $\omega_0 = \gamma \cdot B_0$ . To measure the net magnetization, a radiofrequency (RF) pulse with the Larmor frequency  $\omega_0$  is applied perpendicular to  $B_0$  and causes the net magnetization to rotate towards the  $xy$ -plane. In the transversal  $xy$ -plane, the magnetization starts to decay and induces a current, which can be measured with a receiver coil. There are three different processes that drive this decay process: the spin-lattice, the spin-spin interaction and the local field inhomogeneities of the  $B_0$  field. The first process causes the spins to return to their equilibrium state, whereas the second and third lead to a dephasing of the spins in the transversal plane. All processes are characterized by specific and material dependent relaxation times  $T_1$ ,  $T_2$  and  $T_2^*$ , respectively. This opens up the possibility of modifying RF pulses in their length, power and direction to achieve a variety of image contrasts. The  $T_1$  relaxation time is also described as the longitudinal or spin-lattice relaxation and indicates the time that is necessary for the longitudinal magnetization  $M_z$  to reach 63% of its equilibrium value  $M_0$  after a  $90^\circ$  pulse:

$$M_z / M_0 = 1 - e^{-\frac{t}{T_1}} \quad (1)$$

The  $T_2$  or spin-spin relaxation time specifies the time after which 37% of the signal of the  $M_{xy}$  magnetization is still present after a  $90^\circ$  pulse:

$$M_{xy} / M_0 = e^{-\frac{t}{T_2}} \quad (2)$$

The  $90^\circ$  pulse leads to a synchronization of the spins in all spin packets. Therefore, all spins are in phase after the initial excitation of the  $90^\circ$  pulse and precess around  $B_0$  with the Larmor frequency  $\omega_0$ . Immediately after the excitation, different effects start and lead to a dephasing of the spins, causing a  $T_2$  decay and thus a reduction of  $M_{xy}$ . All spins within one packet precess with the same Larmor frequency, whereas the spins of a different spin packet rotate with a slightly different Larmor frequency. This leads to the fact that some spin packets start to precess more quickly than others, causing the components to dephase, and therefore results in a decrease of the transverse  $M_{xy}$  magnetization. This effect is described as the local fluctuating magnetic field or spin-spin interaction. Therefore,  $T_2^*$  refers to the effective transverse relaxation time, commonly known as the apparent transverse relaxation time. It accounts for various factors that can contribute to signal decay during the MRI process, including magnetic field inhomogeneities, susceptibility effects, and microstructural variations within the tissue.  $T_2^*$  provides valuable insights into the complex interplay between these factors

and is crucial for understanding and optimizing image contrast and resolution in MRI applications (Hashemi et al. 2018a; Bushong 2003). To acquire 3D image data with the MRI, the abovementioned RF pulses are applied, perturbing the alignment and causing the nuclei to emit radiofrequency signals upon returning to their equilibrium state. Spatial encoding is achieved through a combination of frequency encoding and phase encoding, which allows for the differentiation of signals based on their frequencies and introduces spatial information in two dimensions. Additionally, gradient pulses are employed for slice selection, determining the thickness of the image slices along the third spatial dimension. Through repetition of these steps and the acquisition of multiple 2D slices, each corresponding to a different depth within the imaged volume, a comprehensive dataset is obtained. This raw data undergoes Fourier transformation during image reconstruction, converting it into a detailed 3D representation of the imaged anatomy (Hashemi et al. 2018b). The resulting 3D image, composed of voxels representing small volumes within the object, provides a thorough and informative visualization of internal structures. Post-processing techniques may be applied to enhance the image quality, remove artifacts, and emphasize specific features (Brown et al. 2014). The versatility of MRI allows for the adaptation of imaging sequences and parameters to highlight different tissues or contrast characteristics, offering valuable insights for medical diagnosis and treatment planning.

### **2.5.1 Typical relaxation times for abdominal organs and structures**

In the abdominal region, at a magnetic field strength of 1.5 Tesla, the T1 and T2 relaxation times vary across different tissues. In the liver, T1 values fall within the range of 400-600 ms, while T2 values are approximately 30-60 ms. For the kidneys, T1 ranges between 400-600 ms, and T2 is around 30-60 ms. Skeletal muscles exhibit T1 values of approximately 800 ms, with T2 values ranging from 30 to 40 ms. Fat demonstrates T1 values in the range of 200-300 ms, and T2 values around 80-100 ms. In the spleen, T1 values are typically around 400-600 ms, and T2 values range from 30 to 60 ms. The pancreas generally exhibits T1 values within the range of 400-600 ms, and T2 values of around 30-60 ms. It is important to note that these values are approximate and can be influenced by factors such as individual variability and imaging parameters (Bushong 2003). Additionally, higher magnetic field strengths may lead to different relaxation times.

## 2.6 Basic principles of computed tomography

CT is a diagnostic imaging technique that uses ionizing radiation to acquire 3D, cross-sectional images of an object. A x-ray tube generates x-rays throughout the duration of the scan while an opposing detector measures projection images from different angular directions (Pelc 2014). As the radiation is attenuated by the object or patient, different intensities  $I(L)$  are measured by the detector after the x-ray has traversed the patient along the line  $L$ . The photon energies in CT are in the range from 80 keV up to 150 keV. Due to this energy range, different interactions of photons and tissue may occur. At energies below 30 keV, the energy is transferred predominantly by the photoelectric effect, whereas between 50 keV and 90 keV, both the photoelectric effect and Compton scattering effects contribute equally. In the range between 90 keV and 150 keV, Compton scattering is the dominating effect. Each tissue has a specific linear attenuation coefficient and the corresponding attenuation can be calculated by the Beer-Lambert law:

$$I = I_0 e^{-\mu L} \quad (3)$$

where  $I$  is the intensity of the detected beam,  $I_0$  the initial intensity,  $\mu$  the linear attenuation coefficient of the tissue and  $L$  the intersection length with the object or patient. Note that this equation only holds for homogeneous objects and monochromatic radiation. In general, the linear attenuation coefficient is a function of energy, and the x-ray source emits a polychromatic x-ray spectrum. Initially, image reconstruction results in an image showing the linear attenuation coefficients. In radiology, it is common practice to specify attenuation coefficients relative to water, and the attenuation coefficient is converted to CT values measured in HU:

$$CT_{number} = \frac{\mu - \mu_{water}}{\mu_{water}} \cdot 1000 \text{ HU} \quad (4)$$

In this equation,  $\mu_{water}$  is the linear attenuation coefficient of water. This equation provides two fixed points. The CT value of water is 0 HU, whereas air has a CT value of -1000 HU. The CT values of lung tissue range from -900 HU to -500 HU, as the lung is composed of soft tissue and air. The liver typically falls within the range of 40 to 60 HU, while the kidneys vary between approximately 30 to 50 HU depending on the region (cortex, medulla) for normal renal tissue. The spleen shares similar HU values to the liver, with a range of around 40 to 60 HU. Muscles have a HU range approximately from 0 to 50 HU, influenced by factors such as hydration and

composition. Fatty tissue, characterized by its lower radio density, typically ranges from -50 to -100 HU or lower, reflecting its reduced density compared to other soft tissues.

Bones range from 250 HU to over 1000 HU, especially for cortical bones (Schulthess 2017; Hsieh 2015). The spatial resolution of a CT scanner depends on the focal spot size, the reconstructed detector pixel size and the distance between source and detector, among other things. In order to improve the temporal resolution of a CT and thereby decrease the scan time, a so-termed dual source CT (DSCT) was developed. Instead of just one, these devices are equipped with two x-ray sources and two detectors. This technology offers the advantage of high temporal resolution, which is particularly beneficial for specific scenarios such as imaging during breathing or cardiac motion. For example, using a turbo FLASH sequence, 737 mm per second of imaging data can be acquired (Siemens Healthcare GmbH 2021). Therefore, it is possible to acquire images that are mostly free of motion artifacts, which improves the diagnostic capabilities.

CT is one of the major imaging modalities for the diagnosis and evaluation or preparation of irradiation plans in RT, as it provides the electron density that can be calculated from the HU. However, there are several limitations to this technology, including the poor soft tissue contrast compared to MRI and the exposure to ionizing radiation. Therefore, particularly in IGRT, MRI scanners are increasingly used in addition to CT and especially for real-time imaging during treatment.

## **2.7 Magnetic resonance guided radiotherapy**

As described in the chapter about the basic principles of MRI, MRI offers a great advantage in terms of soft tissue visualization and differentiation. Therefore, the development of magnetic resonance guided radiotherapy emerged. This was initially realized by means of a shuttle system between the Linac and the MRI scanner. (Bostel et al. 2018). However, the two devices must be located in different rooms, which means that the transport path of the patient can lead to uncertainties and anatomical position changes such as organ displacements, which cannot be detected during the treatment. Consequently, a new device was developed by combining a MRI scanner with a Linac. The technical implementation is quite challenging, as a magnetic-field-free area is important to ensure that the Linac functions properly. In 2014, MR-guided irradiation was performed for the first time. This was done using the MRIdian by ViewRay (Mutic

und Dempsey 2014), which consists of a split 0.35 T MR scanner in the form of a double donut. Regarding this device in its center was a rotating ring (gantry) with three Cobalt-60 sources for irradiation. In 2017, the MRIdian was revised, and the Cobalt sources were replaced by an integrated 6 MV Linac (Klüter 2019). Due to the low magnetic field, this results in a low signal-to-noise ratio (SNR). Therefore, MRIdian imaging can be used exclusively for motion tracking, as it is sufficient for determining the position of the tumor and organs at risk but not for diagnostic imaging. In contrast, the Unity MR-Linac (Raaymakers et al. 2009) uses a magnetic field of 1.5 T, which is also common diagnostic MRI devices. For the Unity MR-Linac, the first clinical treatments started in 2017 (Raaymakers et al. 2017). In addition to tracking, the strong magnetic field allows for diagnostic and functional imaging, for example, to investigate the therapeutic response of a tumor via diffusion imaging (Decker et al. 2014). In recent years, dosimetry has played a crucial role in radiation therapy, facilitating the accurate measurement and evaluation of radiation dose distribution.

### **2.7.1 EBT3 Films**

One of the significant advancements in dosimetry is the development of radiochromic films, which are sensitive to ionizing radiation and undergo a measurable change in color upon exposure (Marroquin et al. 2016). Among these films, EBT3 has gained considerable attention due to its high spatial resolution, energy independence, and ease of use. EBT3 films are radiochromic films that are based on the principle of radiation-induced polymerization. They consist of a thin active layer that contains a radiation-sensitive dye embedded in a polymer matrix. When exposed to ionizing radiation, the dye molecules absorb the energy and undergo a chemical reaction, resulting in a change in color. The absorbed dose can be quantified by analyzing the optical density or color change using specialized scanners and image analysis software. The spectral absorption characteristics of EBT3 films and their minimal energy dependence make them suitable for a wide range of radiation energies (Niroomand-Rad et al. 2020). However, the orientation of the film is important for the dose response. It is important to provide a consistent orientation of the films during all measurements in order to obtain reproducible results (Khachonkham et al. 2018).

Accurate calibration is crucial for obtaining reliable dose measurements with EBT3 films. The paper by (Chen et al. 2016) focuses on the calibration and uncertainty analysis of EBT3 films using a commercial flatbed scanner. It provides a detailed methodology for calibrating EBT3 films and evaluates the associated uncertainties,

which are essential for accurate dose determination in clinical applications. The calibration process for EBT3 films involves exposing the film to known radiation doses, scanning the film to measure its optical density, and plotting optical density values against the known doses to create a calibration curve. This curve is then used to accurately determine radiation dose values from optical density measurements in subsequent experiments or clinical applications.

EBT3 films find application in various radiation therapy techniques, including external beam therapy and brachytherapy. The article by (Wen et al. 2016) explores the use of EBT3 films to ensure the quality of stereotactic radiosurgery and stereotactic body radiation therapy. The study demonstrates the capability of EBT3 films to accurately measure high-dose gradients and small field sizes, making them valuable tools for treatment verification.

## **2.8 Directional Terms in anatomy**

In the context to characterize the direction of organs, the term superior describes movement or position towards the upper part of the body or head. For instance, during inhalation, the diaphragm moves superiorly. During exhalation, the diaphragm moves inferiorly. Therefore, the term inferior characterizes movement or a position towards the lower part of the body. When referring to the front of the body, the term 'anterior' is used. For instance, the expansion of the chest wall during a deep breath is described as anterior movement. Conversely, 'posterior' denotes movement or positioning towards the back of the body, as observed during chest wall contraction during exhalation. Similarly, the directional terms 'right' and 'left' are instrumental in characterizing lateral movements. When an organ or structure shifts toward the right side of the body, it is described as moving to the 'right.' Notably, certain phases of the cardiac cycle may involve a subtle shift of the heart to the right. Conversely, 'left' denotes movement or positioning toward the left side of the body. This is particularly relevant to the heart, which is conventionally positioned more to the left side of the chest. These terms facilitate standardized communication in anatomy and clinical contexts.

## 2.9 Anatomy of the diaphragm

In general, respiration is a well-coordinated interplay between muscle contraction and relaxation. During the inspiration phase, the respiratory muscles contract, causing the chest cavity to expand. As the lungs accompany the movement of the thoracic wall, they are expanded. This creates a vacuum and air is inhaled. The most important respiratory muscle is the diaphragm. During expiration, the inspiratory muscles relax and the lungs shrink. The muscular part of the diaphragm is shaped like two diaphragmatic domes: one on each side. The right diaphragmatic dome lies slightly higher than the left one because it rests on the liver in the right upper abdomen. The diaphragm has a small indentation between the two diaphragmatic domes to provide space for the heart and pericardium. The diaphragm consists of two surfaces: a thoracic and an abdominal one. The thoracic surface of the diaphragm is in direct contact with the lungs and pericardium. On the abdominal side, the diaphragm is adjacent to the liver, stomach and spleen. Various structures pass from the thorax through the diaphragm into the abdomen. For this purpose, there are certain openings, commonly referred to as hiatuses, in the diaphragm (Fig. 3). In the context of anatomy, a hiatus is defined as a gap that allows certain structures to pass through it. The largest and most important openings include the inferior vena cava, the descending aorta and the esophagus, through which they pass (Gosling 2008; Drake et al. 2021; Netter 2014).

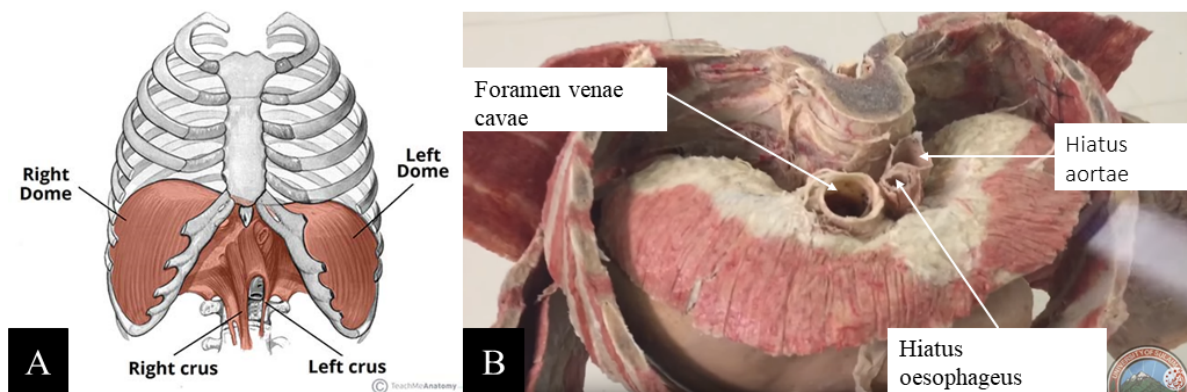


Figure 3: Plastinated diaphragm anatomy (University of Sulaimani / College of Medicine 2017; The Diaphragm - Actions - Innervation - TeachMeAnatomy 2022) : The diaphragm consists of two domes. One lays slightly higher because the liver lies directly under it (A). Moreover, it features various gaps known as hiatus, through which the vena cava, the esophagus, and the aorta pass (B).

Due to the fact that the diaphragm is adjacent to several abdominal organs, such as the liver or spleen, the contraction of this muscle also causes the adjacent organs to

displace. Several studies have been conducted with a focus on breathing-induced abdominal organ displacement. For example, an early study conducted by (Korin et al. 1992) showed an average liver motion of 1.3 cm in superior-inferior (SI) direction for normal breathing. Later studies investigated the breathing-induced abdominal organ motion using four-dimensional (4D) CT images in SI, anterior posterior (AP) and right-left (RL) direction. This study also revealed a significant displacement of liver, spleen and both kidneys (Brandner et al. 2006). Therefore, the breathing motion of the diaphragmatic muscle is responsible for the majority of the organ motion that occurs in the abdomen.

## **2.10 Breathing-induced organ motion**

Respiration is accountable for the primary movement of organs within the human body. The contraction of the diaphragm induces organ motion in the abdomen. Organs and structures adjacent to the diaphragm in particular experience significant displacement. This is also true for the organs below them, as they are shifted by the movement of the organs directly above them and the displacement of the diaphragm. These organs include, e.g., the kidneys and the pancreas. Several scientific studies have already investigated and analyzed the movement of organs in the abdomen. The study by (Kim et al. 2007) analyzed 4D CT scans of nine volunteers in order to evaluate the displacement of the liver dome and its lower tip, the pancreas head and tail, the left and right kidney as well as the spleen, in supine and prone position. The movement trajectory was evaluated in superior-inferior (SI), anterior-posterior (AP) and right-left (RL) direction. In the subsequent chapters of this thesis, only the movement in SI and AP direction will be discussed, as these directions account for the majority of the displacement. The exact values and additional displacement values can be obtained from the cited studies (Tab. 2). In the supine position, the liver dome displays a 15 mm displacement in the SI direction, while the liver tip shows a 12.8 mm displacement. Contrastingly, in the prone position, the liver dome registers a measurement of 12.5 mm, and the liver tip records 10.6 mm, both reflecting reduced magnitudes of displacement. The movement in AP direction for the supine position was 7.4 mm (dome, supine), 1.3mm (dome, prone), 5.3 mm (tip, supine) and 2.0 mm (tip, prone). The liver displacement in the RL direction was minor and amounted to 1.9 mm (dome, supine), 2.4 mm (tip, supine), 1.1 mm (dome, prone) and 1.0 mm (tip, prone). A significant displacement of the pancreatic head in SI direction amounted to 11.6 mm in prone position. For the right and left kidney, values of 13.9 mm and 12.0 mm were

obtained. The displacement of the spleen was 14.1 mm in SI direction. In a further study carried out by (Brandner et al. 2006), the motion of abdominal organs of 13 patients were measured using a 4D CT. All images were acquired in supine position and an average organ displacement across all patients was calculated. The analysis of organ motion showed that the liver has moved 13 mm in the SI direction and 5.2 mm in the AP direction. Similarly, the left kidney has shifted 11 mm in the SI direction and 4.4 mm in the AP direction, while the right kidney has displaced 13 mm in the SI direction and 6.1 mm in the AP direction. The analysis of the spleen motion revealed an average movement of 13mm in SI and 5mm in AP direction. Other studies used cine MRI sequences for the evaluation of organ movement in the abdomen. (Kirilova et al. 2008) measured an average liver tumor movement of 15.5 mm in SI direction, in AP of 10mm and RL of 7.5mm during free breathing. The kidney movement under normal breathing conditions was analyzed by (Moerland et al. 1994) and revealed displacements of 2 to 24 mm for the left and 4 to 35 mm for the right kidney in SI direction. The different organ displacements that were measured in the studies are compiled in table 1.

As shown in the presented studies, respiration and the contraction of the diaphragm significantly affect the organ motion in the abdomen. The displacement of the individual organs reaches up to 15.5 mm for the liver during free breathing, up to 24mm for the right kidney and 35 mm for the left kidney during forced deep breathing, 11.6 mm for the pancreas and 14.1 mm for the spleen. The presented magnitudes represent the SI direction movement, as this direction shows the largest displacement overall. Therefore, it is important to consider the organ motion in the abdomen for MRgRT, especially for newer devices such as the MR-Linac.

Table 2: Organ displacement measured in different studies for liver, right and left kidney, pancreas head and spleen. The measured directions are superior-inferior (SI), anterior-posterior (AP), right-left (RL).

Organ	Liver (Tumor)			Right Kidney			Left Kidney			Pancreas Head			Spleen		
	SI	AP	RL	SI	AP	RL	SI	AP	RL	SI	AP	RL	SI	AP	RL
(Kim et al. 2007)	15	7.4	1.9	13.9	2.3	0.7	12	1.7	1	11.6	2.7	2	14.1	4.4	1.9
(Brandner et al. 2006)	13	5.2	2.1	13	6.1	1.4	11	4.4	1.7	-	-	-	13	6.1	1.4
(Kirilova et al. 2008)	15.5	10.1	7.5	-	-	-	-	-	-	-	-	-	-	-	-
(Moerland et al. 1994)	-	-	-	2-24	-	-	4-35	-	-	-	-	-	-	-	-

As pointed out in the introduction, there is a lack of validation tools, such as phantoms that are capable of simulating physiological organ movement. Consequently, the demand for these phantoms with new findings and new developments in RT is increasing.

## 2.11 Abdominal phantom container and motion control

This chapter discusses the design and functionality of the phantom assembly, the main part of this thesis. The phantom assembly can be broken down into three main parts: the linear stage unit, the hydraulic system and the phantom container. Each of the components is responsible for a specific task. The linear stage unit consists of a stepper motor, a linear stage and a double-acting cylinder that is connected to the linear stage. The motor transmits predefined breathing movements to the linear stage. The latter passes this movement to the double-acting piston. The movement of the piston induces a displacement of the water in the hydraulic tubes of the hydraulic system, and the

breathing movement is transmitted to the diaphragm. This construction makes it possible to transmit predetermined breathing patterns to the phantom's diaphragm, which then transmits the impulse to the organs inside the phantom, resulting in their displacement.

### **2.11.1 Linear stage unit**

This chapter outlines the design and fabrication process of the linear stage unit within the Phantom assembly. The linear stage was designed with a holder for the motor and an adapter for linear stage and the double-acting cylinder (Fig. 4). To ensure precision and efficiency, 3D printing technology was employed to fashion several crucial components using VeryCyan (blue) and VeroClear (light gray) materials. The motor holder, coupling adapter, and the adapter for the linear stage were produced using 3D printing with the materials VeryCyan and VeroClear, lending the structure both durability and flexibility. Additionally, a custom-made adapter plate for the double-acting cylinder was expertly manufactured by the mechanical workshop from high-strength PVC (polyvinyl chloride). This material choice ensures the structural integrity required for the assembly's seamless operation. A NEMA 23 motor (EC Motion GmbH, Germany) with a 3-channel encoder (A) is attached to the motor holder and connected via a coupling (B) to the linear stage (igus® GmbH, Germany) with a 15mm slope and 100 mm length (C). The plunger (D) is fixated on an individually designed plate and embattled to the linear stage. To hold the double-acting cylinder (F) (PSK Ingenieurgesellschaft mbH, Germany), a holding mechanism is fixated with knurled screws so it could be easily attached to the linear stage unit and also quickly detached from it. The double-acting cylinder can be connected to hydraulic tubes via two connections (E) and (G).

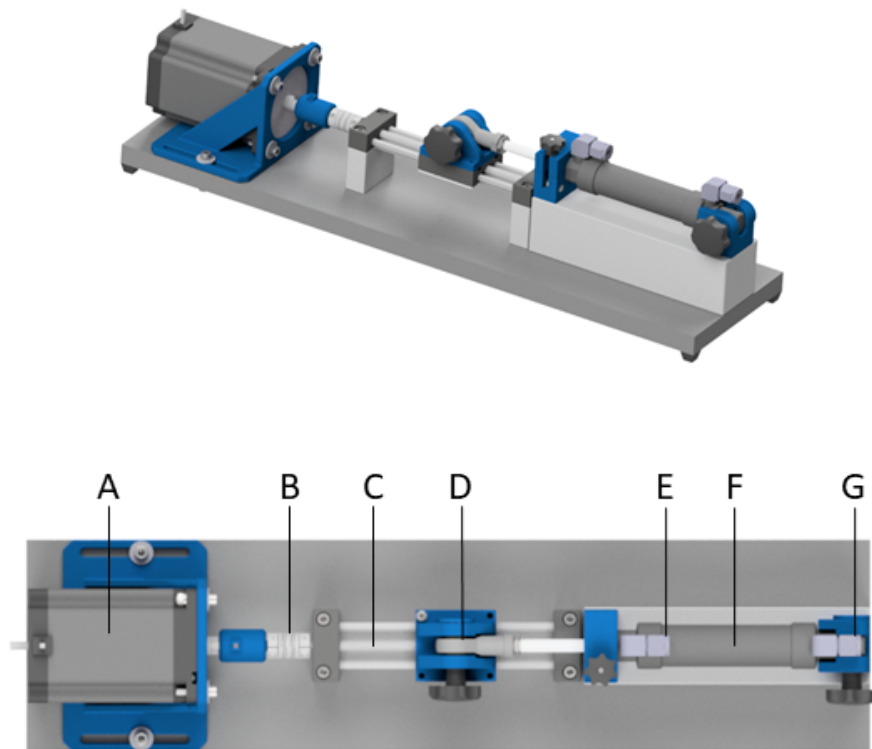


Figure 4: Linear stage unit for motion control. A NEMA 23 motor (A) is connected via a coupling (B) to the linear stage (C). The linear stage holds the plunger (D) of the double-acting cylinder (F), which was connected to the hydraulic system via the hose connection (E) and (G) (Source: Own figure).

### 2.11.2 Programmable logic controller (PLC)

A programmable logic controller (PLC) is a microprocessor-based system by Beckhoff and is commonly used in the automation industry to carry out operations in industrial processes. Therefore, the system has a real-time compliance. In this thesis, a PLC CX2040 (Beckhoff Information Systems, Germany) with an EL5101 Encoder-Interface was used to control and monitor the stepper motor. For the implementation, the structured text programming language in the TwinCat 3 Software environment was utilized. This software environment is integrated into Visual Studio 2010. Three different function blocks (FB) were implemented, including a motor control FB, a main FB and a comma-separated values (CSV) Read FB. In the motor control FB, the axis for the motor was instantiated and the control of the axis set to true. Extra variables allow for executing any desired positional drive of the motor at a specified velocity. A state machine was implemented in the motor control FB, it was called continuously by the main FB in case of issues with the PLC or the motor, and the state would change into

error and reset state. In order to simulate breathing motion, customized breathing functions in CSV format could be loaded in the PLC storage with the CSV Read FB. The CSV file contained two columns: the first column focused on the time, the second column on the position that should be accessed at that specific point in time. This way, the velocity of the motor was calculated individually to reach every desired position at the specified time.

### **2.11.3 Motion control of the phantom**

The linear stage, the PLC, and the hydraulic actuator represent the motion control of the experimental setup. A stepper motor that is located on the linear stage was connected to the PLC through three plug-in connectors. One connector is responsible for the motor power delivery, the next provides the interface between the TwinCat software and the motor in order to control the motor motion and the last one is connected to the encoder, providing feedback on the motor's motion. The stepper motor is located at the front of the linear stage and is connected via a custom-made adapter and a coupling to the linear stage. Next, the plunger of a double-acting cylinder is installed on the carriage, enabling it to move as the motor starts to move. The cylinder, in turn, realizes the connection between the motion control and the phantom via six-meter-long hydraulic tubes. The hydraulic tubes are attached to a second identical double-acting cylinder that is fixated at the top of the phantom. A custom-made adapter was constructed using computer-aided design (CAD) and 3D printing technology. It serves the purpose of securely holding the double-acting cylinder and facilitating its attachment to the phantom.

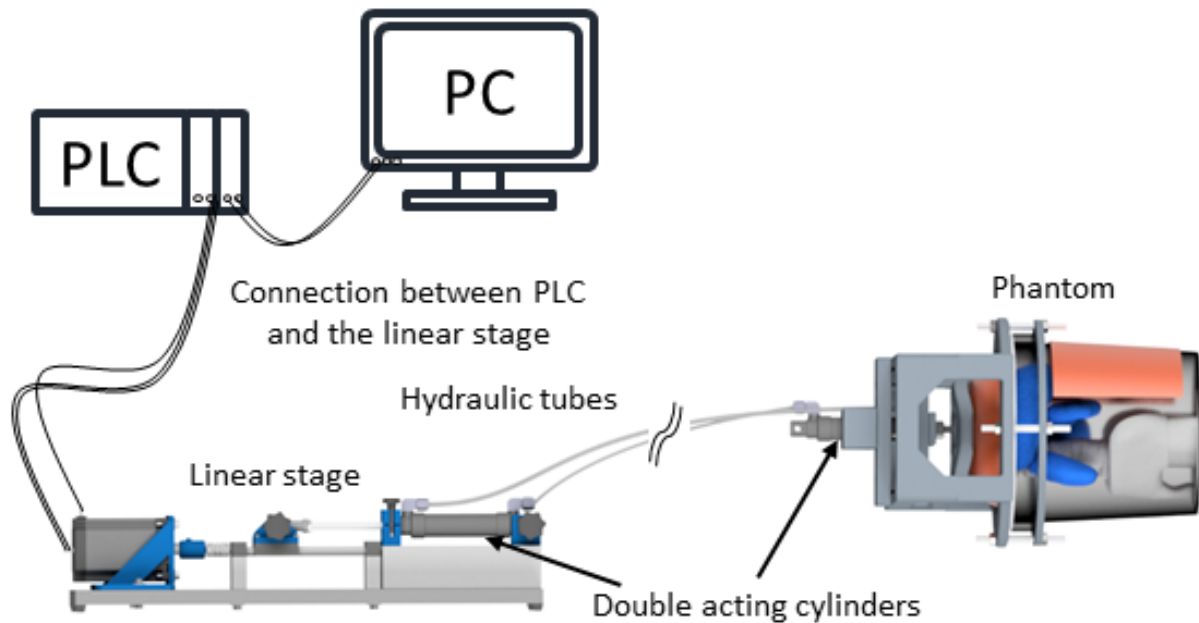


Figure 5: Motion control setup: The PLC is connected to a PC and to the stepper motor. A coupling realizes the connection between the stepper motor and the linear guidance, which is equipped with a linear slide that is attached to the plunger of the first double-acting cylinder. Two hydraulic tubes connect both double-acting cylinders. The second cylinder is fixated at the top of the phantom, and a diaphragm-shaped 3D printed actuator is screwed onto it. This actuator slightly touches the phantom's diaphragm, which is the starting position of every simulated breathing cycle (Source: Own figure).

#### 2.11.4 Design of the phantom container

The abdominal phantom consists of two interlocked cone-shaped polypropylene (PP) containers (E) with a volume of 10 l (Fig. 6 (1)). Cutouts were made both at the ventral and at the cranial surface, and a flexible peritoneum and diaphragm were inserted, respectively. The peritoneum (K) and diaphragm (C) were both manufactured and cast with a tin-free catalysts (TFC) silicone caoutchouc type 6 (Troll Factory Rainer Habekost e.K., Germany) with a shore of A 22 and a thickness of 3 mm. Shore refers to the shore hardness scale, which is a measure of the hardness of a material. Higher shore values (e.g. shore A 70-90, such as rigid plastics or harder rubbers) indicate greater hardness, while lower values (e.g., shore A 10-30, such as flexible rubbers or gels) indicate softer materials. To hold the diaphragm in place and prevent any leakage of agarose, the diaphragm was attached to the lid (J) with two holding frames (D) and (J) using 36 M6 plastic screws. Two frames (H) and (F) were designed to hold the phantom containers together and were additionally used for the positioning

in the MRI as well as for the attachment of the hydraulic system (G). The mount for the double-acting cylinder (A) was designed in such way that it made it possible to adjust the cylinder in x and y position. For that purpose, a millimeter scale to the mount to ensure a reproducible placement of the cylinder (B) and the actuator which was attached to the cylinder via a M10 thread. In order to better visualize the abdominal phantom, a rendering of the internal organ models (Fig. 6 (2)) and the assembled phantom are shown in figure 6 (3).

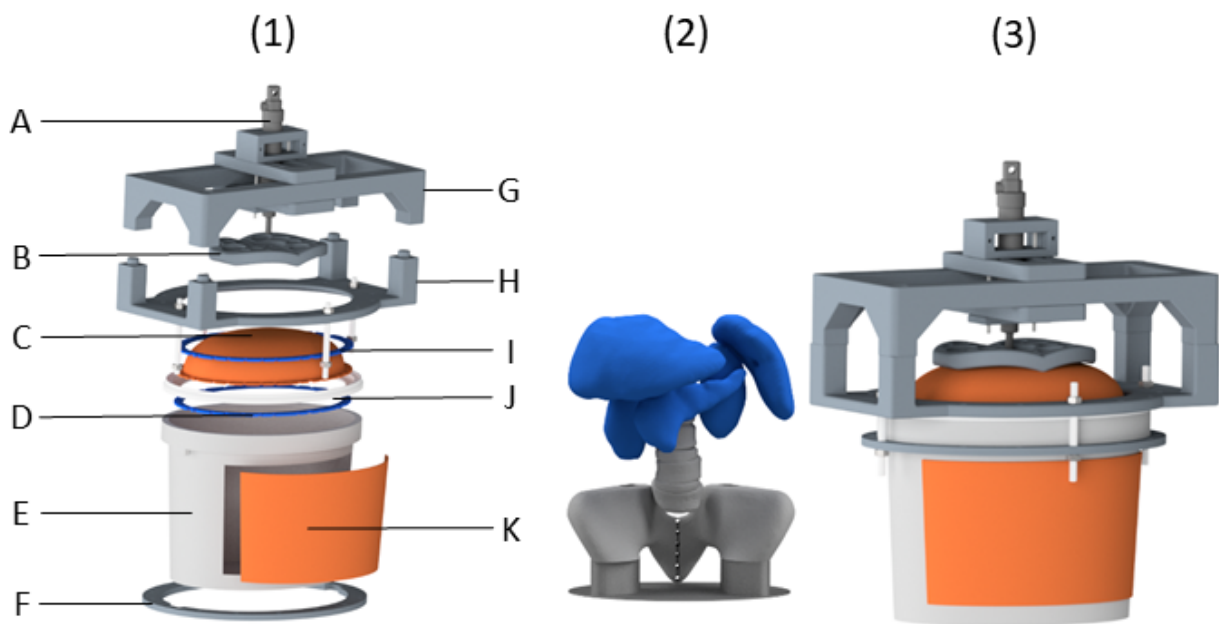


Figure 6: Phantom container and organ models. The phantom container and its individual components are shown in (1). A rendering of the organs inside the phantom (2) for better visualization, and the assembled phantom container with the attachment for the hydraulic system (3) (Source: Own figure).

## 2.12 Manufacturing of the organ models

For the construction of the organ models, different approaches were used. The liver model was created based on a 3D scan of an anatomical liver model; the kidneys, spleen and pancreas were segmented from volunteer MRI digital imaging and communications in medicine (DICOM) data. The spine model was generated from pseudo-anonymized patient CT data retrieved from picture archiving and communication system (PACS). The liver model was scanned with an Artec Eva (Artec Europe) 3D scanner. For this

purpose, the software Artec Studio 9 (Artec Europe) was used to post-process the scanned data. The creation of the DICOM data was carried out with the medical imaging interaction toolkit (MITK). For this, the desired organs, e.g., kidney, spleen and pancreas were segmented in the axial, coronal and sagittal plane. Utilizing an algorithm supplied by MITK facilitated the transformation of segmentation data into a polygonal model. This model was post-processed with Meshmixer (Autodesk, USA), to smooth it and close holes. These processed organ models then served as the basis for the casting molds of each individual organ model, which were constructed using the CAD Inventor Professional 2018 (Autodesk, USA). The casting molds for the organ models were designed with an opening at the top of each mold, allowing for easy filling with a mixture. Moreover, holes were constructed all around in order to lock the mold with screws and prevent the liquid mixture, as this is its state during the pouring process, to escape from the mold. For the creation of the 3D models of the spine and pelvis holding plate, CAD was used as well. Subsequently, all casting molds were 3D printed with the Objet500Pro (Stratasys, USA).

Table 3: Chemical composition of liver, kidney, spleen, pancreas and vertebrae models for magnetic field strengths of 1.5 T and 3 T and equivalent HU values for CT imaging.

	Agarose [g]	Ni-DTPA [g]	KCl [g]	Water [g]	Volume [g]
1.5 T					
Liver	51.67	66.77	21.41	1581.60	1700
Kidney	8.28	10.31	3.32	481.41	500
Spleen	13.12	12.62	12.25	674.63	700
Pancreas	15.24	7.81	19.74	465.02	500
L4 Vertebrae	9.14	23.26	13.06	277.80	300
3 T					
Liver	80.80	30.01	25.57	1589.20	1700
Kidney	10.48	7.89	3.51	481.63	500
Spleen	18.83	12.53	7.86	673.31	700
Pancreas	18.67	9.51	11.6	469.73	500

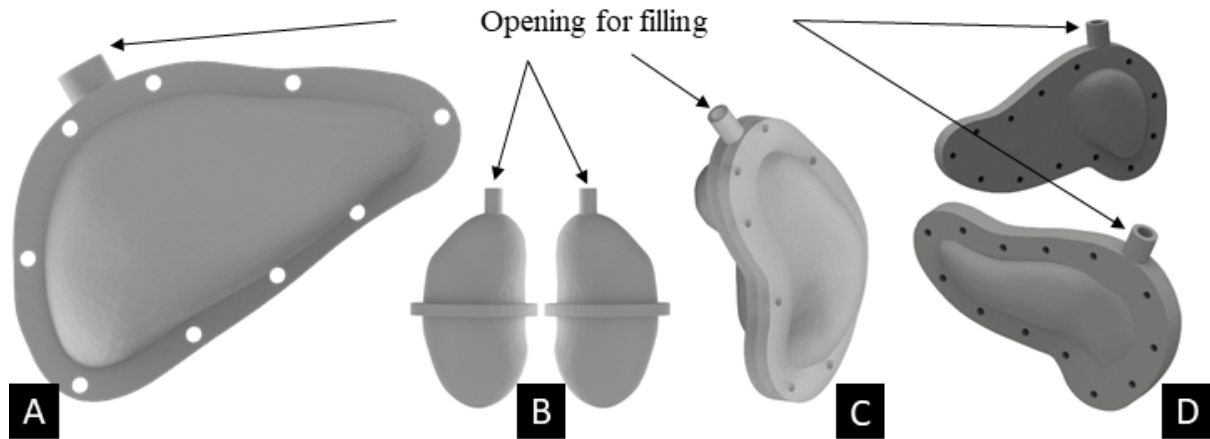


Figure 7: Casting molds were designed with CAD for the liver (A), the kidneys (B), the spleen (C) and the pancreas (C). All casting molds provide an opening for filling and holes in order to lock the casting mold with screws (Source: Own figure).

Next, the casting molds were used to manufacture the organs models from a mixture of agarose gel (Roth Industries GmbH, Germany) doped with Ni-DTPA (DKFZ, Germany) and potassium chloride (KCl) (Carl Roth GmbH & CoKG, Germany). Nickel diethylenetriaminepentaacetic acid (Ni-DTPA) and agarose served as modulators for contrast in MRI (Tofts et al. 1993) and KCl for contrast in CT imaging. First, the quantities of water, Ni-DTPA, agarose and KCl were calculated for each organ model in accordance with (Elter et al. 2021) in order to achieve tissue-specific contrast in MRI at 1.5 Tesla (T), 3.0 T and CT imaging (Table 2).

Subsequent, the beaker containing only the calculated amount of water was placed on a heater, while stirring continuously, and a target temperature of 82° C was set. Then the remaining components were added to the water in the following order: first Ni-DTPA, then agarose and finally KCl. Afterwards, the beaker was covered with aluminum foil to accelerate the heating process while avoiding condensation and a change in volume. After the mixture reached the target temperature of 82° C, the beaker was removed from the heater and placed in a desiccator. As the mixture contained trapped air (Fig. 8 A) due to the viscosity which could not be released by constant stirring, the beaker was placed in a desiccator connected to a vacuum pump (Fig. 8 B). The degassing process occurred in 30mbar steps, starting at 450mbar every 40 seconds to avoid foam formation. As the mixture contains agarose, it becomes more viscous with decreasing temperature. For this reason, it had to be liquefied by heating it up to 80° C. The process of heating and successively degassing was repeated at least three times, until enough air was able to escape and no further air bubbles were visible

(Fig. 8 C). After that, the mixture was poured into the designated casting mold (Fig. 8 D) and stored at 4° C to accelerate the hardening process. After the mixture had solidified, the organ models were removed from the mold, packed, and vacuum-sealed in foil (Caso 1295, CASO Design) (Fig. 8 E).

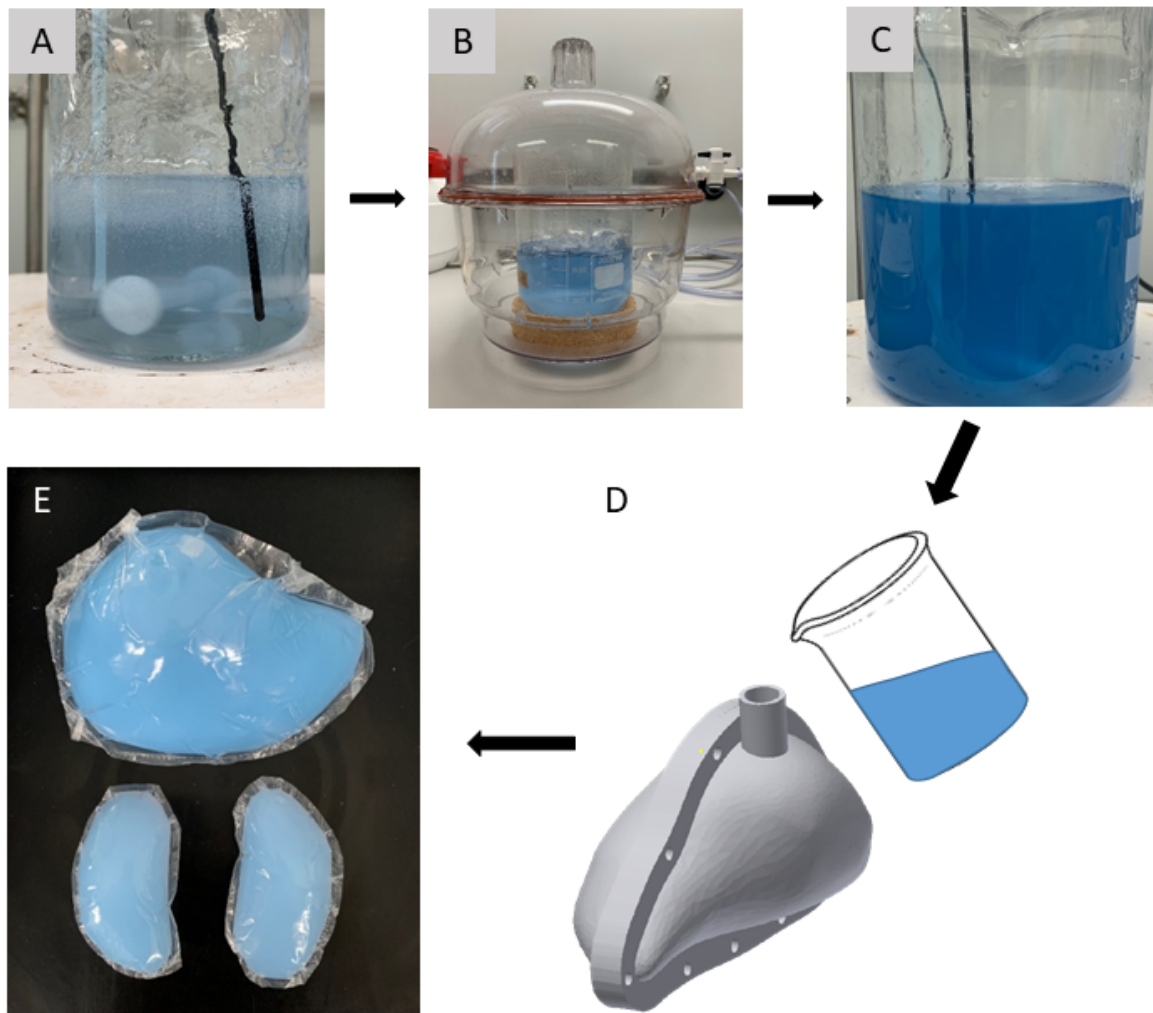


Figure 8: Manufacturing of organ models. Agarose gel mixture doped with Ni-DTPA on a heating plate containing trapped air (A). Beaker placed in a desiccator with a connection to a vacuum pump (B). After degassing and heating three times, beaker shows no visible air bubbles (C). The mixture for the liver was poured into the designated casting mold (D). After the hardening process, the organ model was removed from the mold, packed and sealed under vacuum in foil (E) (Source: Own figure).

The pelvic bone used in this thesis was provided by the ADAM-pelvis phantom, which is described in more detail in Niebuhr et al. 2019. The hollow pelvis was 3D printed (Object 30 pro, Stratasys) using the material VeroClear and filled with a mixture containing 25 wt. %  $K_2HPO_4$  (wt. % = weight fraction in percent of the substitute in

the overall compound) (Niebuhr et al. 2019) and Vaseline 75 wt. % to achieve a CT number range close to the mean values of patient data. Due to its high amounts of calcium, gypsum, which is similar to human bone, it can be utilized to achieve high CT values. Therefore, the outer bone was coated with different layers of gypsum according to Niebuhr et al. in order to provide different attenuation of outer and inner bone regions. As shown in figure 9 A, three layers of gypsum provide a HU value of 300 HU, four of 400 HU and five up to 600 HU at 120kV CT scans. After the gypsum was applied and fully dried, the pelvic bone was covered with a rubber varnish spray to prevent the agarose from mixing with the gypsum. The lumbar spine containing hollow vertebrae L5-L1 and flexible intervertebral discs was manufactured via 3D printing. The 3D printing material VeroClear was used for the vertebrae and the flexible, silicone-like material Agilus 30 with a shore of A 50 was chosen for the intervertebral discs. Next, the hollow vertebrae were filled with an agarose mixture doped with Ni-DTPA in accordance to table 1. Afterwards, the vertebrae were coated with three layers of gypsum in order to achieve a CT number in the range of 300HU, and they were attached to the pelvis via a constructed holder at the L4 vertebra (Fig. 9 A). To ensure consistent and secure positioning of the pelvis and spine model, a custom holder was crafted and attached to the bottom of the phantom container (Fig. 9 B). This procedure provided a homogenous organ surrogate and was important in order to provide anthropomorphic contrast and composition in MRI and CT imaging.

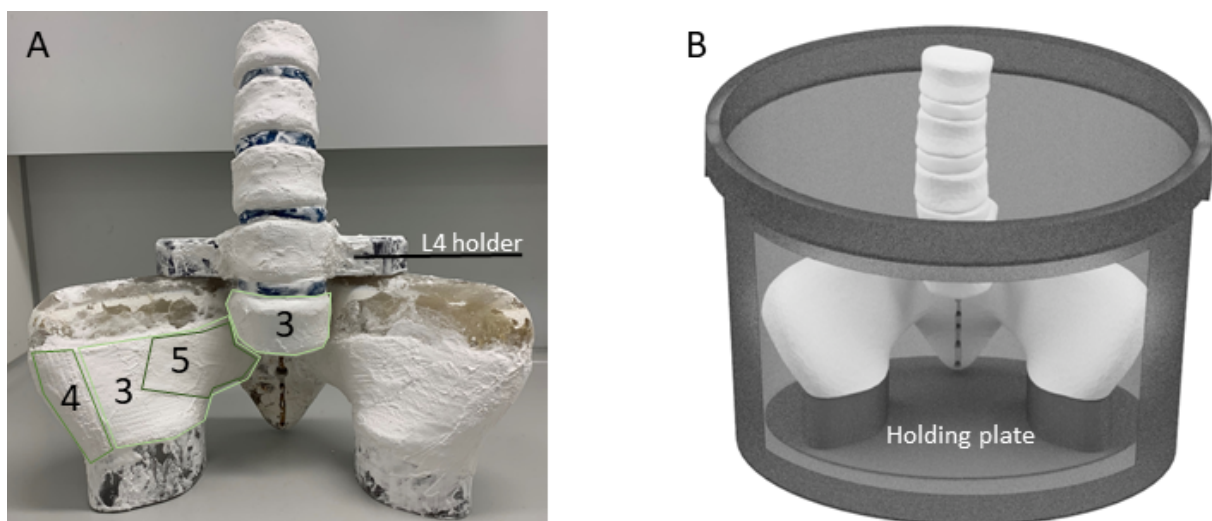


Figure 9: The pelvis with attached lumbar spine model, covered with different numbers of gypsum layers around the pelvic bone model and the vertebrae (A). A rendering of the phantom container and the pelvis fixated to its holding plate (B) (Source: Own figure).

## 2.13 Phantom filling and assembling

First, the pelvic bone with the attached lumbar spine segment were placed in the phantom container (Fig. 10 A). Next, two beakers with a volume of 5 l were heated up to 80° C on a heating plate under constant stirring. The mixture for the surrounding tissue with an agarose concentration of 0.4 % was realized by using 4980g of desalinated water and 20g of agarose. Then the 10 l of agarose were poured slowly into the phantom container to avoid bubble formation (Fig. 10 B).

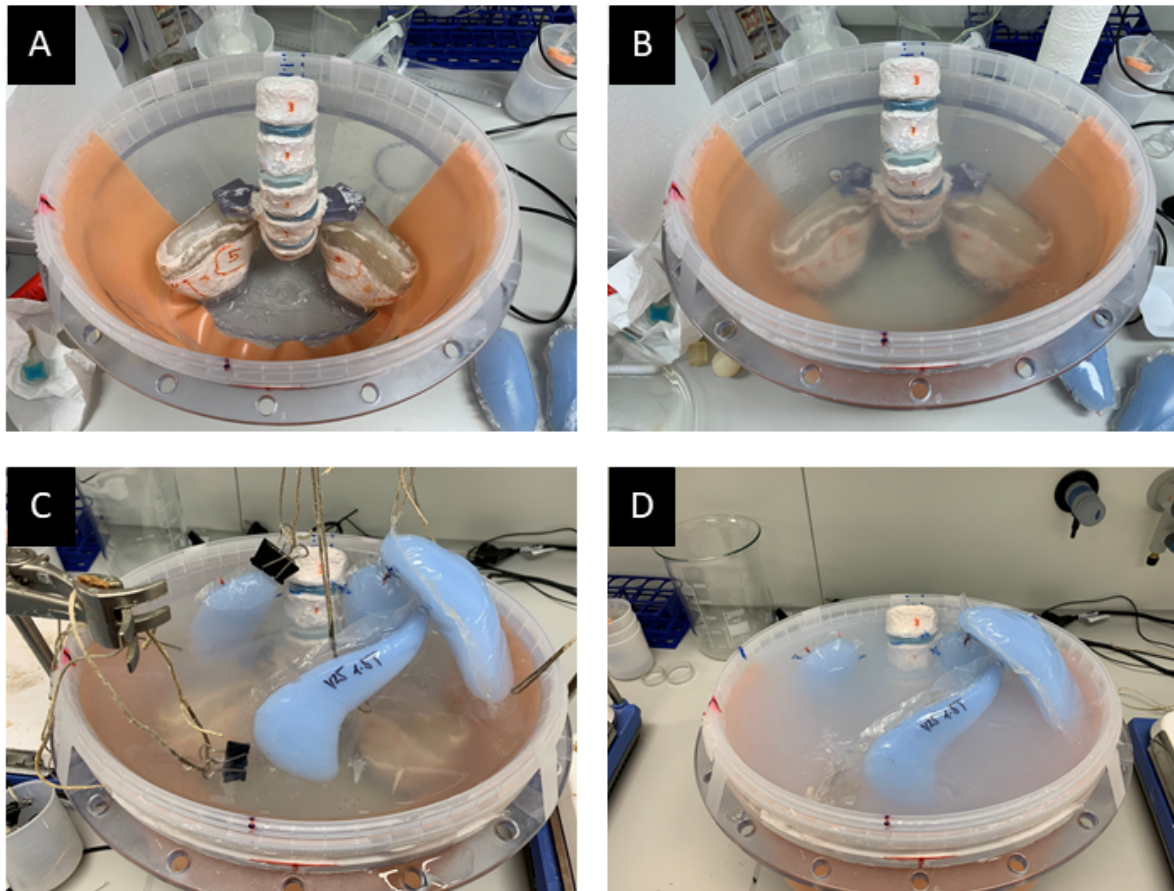


Figure 10: Phantom container filling and organ placement. The phantom container containing the pelvic bone and spine model (A). In (B), 10 l of agarose mixture are surrounding the pelvic bone and parts of the spine model. Additional organ models such as both kidneys, the pancreas and the spleen are placed anatomically inside the phantom as an additional 5 l of agarose mixture are poured inside the phantom container (C). In (D), the phantom container is shown, with the organ models and solidified agarose (Source: Own figure).

Afterwards, the organ models of the left and right kidney, the spleen and the pancreas were attached to a mounting bracket and arranged to their approximate anatomical position (Fig. 10 C). Distinct markings on the organs and inside the phantom container

(Fig. 11 A - E) ensured reproducible placement. After the organ models were arranged, an additional 5 l of agarose mixture were prepared as described and poured slowly inside the phantom container. The phantom was then stored overnight, allowing the mixture to solidify, ensuring that the organ models became securely embedded within the gel matrix (Fig. 10 D). After 24 hours, once the agarose was hardened, one liter of agarose was poured into the phantom and the liver was placed based on distinct markings (Fig. 12 B 3 and 4). This process ensured an accurate organ placement at a distinct position, and the stepwise hardening of the agarose prevented the organs from drifting out of their foreseen position. Finally, the lid with the attached diaphragm was used to seal the phantom. Afterward, the phantom was rotated into supine position and another 2L of agarose were poured into the phantom via two Luer lock openings in the lid (Fig. 12 C). The supine position was defined as shown in figure 13 C.

The kidneys, spleen, pancreas, pelvis and lumbar spine remained the same for all experiments. For the end-to-end test, a new modified liver model that contained a tumor model was designed and manufactured.

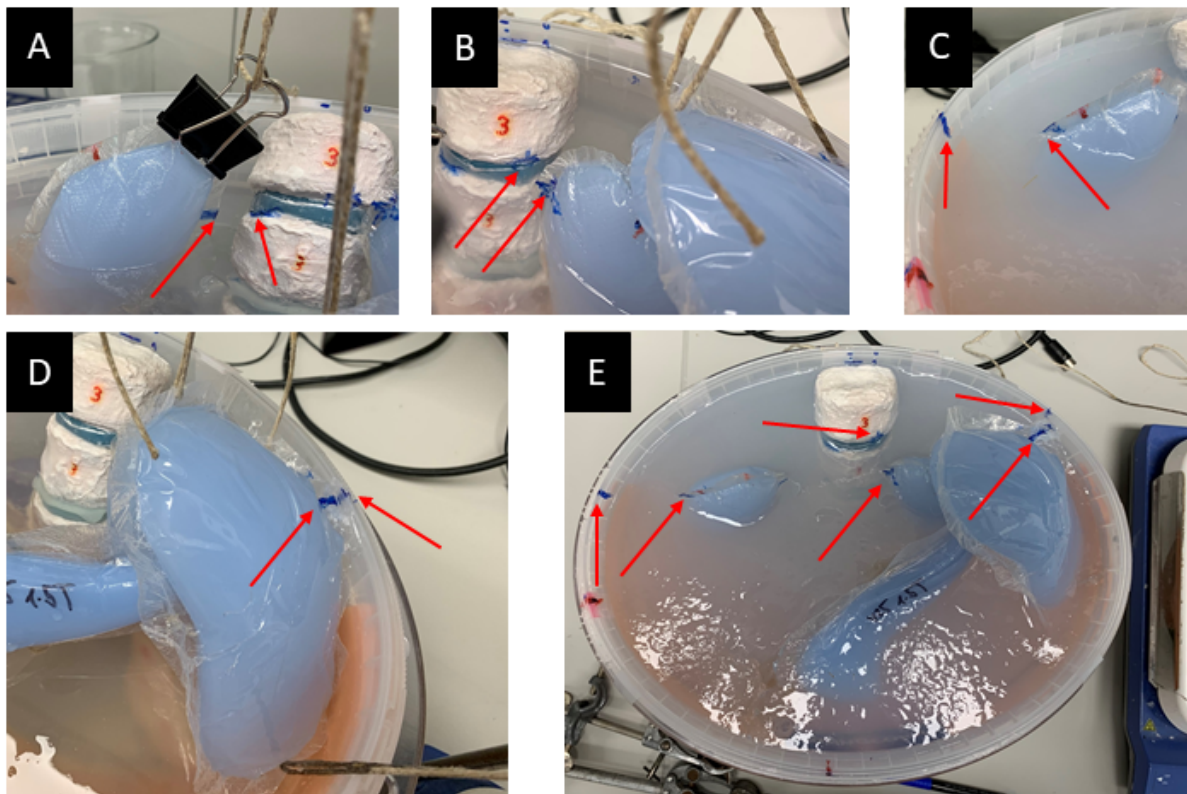


Figure 11: Markings on the organ models and the phantom container. Markings (A-E) ensured a reproducible placement of the different organ models (Source: Own figure).

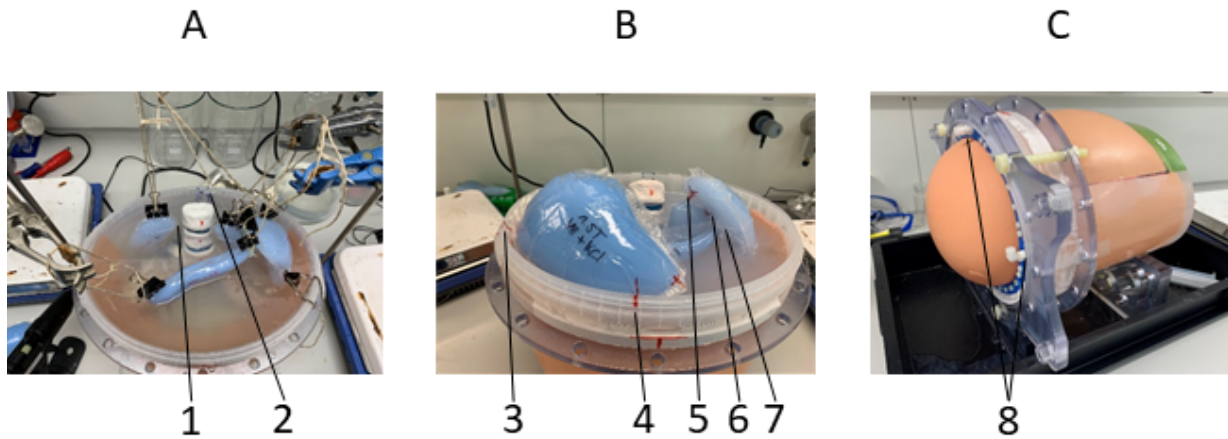


Figure 12: Organ placement: Organ, pelvis and spine models are placed in the phantom, which is then filled with 0.4% of agarose (A). Distinct markers were used to place the organ models inside the phantom in a reproducible manner (A 1, 2) and (B 3, 4, 5, 6 and 7). Completely filled and sealed phantom container with flexible diaphragm (C) and Luer lock openings in the lid (C 8) (Source: Own figure).

Finally, a precisely designed 3D printed adapter is attached on the phantom lid (Fig. 13 A, B). This adapter incorporates a carriage with the double-acting cylinder and the diaphragm-shaped actuator. A six-meter-long hydraulic tube (Festo, Germany) connects the phantom to the linear stage. The entire experimental setup is depicted in figure 13 C.

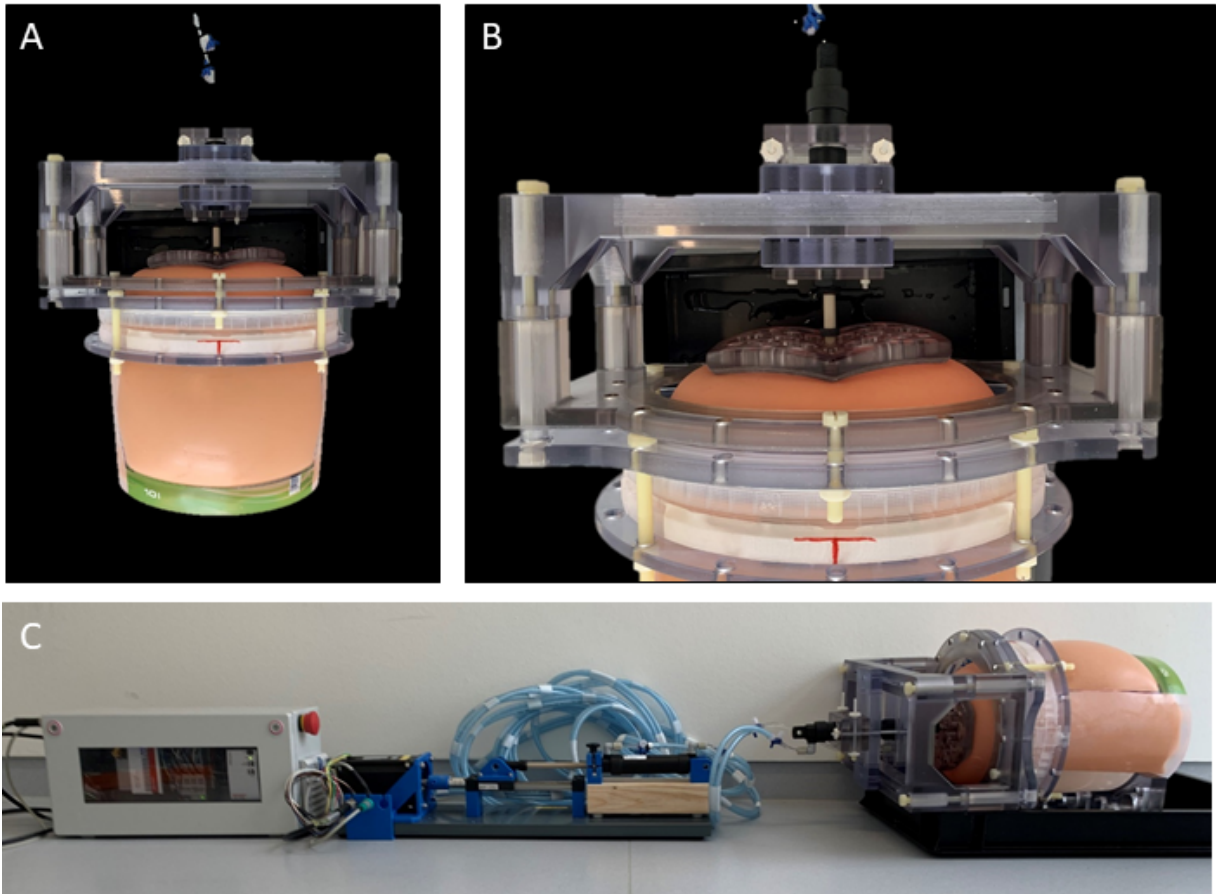


Figure 13: Phantom with attached adapter and diaphragm-shaped actuator (A), (B). Entire experimental setup with the hydraulic system, linear stage and the PLC (C) (Source: Own figure).

## 2.14 Experimental Setup

A total of three different experimental phantom setups were designed in order to perform intra-fractional image-guided radiation and an evaluation of organ motion. For all setups, the same container and motion control was used. Furthermore, the organs manufactured for the first setup remained the same throughout all experiments. Only supplemental organs that were used in the second and third phantom setup, such as pancreas and spleen, as well as the custom-made liver model that contained a tumor model were additionally manufactured.

### 2.14.1 Experimental setup overview

In the following an overview of the different experimental setups that were used for experiments is given. Setup 1 and 2 served as a foundation for the evaluation and optimization of breathing-induced organ motion. Throughout all the performed experimental setups, the same phantom container and motion control as well the same breathing curves were used for the respiratory simulation. The first setup comprised a liver and two kidney models that were embedded in a 0.4% of agarose gel. A total of three different breathing simulations were performed, one to simulate shallow breathing with a total amplitude of 15mm, the second to perform free breathing with an amplitude of 25mm and finally an amplitude of 40mm for a deep breathing simulation. Those three breathing curves were used for all subsequent experimental setups. For the second setup, a spleen and a pancreas model were added as additional organs. A pelvis and a spine model consisting of the L1 to L5 vertebrae were also fixated in the phantom container. With this version all three breathing curves were performed and measured with the MRI. The third and final setup resembled the second one, with the exception of the liver model. In this setup, the liver model was replaced with a newly designed model that incorporated a tumor model. Hence, this version was used for an end-to-end-test with an intra-fractional image-guided radiation with an MR-Linac. The different experimental setups are shown in table 4.

Table 4: Overview of the different experimental setup versions.

Setup	Organ models	Breathing simulation	Dosimetry
First	Liver, two kidneys	Shallow, free and deep	No
Second	Liver, two kidneys, spleen, pancreas, pelvis and spine	Shallow, free and deep	No
Third	Liver and tumor model, two kidneys, spleen, pancreas, pelvis and spine	Shallow, free and deep	Yes, with EBT3 films in liver tumor

### 2.14.2 First experimental setup

The first experimental setup consisted of the phantom container with two organ models, the PLC and the linear stage. The phantom container was filled with a 0.4% agarose gel containing a liver and two kidney models that were arranged in their anatomical foreseen positions, similar to what is shown in figure 14. The process of filling and assembling the phantom was carried out as described in chapter 3.3 which focuses on the phantom filling and assembly. The phantom was connected to the linear stage via six-meter-long tubes filled with fully demineralized water. In particular, the connection was established by means of a diaphragm-shaped actuator, which was directly connected to a double-acting cylinder and firmly bolted to the phantom container on a frame. The fixation of the phantom and the motion control remained the same throughout all experimental setups as well as the performed breathing curves. The primary application of this phantom was to perform breathing simulation during an MRI measurement and to analyze the breathing-induced organ motion afterwards. For the evaluation and optimization of the organ motion, MRI measurements were performed using a cine sequence, which acquires 200 2D images every 0.4 s. The analysis of these images was used to optimize the motion of the organ models to align them with the motion patterns and maximum amplitudes observed in the volunteers.

### 2.14.3 Second experimental setup

For the second setup, the same organ models were used. Additionally, a pelvis with a lumbar spine model and two additional organ models, a pancreas and a spleen, were added (Fig. 15). In comparison to the phantom version that is displayed in figure 15, only the liver model differed, as it did not contain a tumor model. Aside from that, both experimental setups were prepared the same way and all organ models were arranged in the same way. The organ models were arranged to their foreseen anatomical position inside a 0.4 % agarose mixture. For the fixation of the pelvis bone, a custom-designed holding plate was glued to the bottom of the container in order to ensure reproducible placement of the pelvis and spine model. As in the previous setup, the phantom container was connected to the linear stage via hydraulic tubes.

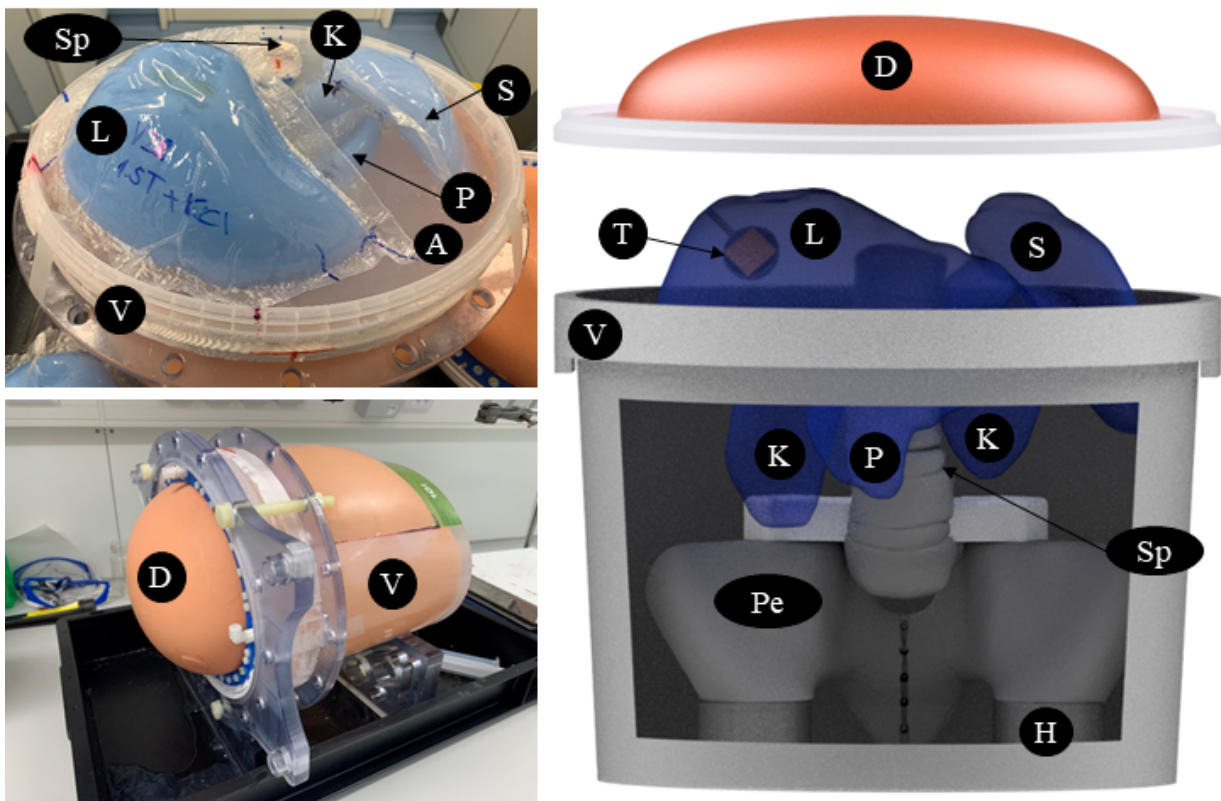


Figure 14: Third experimental setup. On the left, the filled phantom container vessel (V) is displayed containing a liver (L) with a tumor model (T), left and right kidney (K), spine (Sp), spleen (S), pancreas (P) that are embedded in 0.4 % agarose (A). A rendering of the phantom is shown on the right. A flexible diaphragm (D) made of silicone is attached to the lid and the pelvis (Pe) to its holding plate (H), which is firmly glued to the bottom of the container (Source: Own figure).

This version of the experimental setup served for the analysis of the organ motion and the additionally added organ models such as pancreas and spleen, primarily to also analyze the organ displacement in the composite and to compare it to the volunteer data.

#### **2.14.4 Third experimental setup with EBT3 films**

In order to provide an experimental setup that is capable of dosimetric evaluation (Fig. 14), a modified liver casting mold that provided a cutout for the insertion of a spherical tumor model was custom designed using CAD (Fig. 15 B, D). The tumor model is positioned within the liver at a depth of 20 mm. The tumor model was designed in such way that it offered the possibility to attach a 20x20 mm Gafchromic EBT3 film exactly in the middle of the tumor (Fig. 16 A). As a geometrical shape, a sphere with a diameter of 30 mm (Fig. 15 C) was chosen for the tumor model. To allow easy film insertion, the tumor model was 3D printed as two halves (Fig. 15 C). For this purpose, the model was divided in two equal parts along the coronal plane, to enable a reproducible and easy EBT3 film placement. In addition, a filler hole provided the possibility to fill a Ni-DTPA doped agarose mixture into the spherical tumor model to ensure anthropomorphic MRI and CT contrast.

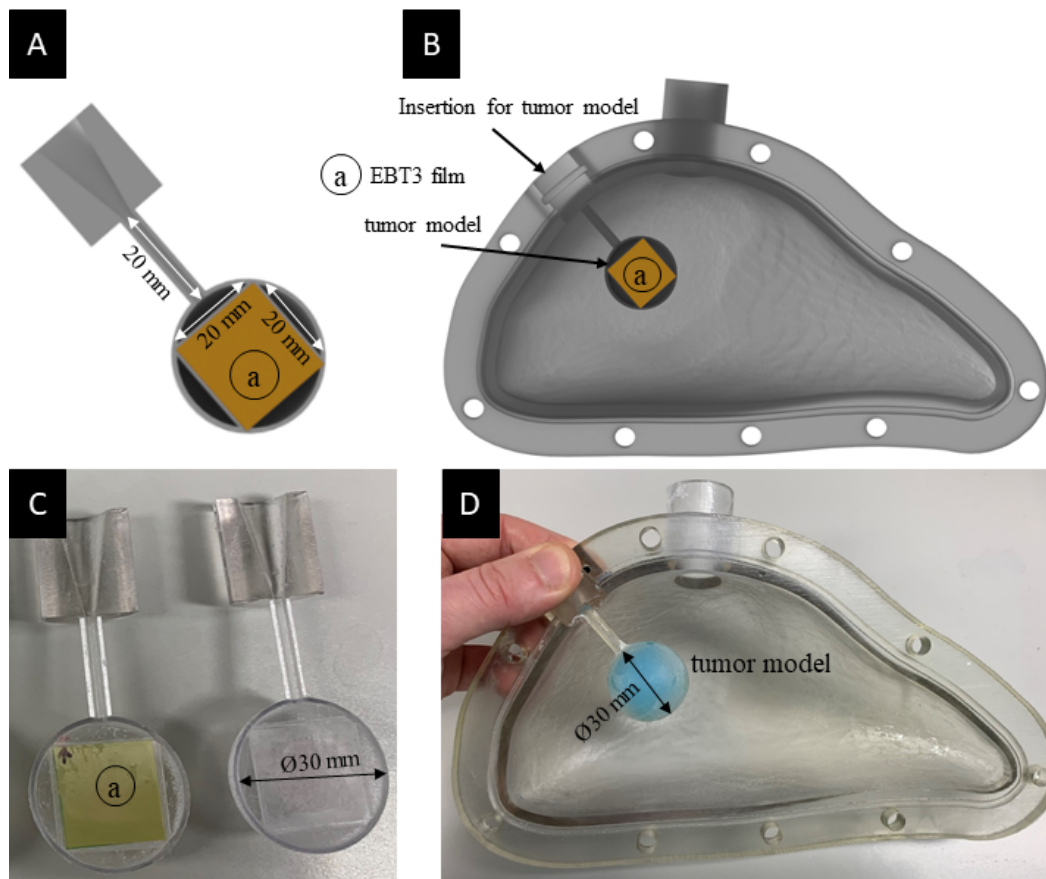


Figure 15: Liver casting mold with tumor model. Cross section of the spherical tumor model containing the EBT3 film (A). Tumor model inserted into the liver casting mold and fixated in the designated opening (B). 3D printed model of the tumor model with inserted film (C). (D) Shows the tumor model already filled out with a tumor-equivalent Ni-DTPA doped agarose mixture (Source: Own figure).

#### 2.14.5 EBT3 film evaluation

The evaluation of EBT3 films was carried out with a scanner that is recommended by the manufacturer. The transmission of the films was read by an EPSON V800 flatbed scanner. Therefore, a 48-bit RGB (Red Green Blue) mode with 300 dots per inch (dpi) was set. The image was analyzed using the Red channel, as it exhibits the greatest sensitivity among the RGB channels and aligns most accurately with the tested dose range, which is below 8 Gray (Gy) (Kang et al. 2017; RSD Breathing Phantom 2024).

#### 2.14.6 Dose offset determination of the EBT3 films

To determine the offset values that additionally contribute to the value of the optical density (OD) of the films, further measurements were carried out. A certain offset value is generated by the planning CT scans, which take place before irradiation. For this purpose, the film in the tumor model was replaced by a new, identical film after

irradiation at the MR-Linac, and the same planning CT was performed again for the phantom with the exact same conditions and the same imaging protocols.

In addition to the offsets generated by the planning CT, it was investigated whether an offset is applied during the manufacturing process of the liver and tumor model. In order to determine this offset, a total of six spheres identical to the tumor model were manufactured under the same conditions. For this purpose, the spheres were manufactured using the same material and 3D printing. A mixture was then produced in the laboratory with the same agarose proportion. Furthermore, the mixture had exactly the same temperature of 50° C during the filling of the spheres, which it had also had during the manufacturing of the tumor model. In order to simulate the condition of the surrounding liver, the tumor model was placed in a beaker. The beaker was subsequently filled with agarose so that the tumor model was exactly 20 mm deep inside the agarose (Fig. 16 C), to ensure the same conditions as in the phantom.

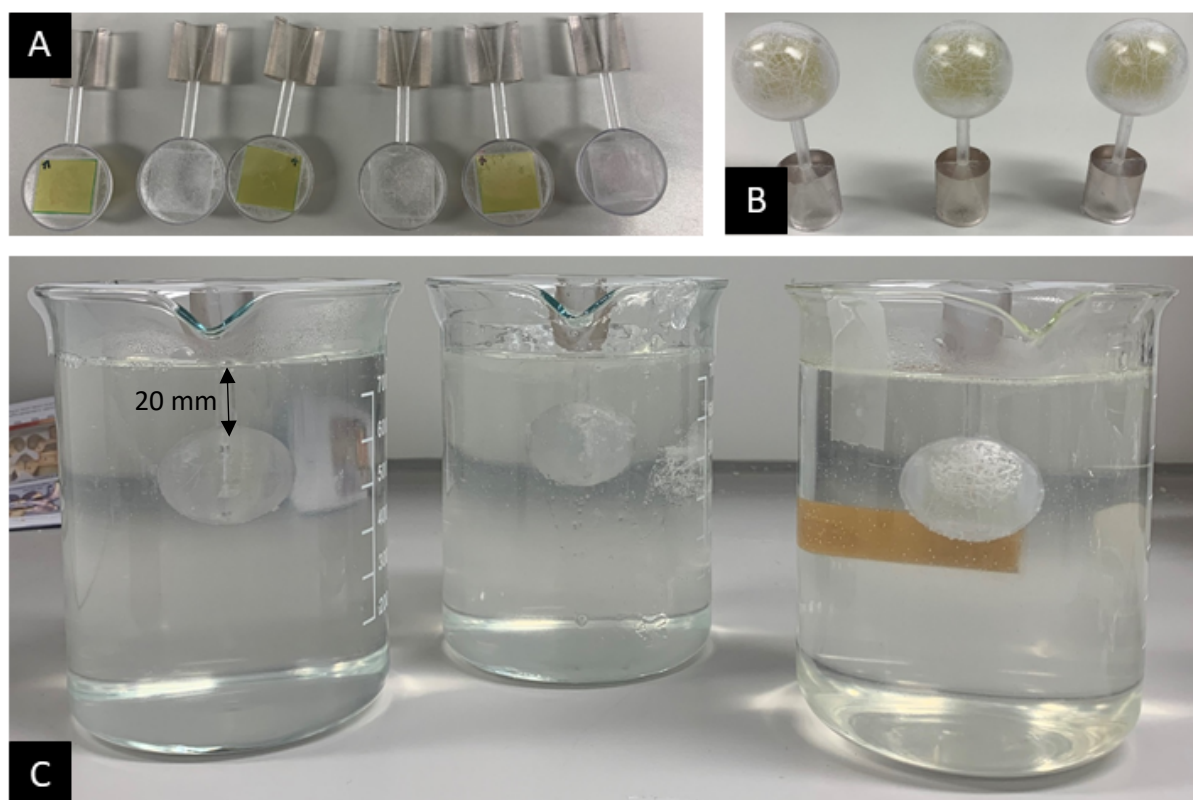


Figure 16: Manufacturing of the spherical tumor model that was used to determine the manufacturing offset. (A) Spherical tumor model with attached EBT3 film cut in half. (B) The two halves were glued together. After that, the tumor model is placed in an beaker with an agarose mixture, at a depth of 20 mm (C) (Source: Own figure).

## 2.15 MRI measurements

### 2.15.1 Quantitative T1 and T2 relaxation time

The quantitative T1 relaxation time of all organ models was measured by using a saturation recovery (SR) sequence (Fig. 17 A, B, C and D). This method uses a 90° pulse to rotate the longitudinal magnetization  $M_z$  into the xy-plane. Due to the spin-lattice interaction, the spins start to relax towards their equilibrium state. For this reason, a 90° pulse is repeated after a specified time, the inversion time (TI). A TI that is comparatively longer than the T1 causes the magnetization to relax to its equilibrium state. However, if the value is decreased to a magnitude near T1, the magnetization will not fully relax and therefore, after a 90° pulse, a certain amount of spins parallel to  $M_z$  will contribute to the magnetization  $M_{xy}$  where the signal is read out. To determine the quantitative T1 relaxation time, multiple SR scans need to be performed. The TI can be varied to acquire signals at different points in time along the relaxation curve. Afterwards, the signals can be used to theoretically calculate the intensity  $S_{T1}$  at a specific point in time and to fit a curve using the equation (3). In this thesis several SR sequences were used with different TI, starting from TI = 20 ms and subsequently increased up to TI = 5000 ms.

$$S_{T1} = S_0 (1 - e^{-\frac{TI}{T1}}) \quad (3)$$

To acquire the quantitative T2 relaxation time of a specific material, a spin-echo sequence was used. Applying a 90° pulse causes the z-component of the spins to rotate in the transversal plane and a phase synchronization of the precessing spins. The effect of the local field varieties and the spin-spin interactions cause the transversal magnetization  $M_{xy}$  to decay. However, the decay of the  $M_{xy}$  magnetization occurs with the relative relaxation time  $T2^*$  ( $T2^* < T2$ ) and not with the material-specific relaxation time T2. To determine the T2 relaxation time, it is important to compensate for the dephasing of the transversal magnetization caused by the local  $B_0$  field inhomogeneity. This can be done by using a so-termed spin-echo (SE) sequence. Since the local  $B_0$  field is not time dependent, its effect causing the dephasing of the transversal magnetization is reversible, whereas the T2 relaxation depending on the material-specific local field fluctuations is irreversible. Thus, only the effect of the local field varieties is considered to determine the relaxation time T2, and the effect of the local field fluctuation is neglected. After a 90° pulse the net magnetization starts dephasing due to the fact that some components are precessing faster than others, causing the loss of phase coherence.

If a  $180^\circ$  pulse is applied at time  $t = \tau$  along the x-axis, the components will be mirrored and start rephasing. After  $t = 2\tau$ , all components will point again to the same direction and result in a maximum signal intensity called spin-echo. If a series of  $180^\circ$  pulses is applied at the times  $t = 4\tau$ ,  $t = 6\tau$  and so on, multiple SE signals can be measured as the signal intensity decreases (Fig. 17 e and f). Those signals are used to fit a curve with the T2 relaxation rate as a characteristic exponential decaying function:

$$S_{T2} = S_0 \cdot e^{-\frac{TE}{T2}} \quad (4)$$

$S_0$  represents the initial signal intensity, and the echo time (TE) represents the time between two consecutive echoes. In this thesis, a multi-SE sequence with 32 echoes was used to calculate and fit the relaxation curve which depends on T2 using the equation (4) (Reiser et al. 2008; Weishaupt et al. 2006).

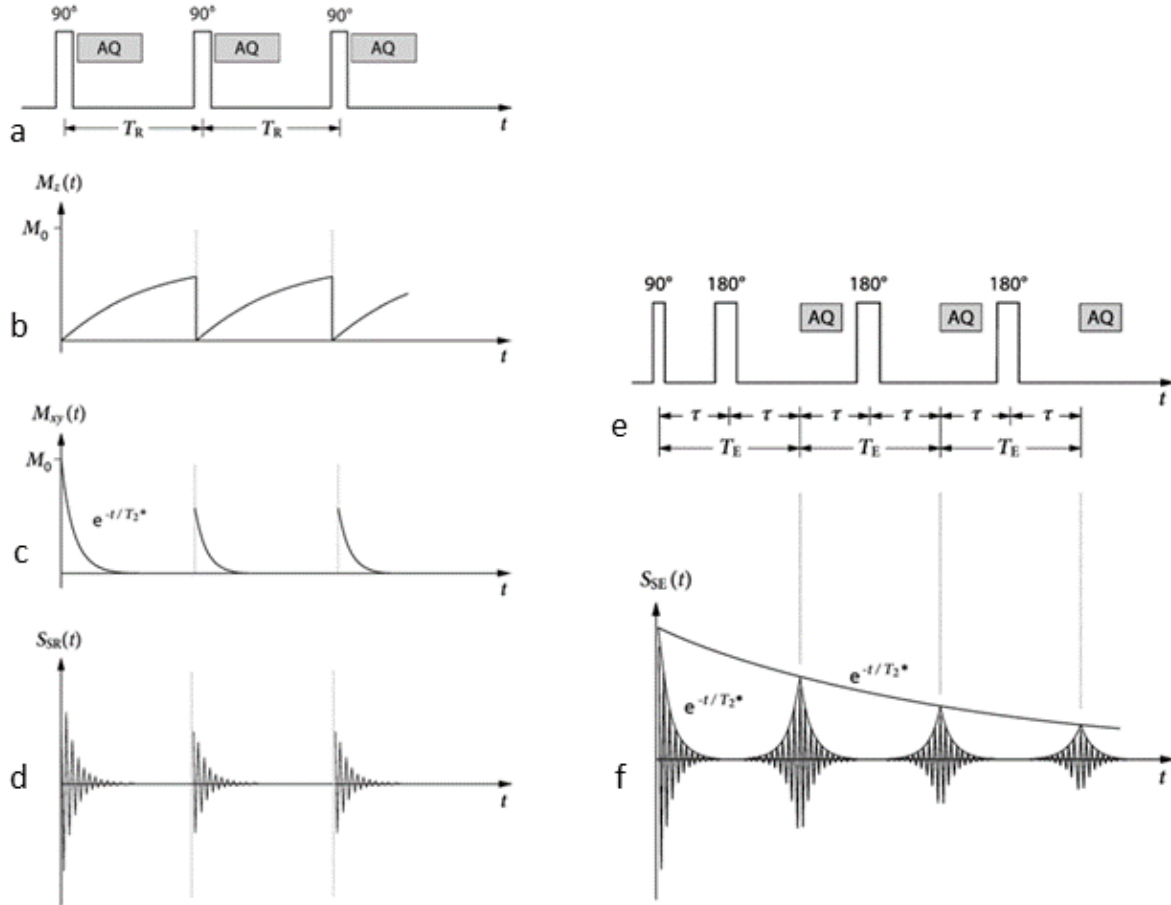


Figure 17: Saturation recovery and multi-spin-echo sequence: (a) Pulse sequence of a saturation recovery sequence. Signal acquisition (AQ) follows immediately after a  $90^\circ$  pulse. (b) After a  $90^\circ$  pulse, the longitudinal magnetization relaxes towards its equilibrium after the repetition time TR. The induced signal (d) is read out after the inversion time TI in the x-y-plane. (e) Pulse sequence of a multi-SE sequence. Multiple  $180^\circ$  pulses cause the rephasing of the spins to acquire the portion of the signal (f) after a specific echo time (TE). The read-out signal is now determined by the T2 decay and not T2\*. Figures reprinted from Reiser et al. 2008.

### 2.15.2 Acquisition of MRI cine measurements

In order to evaluate and track the organ movement within the phantom, a so-termed cine sequence was used at the MRI scanner. Prior to the cine sequence measurements, several T1w and T2w images were acquired. These images were used to localize the desired organ models and, later on for the selection of a slice through the individual organ model. Therefore, all T1w and T2w sequences were performed in the axial, sagittal and coronal plane. All cine sequences were adjusted the same for all experimental setups. Only the slices through the phantom as well as the imaging orientation, e.g. coronal and sagittal, were individually adjusted. For all experimental

setups, the same set of cine sequences was chosen. The only difference was that the first experimental setup only contained a liver and two kidney models. For the measurements, a set of cine sequences was acquired in the coronal plane with a central slice through the diaphragm to track its movement accurately (Fig. 18 A). To be able to track the movement of the liver and right kidney in SI and AP direction, a sagittal plane through these desired organ models was chosen (Fig. 18 B). The last image sequence was acquired in sagittal plane and a slice was chosen through the left kidney, the pancreas tail and spleen (Fig. 18 C). To ensure reproducibility, the sequence parameters remained the same for the different slice selections and orientations, only the phantom breathing motion was altered. For this purpose, different amplitudes were chosen: 15 mm for shallow, 25 mm for free and 40 mm for deep breathing simulation. To encompass all breathing amplitude and orientations of the phantom, 200 measurements were conducted every 0.4 s, with a TE = 1.26 ms, TR = 220.82 ms and a pixel bandwidth = 1030 Hz. Furthermore, a pixel spacing of 1.56 mm x 1.56 mm and a slice thickness of 4.5 mm were chosen.

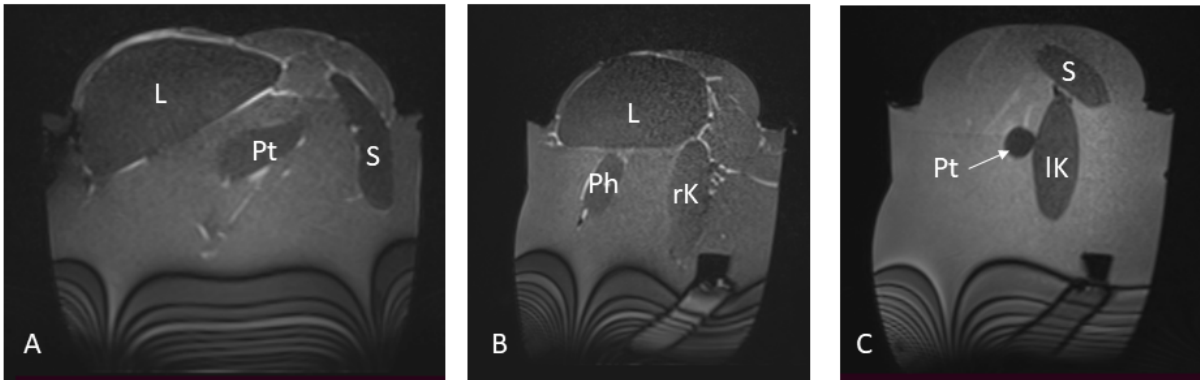


Figure 18: Orientation and slices that were acquired with the cine sequence for the second and third experimental setup. (A) displays a coronal cross-section of the phantom, illustrating the liver [L], pancreatic tail [Pt] and the spleen [S]. In (B), a sagittal slice through the phantom reveals the liver [L], pancreatic head [Ph], and the right kidney [lK]. Lastly, in (C), the spleen [S], pancreatic tail [Pt], and the left kidney [lK] are displayed (Source: Own figure).

### 2.15.3 PACS patient scans and starVIBE 991 MRI sequence

To analyze breathing cycles and breathing-motion-induced organ movement, several MRI volunteer datasets were acquired and pseudo-anonymized 4D CT images (subjects 1-5) from the PACS were provided by the division of medical physics in radiology, Deutsches Krebsforschungszentrum (DKFZ) Heidelberg. Subject datasets included one complete breathing cycle. A total of eight different breathing phases (20%, 25%, 50%

and 75% inspiration amplitude – 100%, 70%, 40%, 0% expiration amplitude) were obtained with a Siemens SOMATOM CT Scanner (Siemens Healthineers, Germany) with a pixel spacing in the axial plane of 0.977 mm x 0.977 mm and a slice thickness of 3mm. An energy of 120 kV and a 66 mA current was used. The volunteer data was acquired using the MAGNETOM Aera Siemens (1.5T) MRI scanner (Siemens Healthineers, Germany). In order to prevent the volunteer from forced and thus biased normal breathing, the initial image data acquisitions were performed without breathing commands. Next, the volunteer was asked to breathe in a shallow and deep manner, respectively. Imaging data was collected in coronal and sagittal plane every 0.4 s using a fast real-time single-slice cine sequence with 200 measurements (TE = 1.26 ms, TR = 220.82 ms, pixel bandwidth = 1030 Hz) with a pixel spacing of 1.56 mm x 1.56 mm and a slice thickness of 4.5 mm. In order to allow for reproducibility, the same sequence parameters for the cine measurement were used for the healthy volunteer as well as to conduct imaging data with the phantom. Afterward, a 3D starVIBE 991 sequence (TE = 1.19 ms, TR = 2.41 ms, pixel bandwidth = 970 Hz, pixel spacing = 1.56 mm x 1.56 mm and slice thickness = 1.8 mm) was performed to acquire automatically gated axial images for normal and deep breathing. Afterwards, five different bins (bin 1 – bin 5) were generated for each breathing phase detected by the algorithm. Bin 1 represents the 100% expiration phase and bin 5 represents the 100% inspiration phase (Fig. 19). Finally, the volunteer was asked to hold his breath after inspiration and expiration respectively, while a T1w vibe963 sequence (TE = 1.64 ms, TR = 4.2 ms, pixel bandwidth = 300 Hz, pixel spacing = 1.02 mm x 1.02 mm and slice thickness = 1.6 mm) was used to acquire 3D image data in axial, sagittal and coronal orientation.

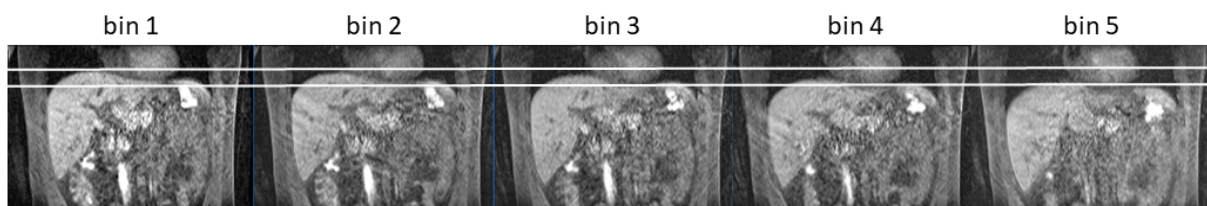


Figure 19: Example of acquired image data in the coronal plane while the volunteer was asked to breathe deeply, using a starVIBE 991 sequence. White lines indicate the breathing amplitude in the CC direction. Bin 1 shows 100% expiration – bin 5 100% inspiration amplitude (Source: Own figure).

## **2.16 Image analysis**

### **2.16.1 Evaluation of quantitative T1 and T2 relaxation times**

The analysis of the acquired quantitative T1 and T2 weighted image data was performed using an in-house developed MATLAB (The MathWorks, Inc., USA) script with a graphical user interface (GUI) (Mann et al. 2017). For this purpose, a T1 and T2 map was calculated, which considered each voxel for the computation of the relaxation time. Each voxel of each individual TE of the segmented slice was taken into account for the calculation. For the determination of the quantitative T1 relaxation time, the script considered each voxel of each individual TI for the entire segmented area. The GUI provided the possibility to create a region of interest (ROI) for the calculated map of the T1 respectively T2 relaxation time. Thereupon, only the voxels within the ROI are considered to calculate a mean value with a standard deviation. Using this approach, all T1 and T2 relaxation times were calculated for the organ models and for the long-term experiment.

### **2.16.2 Analysis of breathing data**

Segmentation of DICOM data was performed using MITK (Nolden et al. 2013). Before the image processing was done, the datasets were converted into the .nrrd-file format using Fiji (Schindelin et al. 2012), in order to allow for effortless and highly compatible handling of DICOM data. The .nrrd (Nearly Raw Raster Data) format is a file format used for storing and exchanging multidimensional raster data. It is commonly used in medical imaging, particularly for storing volumetric image data such as CT scans, MRI scans, and other types of 3D medical images. Fiji on the other hand is a distribution of the open-source image processing software, ImageJ. For segmentation, either the upper-lower threshold and otsu threshold based algorithm or manual 2D segmentation was performed. Otsu's thresholding is an image processing technique for automatically segmenting images into foreground and background regions. By finding the threshold that maximizes the separation between pixel intensities in an image histogram, Otsu's method efficiently identifies the optimal threshold for image segmentation without requiring manual intervention. The upper-lower threshold tool makes it possible to adjust a threshold of a specific grey value range to enable an algorithm to automatically segment the desired regions. With an algorithm based on otsu threshold, the user can define several regions, and based on the image histogram, the pixels will be assigned to different regions. Next, the 2D segmentation tool makes it possible to segment the desired region manually by drawing a ROI of the region, and it additionally provides

a 3D interpolation. However, it was important to check the segmentations of the interpolated slices and correct them manually if necessary. The described procedure was applied to the image data of the healthy volunteer, the subject, as well as to the phantom datasets. Afterward, the segmented regions were stored as masks and post-processed with python. Depending on the sequence used to acquire the image data, a different script was used. The basis for the calculation of the movement of the organs was the center of mass (COM) of the individual organ model or patients' organ. Therefore, the image data was resampled to a fixed size of 1 x 1 x 1 mm to avoid distortion caused by different pixel spacing.

The analysis of breathing data involved the utilization of three different approaches, reflecting the acquisition of three distinct types of imaging data. The primary data source was the PACS, which contained eight different respiratory phases. These phases were used for analyzing the maximum and minimum amplitude of respiratory motion. An in-house developed Python script was employed for the analysis of all three approaches. Thus, for each approach a slightly modified python script was used, as the imaging data differed. To calculate the maximum and minimum amplitudes of respiratory motion from the PACS data, a COM was computed from the static images encompassing the entire organ volume. The COM was then subtracted for each respiratory phase, providing the movement of the target organ. Figure 19 illustrates the PACS data in purple, representing the maximum inspiration, and in orange, indicating the maximum expiration. These representations were performed in three distinct orientations: axial, sagittal, and coronal. The second approach involved the analysis of MRI data acquired using the starVIBE sequence. Each bin was used to calculate the COM for individual organs. This analysis was carried out for both volunteer and phantom data. A 3D mask was applied to each bin to facilitate the calculation of COM, allowing for a precise assessment of the motion of the individual organs in response to respiratory changes. As a final method, the 2D cine sequence images captured over time were analyzed to study the dynamic motion of individual organs. To achieve this, a COM of each 2D mask was computed for each timestamp, providing a comprehensive visual representation of the motion of each organ throughout the respiratory cycle. Figure 20 shows the maximum (red) and minimum (purple) motion of the liver and left kidney. This method allowed for the visualization, comparison, and in-depth analysis of how each organ's position evolved over time, providing valuable insights into respiratory-induced organ motion.

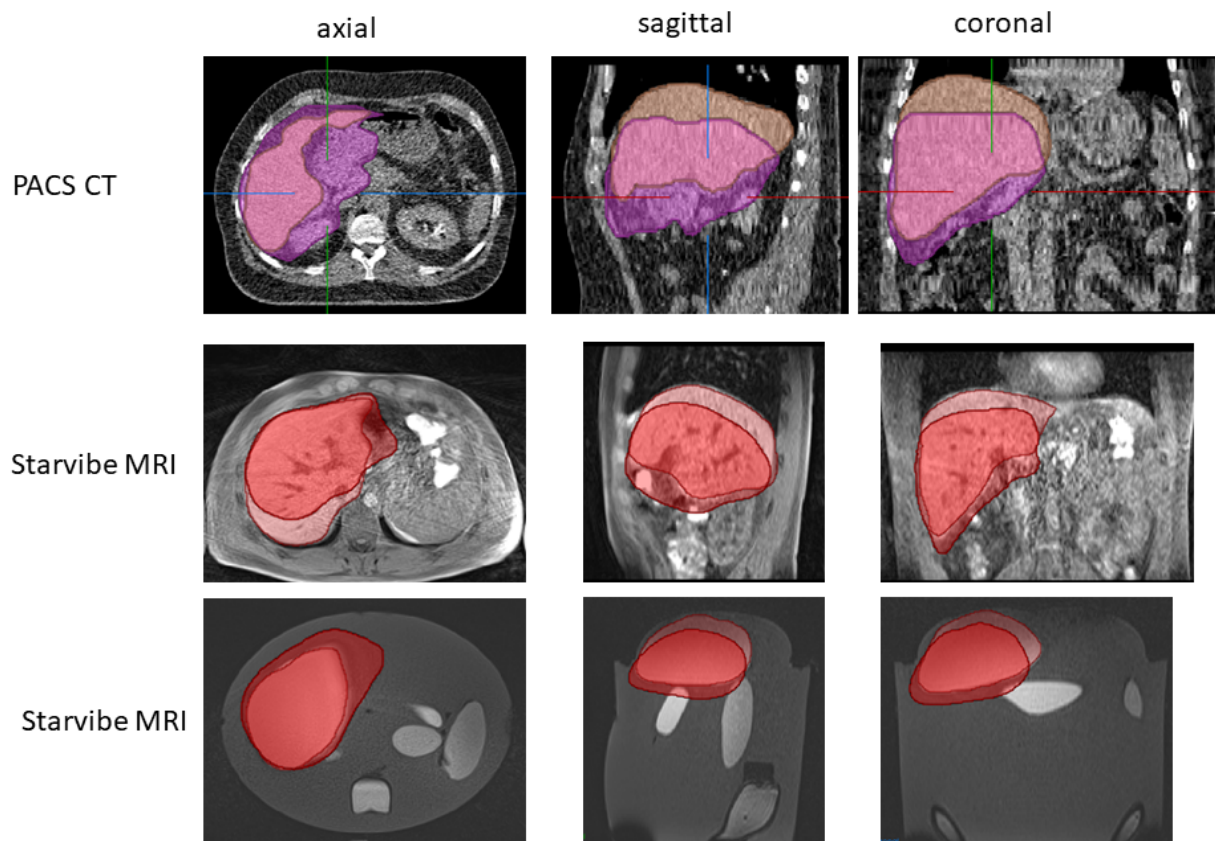


Figure 20: The figure presents axial, sagittal, and coronal slices of CT patient data obtained from PACS, volunteer data acquired using the starVIBE sequence on an MRI scanner, and equivalent data collected with the same starVIBE sequence for the phantom. Liver segmentation was performed in all three planes (sagittal, axial, and coronal). In the upper section, liver positioning is represented in orange for maximum expiration and in purple for maximum inspiration. In the middle section, liver displacement is depicted for the starVIBE sequence, which automatically detected the maximum and minimum motion amplitudes. The lower part of the figure displays a similar liver displacement pattern, but this time for the phantom using the same starVIBE sequence (Source: Own figure).

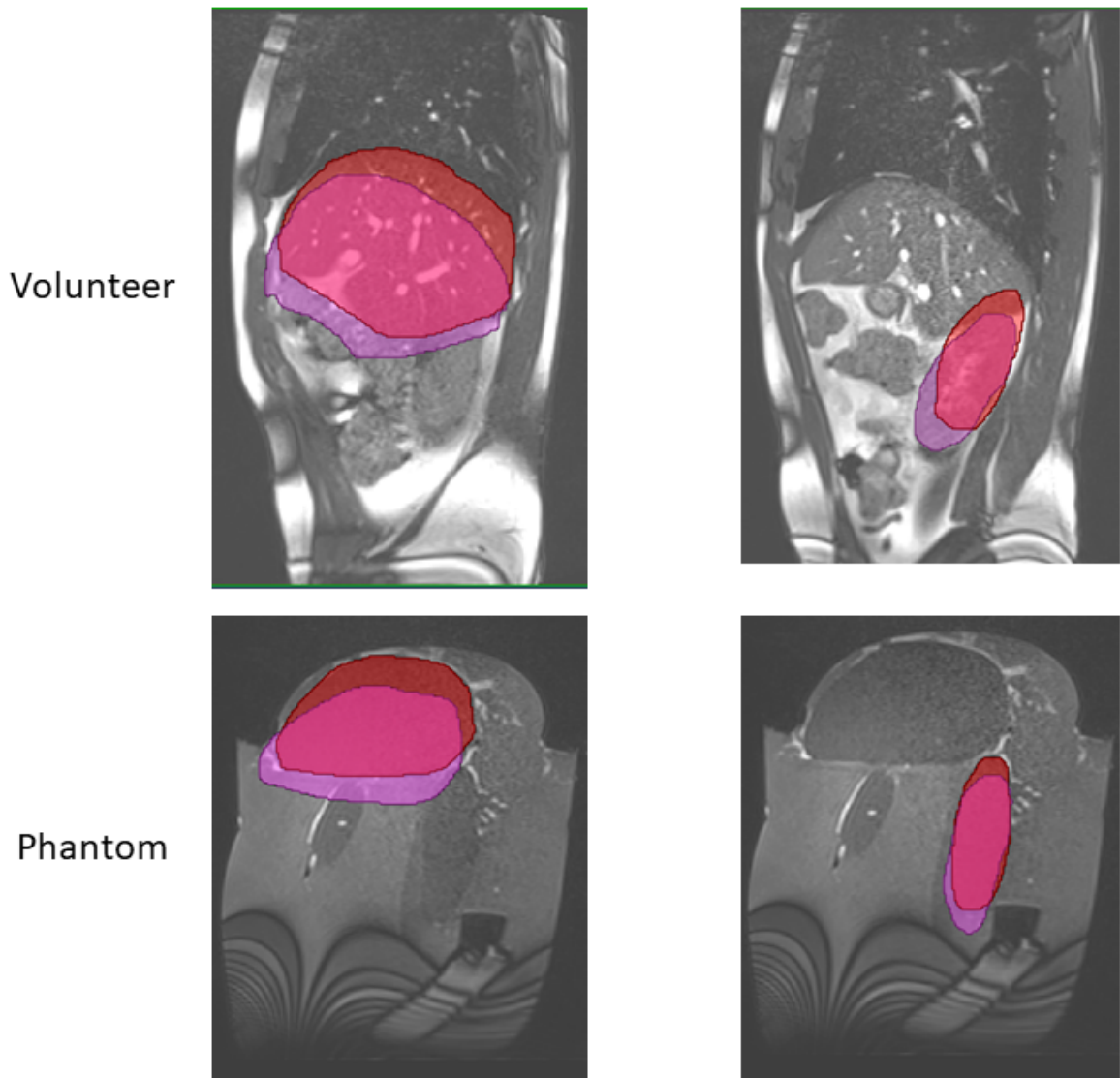


Figure 21: In the upper section of the figure, a sagittal slice of the acquired volunteer cine sequence MRI data is presented. On the left, a segmentation is applied to delineate the liver during deep breathing at maximum amplitude, as denoted by the purple and red segmentation mask. On the right, a similar segmentation is shown for the left kidney. The lower section of the figure exhibits the corresponding segmented organs for the phantom's liver and left kidney model during deep breathing as well (Source: Own figure).

## 2.17 Breathing simulation

The breathing simulation was implemented with the following formula (equation 6) (DeWerd und Kissick 2014a):

$$X(t) = A * \cos^2\left(\frac{\pi * t}{\tau} + \frac{\pi}{2}\right) \quad (6)$$

For the simulation with the phantom, three different breathing curves with different amplitudes (A) and phases ( $\tau$ ) were chosen. Deep, normal and shallow breathing was realized with an amplitude of 15 mm, 25 mm and 40 mm and a phase of 7 s, 11 s and 18 s, respectively. The simulation was performed over time (t) along CC direction (X) in the phantom. All breathing motion experiments were tested and image acquisition was conducted with an MRI scanner.

## 2.18 Contrast stability phantom

The organ models were manufactured using a mixture of different chemical concentrations of Ni-DTPA-doped agarose, water and KCl. Therefore, if an organ model is placed in a 0.4% agarose mixture, the way it is inside the phantom container, the different ion concentration of the organ models and the surrounding agarose cause an ion diffusion. Hence, preliminary experiments were conducted and the evaluation showed a distinctly visible loss in T1 contrast in qualitative T1 weighted images. Two hours after the preparation, a visible contrast loss in T1 weighted image could already be observed. After 21 days, a complete ion exchange was established. Figure 21 displays the temporal T1 contrast loss of the contrast phantom if the individual layers are not covered in any foil. The ion exchange process is illustrated in figure 8 A and B. Therefore, it was important to ensure the contrast stability of the T1 and T2 relaxation times of the organ models over a period of time. To investigate the cause and prevention of T1w contrast loss, a second phantom (contrast phantom) was developed.

For this purpose, a geometrically shaped phantom was manufactured with round layers (diameter 100 mm, thickness 20mm). Two out of four layers were manufactured out of an organ-equivalent agarose mixture OEAM 1 and OEAM 2, based on the chemical composition for 3T MRI of kidney and liver respectively (Table 1). The other two layers were comprised of 0.8% of agarose mixture (AM1 and AM2) to mimic fatty tissue and separate OEAM1 and OEAM 2 from each other. A total of two identical sets of round layers of OEAM1 and OEAM 2 as well as of AM1 and AM2 were

manufactured. The layers were placed on top of each other in a vessel in the following order (from bottom to top): AM1-OEAM1-AM2-OEAM2 (Fig. 24 A). To allow for a potential ion exchange in the first vessel (Fig. 24 A), the layers were placed on top of each other without any separating foil, while the layers in the second vessel (Fig. 24 B) were packed and vacuum sealed in foil (Caso 1295, CASO Design). Both vessels were poured with 0.4% of agarose so that the layers were completely covered by the agarose. This phantom was manufactured in order to investigate potential ion exchange and associated contrast loss. As the organ models are located in agarose, this causes Ni-DTPA ions to diffuse into the surrounding agarose.

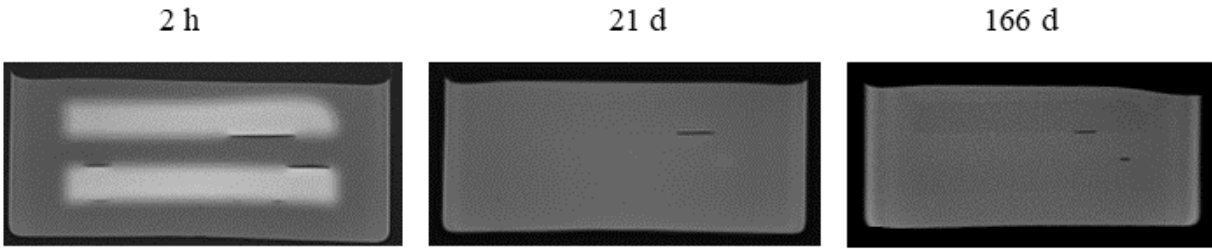


Figure 22: Quantitative T1 weighted images of the contrast phantom. The contrast phantom with the different layers of OEAM1, 2 and AM1, 2 measured with a qualitative T1 weighted sequence at an MRI scanner 2 hours, 21 days and 166 days after preparation (Source: Own figure).

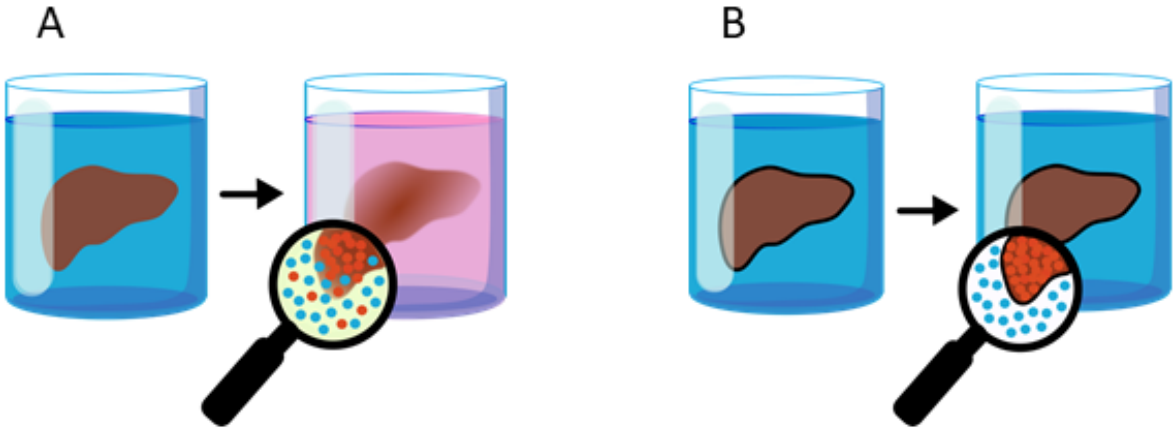


Figure 23: Illustration of ion exchange: The liver model manufactured using Ni-DTPA doped agarose has a higher ion concentration than the surrounding agarose, which leads to ion diffusion if the model is not covered in foil (A). Covering the liver model in foil (B) prevents any possible diffusion inside the vessel (Source: Own figure).

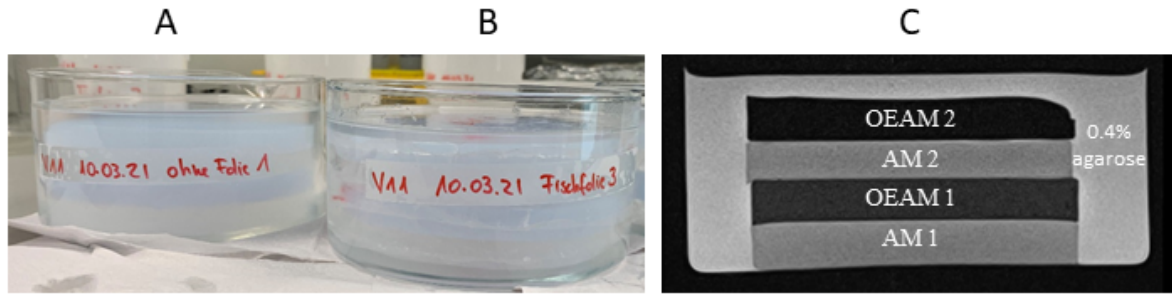


Figure 24: Phantom to investigate contrast stability over a period of time. The first vessel (A) contains surrogate tissue samples, which were placed on top of each other without any separating foil. The second vessel (B) contains the exact same surrogate tissue samples, but each was packed and sealed in foil under vacuum. A qualitative T2 weighted MRI image of the first vessel (C) shows the contrast phantom and the different surrogate samples inside the vessel (Source: Own figure).

## 2.19 Evaluation of contrast stability

To investigate the contrast stability over a period of time, MRI measurements were conducted for two hours (day 0), on day 1, on day 24 and on day 166 after the preparation. Due to the fact that the contrast stability phantom was manufactured for 3T MRI, all measurements were acquired with the MR-PET Siemens Scanner operating at  $B_0 = 3T$ . Therefore, the phantom vessel was placed in a head coil in the MR scanner. An axial slice through the cross section of the vessels with a thickness of 5 mm was selected and imaged with different sequences. A multi-spin-echo sequence was used to acquire quantitative T2 relaxation times. As echo time,  $TE = 8.3ms$  was chosen with a repetition time  $TR = 5000 ms$ . The voxel size for each individual echo was  $1.1 \times 1.1 \times 5 mm$ , with the 5 mm dimension representing the slice thickness. To conduct T1 times, several saturation recovery sequences with varying inversion times starting from  $TI = 20 ms$  up to  $TI = 5000ms$  were used, with a voxel size of  $1.1 \times 1.1 \times 5 mm$ . For the evaluation of the quantitative T1 and T2 time, an in-house developed MATLAB (The MathWorks, Inc., USA) graphical user interface (Mann et al. 2017) was used. For this purpose, rectangular regions of interest were placed in the center of each layer of the contrast stability phantom. Next, a 2D T1 map calculation for quantitative T1 relaxation time and a 2D T2 map for quantitative T2 relaxation time was created, respectively. This evaluation considers each voxel of the segmented ROI and calculates the T1 or T2 relaxation time for each voxel over the entire image series.

## 2.20 Phantom measurements

The imaging protocol commenced with a localizer scan to ensure precise anatomical localization. Subsequently, a series of qualitative imaging sequences, including T1 starVIBE and T2-weighted qualitative sequences, were employed for accurate positioning. To enhance the reliability of the measurements, each amplitude was recorded multiple times. The cine sequence was performed with 200 measurements to capture the dynamic motion of the target organ. Additionally, measurements were taken using the binning method with the advanced starVIBE 991 sequence, allowing for different breathing phases of the respiratory motion.

## 2.21 Calculation of relative organ movement

Diaphragm, liver and kidney were semi-automatically segmented using MITK (Nolden et al. 2013) and the phantom's 2D cine-MR measurements over 55 s for three different input amplitudes. The center of mass of the liver and the kidney as well as the maximum amplitude in CC direction were calculated. Furthermore, liver movement as well as kidney movement were compared to diaphragm movement for the first experimental setup. For the second and third setup, an additional comparison to the diaphragm for the organ models pancreas and spleen was performed. The liver to diaphragm movement ratio (LDMR), the kidney to diaphragm movement ratio (KDMR) the spleen to diaphragm movement ratio (SDMR) and the pancreas to diaphragm movement ratio (PDMR) were computed based on the following equations:

$$LDMR = \frac{CC_{Liver} * 100}{CC_{Diaphragm}} \quad (7)$$

$$KDMR = \frac{CC_{Kidney} * 100}{CC_{Diaphragm}} \quad (8)$$

$$SDMR = \frac{CC_{Spleen} * 100}{CC_{Diaphragm}} \quad (9)$$

$$PDMR = \frac{CC_{Pancreas} * 100}{CC_{Diaphragm}} \quad (10)$$

Diaphragm, liver, kidney, spleen and pancreas motion of the healthy volunteer were extracted at the end-inhale and end-exhale phases using MITK. LDMR and KDMR were computed and compared to the respective organ motion of the phantom. Data was presented as mean  $\pm$  standard error of mean (SEM) and the significance across

multiple groups was examined using a one-way analysis of variance (ANOVA) test using a Bonferroni post-hoc test. A p-value of less than 0.05 was considered significant.

## 3 Results

This chapter presents a series of crucial findings that are at the core of this work. Starting by examining 'Contrast Stability' that should ensure that the image contrast stays stable and accurate. Then, a comparison is made between the phantoms' CT and MRI images with real patients and volunteer imaging data in 'Comparing Phantoms and Patients in CT and MRI Imaging.' Evaluation of Breathing Motion explores the impact of respiration on the organ motion which once again is compared to volunteer and patients' data. Finally, in a performed end-to-end test using the MR-Linac we conduct comprehensive experiments that mimic real-life conditions, including breathing dynamics and dosimetry measurements.

Parts of this section are already published (Weidner et al. 2022).

### 3.1 Evaluation of contrast stability

#### 3.1.1 Long term experiment

The evaluation of the contrast stability phantom showed a visible decrease of T1 contrast in OEAMs and AMs without foil protection after 166 days (Fig. 25 A). The qualitative T1w image already displays a blurring of the contrast only 2 hours after the preparation. However, the T2 contrast did not show any loss in contrast. For the OEAMs and AMs sealed with foil no visible difference for T1 contrast was observed, additionally no significant difference for T2 contrast could be found. On the other side, the T2 contrast remained unaltered 166 days after the fabrication in both vessels (Fig. 25 E and F). A significant increase of quantitative T1 for OEAM1 and 2 was found of 43.26% and 49.97%, respectively one day after the preparation (Fig. 25 C). In addition, AM1 and AM2 demonstrated a reduction of T1 relaxation time of 51.33% and 32.84% (Fig. 25 C). The quantitative evaluation of T1 and T2 relaxation times revealed a complete ion exchange of Ni-DTPA after 21 days. In comparison, the vessel with sealed showed stable T1 contrast over time and a non-significant change of less than 10% was found for OEAM 1, OEAM 2, AM1 and AM2 (Fig. 25 D).

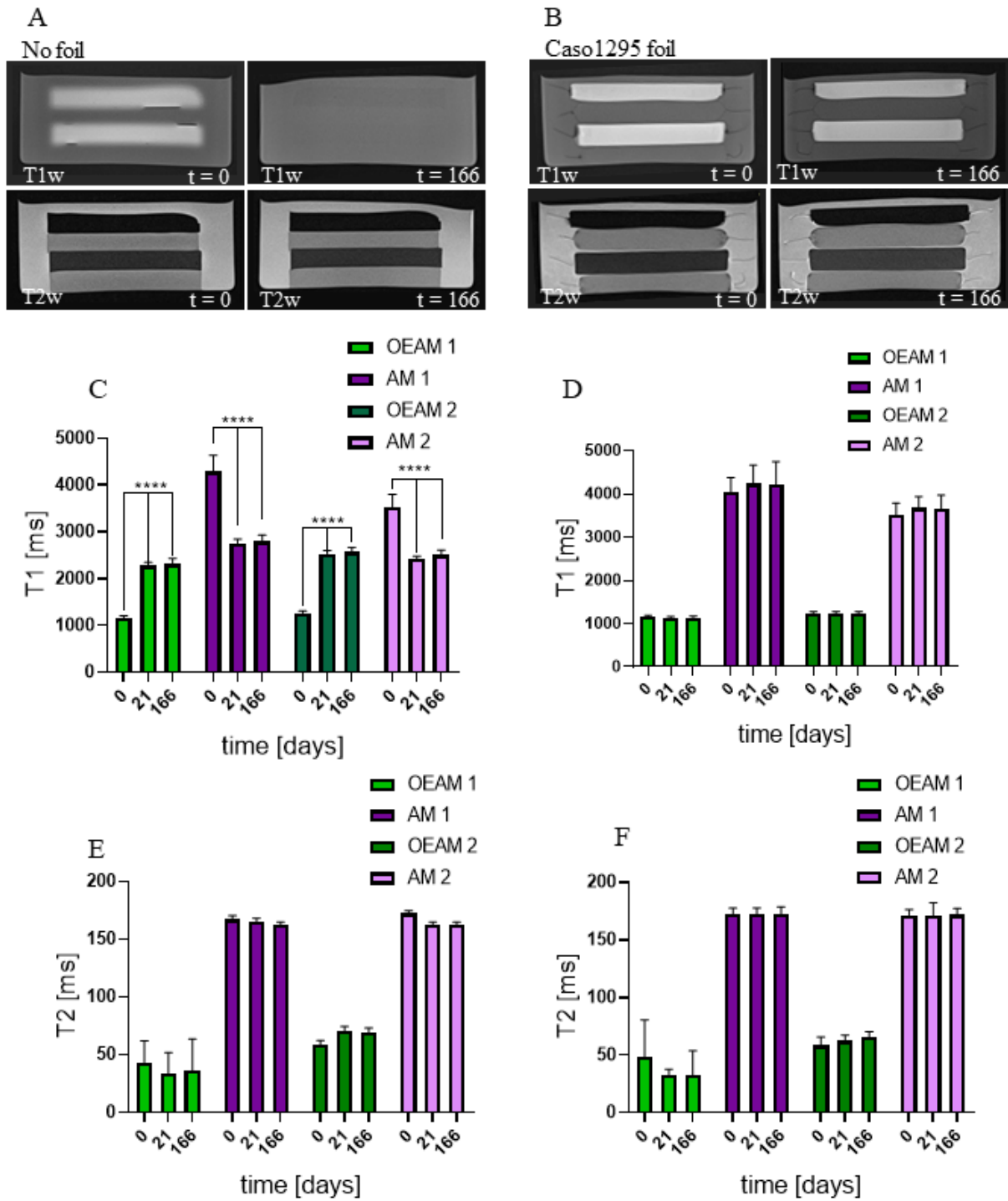


Figure 25; Qualitative T1w (A) and T2w images of OEAMs and AMs obtained without (A) and with (B) sealing at day 1 and day 35. Temporal development of T1 relaxation time of non-sealed (C) and sealed (D) OEAMs and AMs. Comparison of T2 relaxation time in non-sealed (E) and sealed (F) OEAMs and AMs at day 1 and day 35 (Weidner et al. 2022).

### 3.1.2 Temporal contrast stability of the organ models

The evaluation of the contrast stability phantom revealed that covering the organ models in foil ensures stable T1 and T2 relaxation times. Therefore, the temporal contrast stability of each organ model, which was used for the phantom experiments, was investigated. All organs were packed and vacuum sealed in foil and remained for at least 60 days throughout all experiments in the phantom. Even for new versions of the experimental setup, the same organ models were used for the experiments, only additionally added organ models were manufactured. Covering the organs in foil ensured the temporal contrast stability and the evaluation revealed a non-significant change of less than 4.5% for the T2 relaxation time and less than 2.6 % for the T1 relaxation time for the organ that were prepared for 1.5T. On the other hand, a non-significant change of less than 0.8% for the T1 and 7.6% for the T2 relaxation time of the organs prepared for 3.0 T was calculated. The evaluation of the quantitative T1 and T2 relaxation times revealed no significant changes. Figure 26 shows the T1 and T2 relaxation time changes for each individual organ models either prepared for 1.5 T (Fig. 26 A,B), or prepared for 3.0 T (Fig. 26 C,D). Additionally, the exact time after which the individual organ models were measured an additional time, is shown above the corresponding bar.

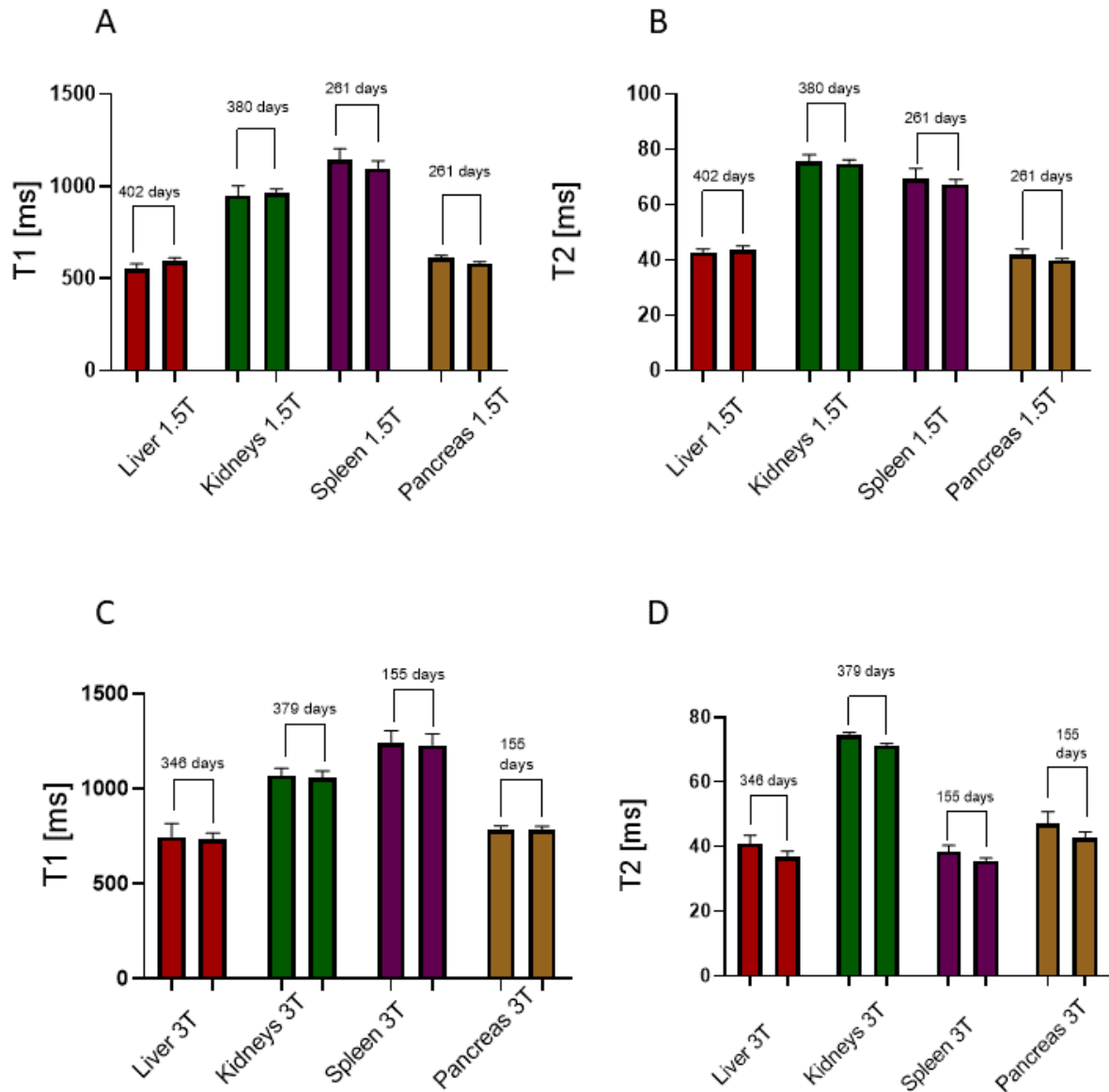


Figure 26: Relaxation time stability over a period of time for all organ models. T1 relaxation time stability for the organ models manufactured for 1.5 T (A) and 3.0 T (C) the time above the bars indicates the time period after which the second measurement was performed. The stability of the T2 relaxation time for 1.5 T is shown in (B) and for 3.0 T in (D) (Source: Own figure).

### 3.2 Tissue-equivalent values for MRI and CT imaging

For all the organ models that were used for the experiments, the relaxation times were measured prior to the experiments. The evaluation revealed for the organs prepared for 1.5 T and used in the first experimental setup, a relaxation time  $T1 = 552.9 \pm 26.2$  ms and a  $T2 = 48.2 \pm 1.2$  ms for the liver model and a  $T1$  of  $950.42 \pm 25.27$  ms and  $T2 = 76 \pm 3$  ms for both kidney models. Organ models that were manufactured for

3T, demonstrated a relaxation T1 of  $742 \pm 53$  ms, a T2 of  $41 \pm 3$  ms for the liver and a T1 of  $1070 \pm 39$  ms, T2 of  $71 \pm 1$  ms, respectively for both kidney models. In addition, the HU values of the 1.5T organs models were evaluated and are shown in table 4 along with the relaxation times and the reference values. The prepared liver and kidney models did not show significant differences from reference values for T1 and T2 relaxation times for both 1.5 T and 3 T. Furthermore, realistic HU in CT could be achieved for all organ models, without significant deviations compared to reference values.

Table 5: Comparison of T1 and T2 relaxation times for 1.5 T and 3.0 T between the manufactured organ models and reference values. The HU measured with the CT was evaluated from the 1.5T organ substitutes (Lamba et al. 2014; Bazelaire et al. 2004).

	Liver	Liver <sub>Ref</sub>	Kidney (r.)	Kidney (l.)	Kidney <sub>Ref</sub>
1.5 T MRI					
T1 [ms]	$552.9 \pm 26.2$	$586 \pm 39$	$950.42 \pm 25.27$	$971.56 \pm 26.11$	$966 \pm 58$
T2 [ms]	$48.2 \pm 1.2$	$46 \pm 6$	$79 \pm 1.7$	$77.5 \pm 1.5$	$87 \pm 4$
3 T MRI					
T1 [ms]	$741.9 \pm 53.1$	$809 \pm 71$	$1039.9 \pm 46.5$	$1070.1 \pm 38.6$	$1142 \pm 154$
T2 [ms]	$40.8 \pm 2.6$	$34 \pm 4$	$70.6 \pm 1.1$	$74.3 \pm 1.0$	$76 \pm 7$
CT					
number [HU]	$44.0 \pm 3.2$	$50.4 \pm 10.7$	$26.6 \pm 2.7$	$25.7 \pm 2.9$	$29.5 \pm 5.1$

The liver and kidney organ models remained the same for the subsequent experimental setups therefore, only the additionally added organ models such as the pancreas, spleen and spine model were evaluated. Prior to the placement inside the phantom vessel, the quantitative T1 and T2 relaxation times were determined. As shown in table 5 the evaluation revealed no significant differences compared to the reference values. To better visualize the comparison between the organ models and the reference values, the figure 27 displays the relaxation times T1 (Fig. 27 A, C), T2 (Fig. 27 B, D) and the HU values (Fig. 27 E) and the corresponding standard deviation (STD) in comparison to the reference values. For the reference HU value of tumor HU only one value was found in the literature, therefore no STD is indicated here.

Table 6: Comparison of T1 and T2 relaxation times for 1.5T and 3.0T between the manufactured organ models and reference values. The HU measured with the CT was evaluated from the 1.5T organ substitutes (Lamba et al. 2014; Bazelaire et al. 2004).

	Pancreas	Pancreas <sub>Ref</sub>	Spleen	Spleen <sub>Ref</sub>	Spine	Spine <sub>Ref</sub>
1.5 T MRI						
T1 [ms]	613 ± 11	584 ± 14	1145 ± 58	1057 ± 42	619 ± 20	549 ± 53
T2 [ms]	42 ± 2	46 ± 6	69 ± 4	79 ± 15	44 ± 5	49 ± 8
3 T MRI						
T1 [ms]	785 ± 20	725 ± 71	1241 ± 64	1328 ± 31		
T2 [ms]	38.35 ± 2	43 ± 7	74.3 ± 1	61 ± 9		
CT						
number [HU]	55 ± 11	50 ± 11	31 ± 4	44 ± 4		133 ± 37.6

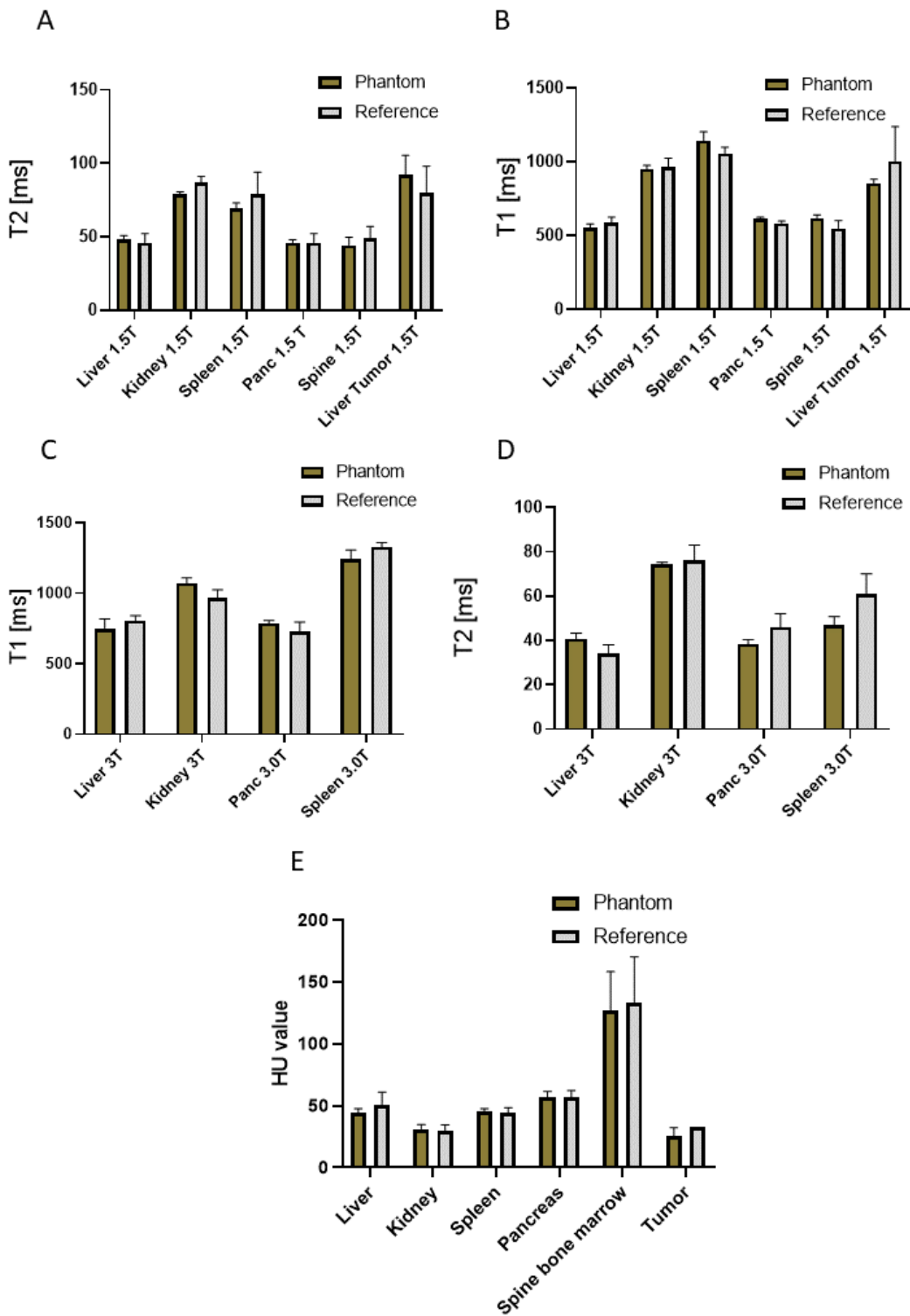


Figure 27: Comparison between the T1, T2 and HU values of the phantom organ models and reference values. The mean T1 relaxation time for 1.5 (A), for 3.0 T (C), T2 relaxation time for 1.5 (B), for 3.0 T (D) and Hounsfield unit values (E) are represented with their corresponding standard deviation in comparison to the reference values from literature (Source: Own figure).

### **3.2.1 Comparison between the phantom and patient imaging data**

As one requirement of the phantom is to provide tissue-equivalent T1 and T2 relaxation times and also a corresponding attenuation in the CT imaging, qualitative MRI and CT scans of the phantom were additionally acquired and compared with the corresponding patients and volunteer imaging data. A direct comparison of two axial and a sagittal CT scan slices between patient and phantom is depicted in figure 28. The corresponding MRI scans are displayed in figure 29 for T1w scans and in figure 30 for T2w scans, respectively. The important anthropomorphic structures are recreated inside the phantom. The simplification of the surrounding fat tissue realized in the phantom by a 0.4% agarose gel is very homogeneous compared to the patient. Nevertheless, all important structures and organs are realistically mimicked. Furthermore, the anatomical positioning of the organ models in the phantom is accurate compared to the patient scans. The overall contrasts of the organ models in comparison to the patients' tissues match very well.

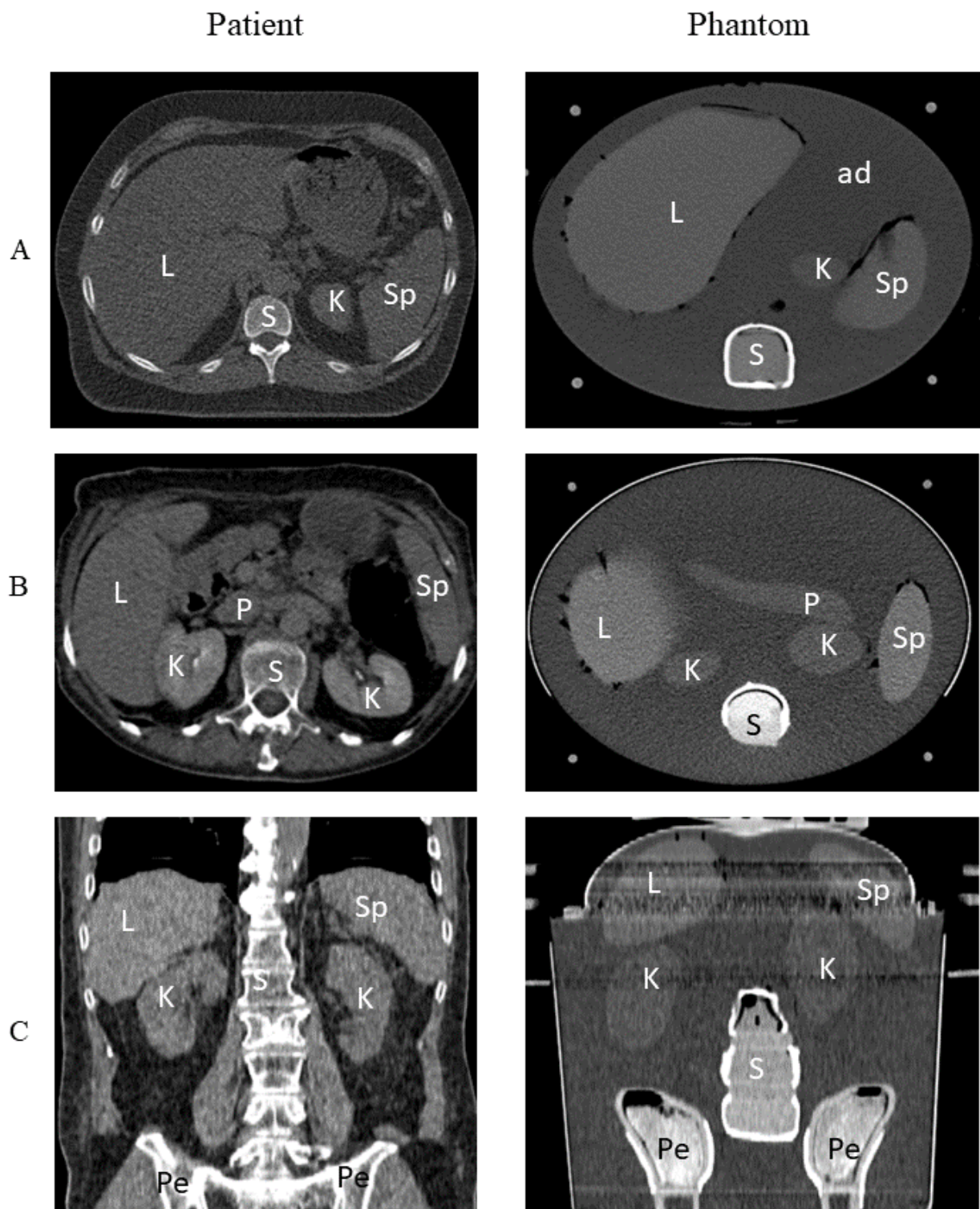


Figure 28: Comparison of axial (A and B) and coronal (C) CT scans between patient (left row) and phantom (right row). L: Liver, S: Spine, K: Kidney, Sp: Spleen, Pe: Pelvis, ad: adipose tissue (Source: Own figure).

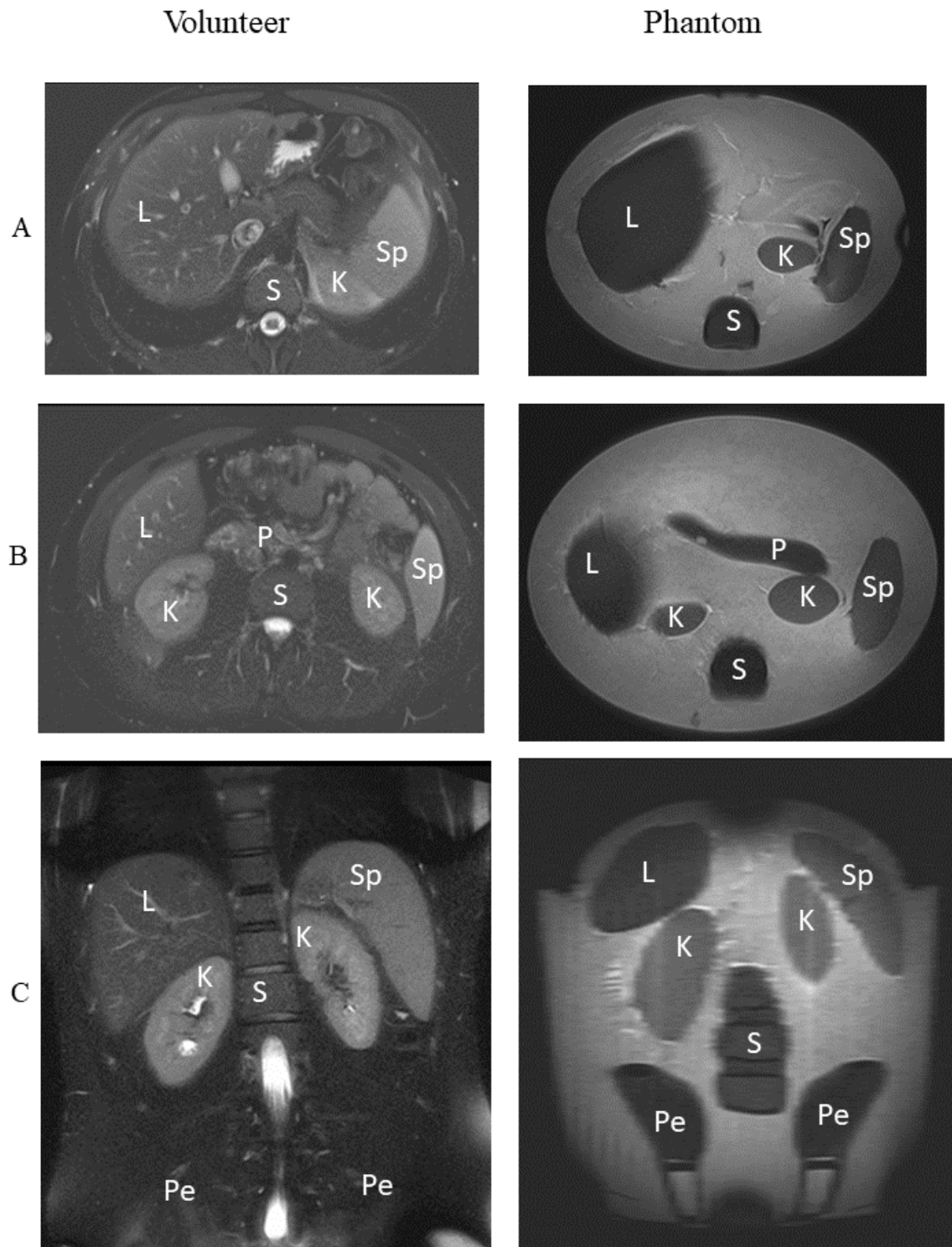


Figure 29: Comparison of axial (A and B) and coronal (C) T1w MRI scans. Volunteer scans are in the left row, phantom is in the right row (Source: Own figure).

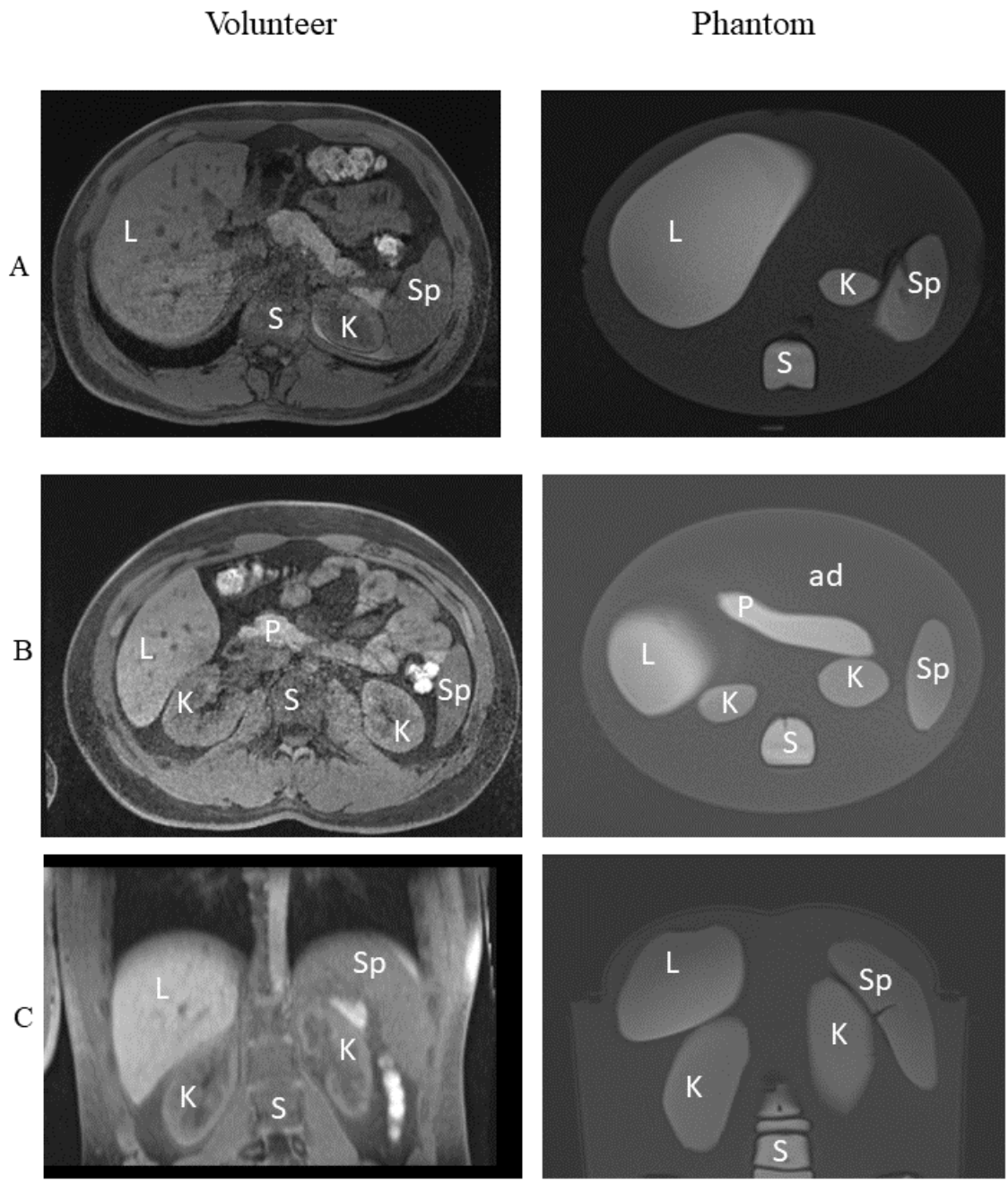


Figure 30: Comparison of axial (A), (B) and coronal (C) T2w MRI scans. Volunteer scans are in the left row, phantom is on the right (Source: Own figure).

### 3.3 Evaluation of breathing motion

#### 3.3.1 Organ motion evaluation of first experimental setup

The evaluation of the organ movement for the first experimental setup revealed a mean diaphragm movement of 11.4 for shallow, 21.7 mm for free breathing and 33.1 mm for deep breathing simulation. Additionally, the movement for the liver and both kidneys was evaluated. For the liver, a displacement amplitude of 7.2 mm in the direction of CC for shallow breathing, 13.8 mm for free breathing and 23.2 mm for deep breathing was measured. The amplitude values for the kidney were combined for both kidneys and resulted in values of 2.9 mm for shallow, 6.1 mm for free breathing and 9.5 mm for deep breathing simulation. The organ model motion showed strong dependence on the input amplitude of the diaphragm through all three breathing motions (Fig. 31 A-F). The comparison of the motion amplitudes between the phantom and a healthy volunteer does not show any significant differences for all three breathing amplitudes (table 6).

Table 7: Comparison of diaphragm, liver and kidney motion amplitudes between phantom of the first experimental setup and volunteer (Ref) for shallow, normal and deep breathing.

Breathing motion	Diaphragm [mm]	Diaphragm <sub>Ref</sub> [mm]	Liver CC [mm]	Liver <sub>Ref</sub> CC [mm]	Kidney CC [mm]	Kidney <sub>Ref</sub> CC [mm]
Shallow	11.4	11.6	7.2	7.1	2.9	3.9
Free	21.7	20.6	13.8	12.9	6.1	6.6
Deep	33.1	33.1	23.2	23.6	9.5	8.3

The relative comparison between the diaphragm motion and the organ model motion resulted in a LDMR of  $64.4 \pm 9.7\%$  for the healthy volunteer, while a LDMR of  $65.5 \pm 4.3\%$  was obtained in the phantom (Fig. 28 J). For KDMR,  $30.7 \pm 4.3\%$  was calculated for the volunteer, while  $27.5 \pm 3.1\%$  was obtained for the phantom (Fig. 28 K). No significant difference between phantom and subject was found for LDMR and KDMR for all breathing amplitudes.

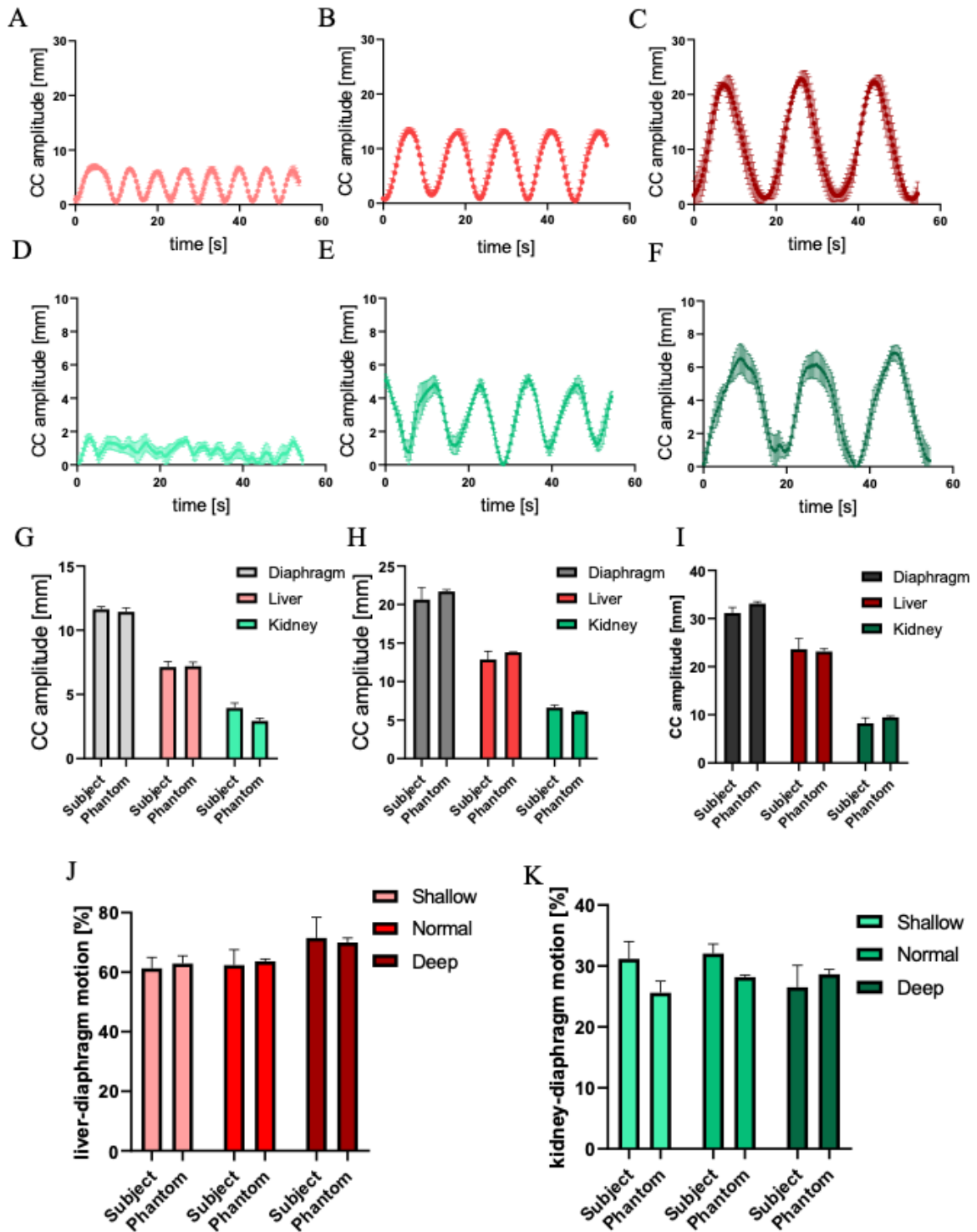


Figure 31: Motion amplitude of the phantom's liver (A, B, C) and kidneys (D, E, F) for shallow (A, D), free (B, E) and deep breathing (C, F). Comparison between the healthy volunteer and the phantom's organ motion is shown for shallow (G), for free (H) and for deep breathing amplitudes (I). Additionally, the LDMR (J) and KDMR (K) is shown as comparison between the phantom and the healthy volunteer for all three breathing amplitudes (Weidner et al. 2022).

### 3.3.2 Organ motion evaluation of the second experimental setup

The second experimental setup of the phantom, in contrast to the first, included additional organ models, such as the spleen, pancreas, a pelvis and a lumbar spine model.

As in the first experimental setup, an evaluation of the individual internal organ model was carried out. A diaphragm deflection of 11.4 mm was measured for shallow breathing motion, 20.3 mm, for free and 32.7 mm for deep, respectively. The displacements of the individual organ models for the three different breathing sequences showed no significant differences in comparison with the volunteer reference data provided in table 8 and figure 27. In addition, a comparison of the movement amplitude in cc direction obtained from the first experimental setup in comparison to the second setup was also conducted. The evaluation showed that there were no significant differences in the maximum movement of the diaphragm, liver or kidneys for either shallow (Fig. 32 A), free (Fig. 32 B) and deep (Fig. 32 C) breathing motion. Figure 33 shows a comparison between the first and second experimental setup. It compares the maximum amplitude of each organ model in CC direction during shallow (Fig. 33 A), normal (Fig. 33 B), and deep (Fig. 33 C) breathing. The result shows that there are no significant differences between experimental setup versions, which ensures reproducibility. In addition, the motion trajectory of the individual organ models was extracted and evaluated. The results show that also in this experimental setup the organ model displacement has a strong dependence on the input amplitude (Fig. 34 A-O).

Table 8: Comparison of diaphragm, liver, kidneys, spleen and pancreas motion amplitudes between phantom of the second experimental setup and volunteer (Ref) for shallow, normal and deep breathing.

Breathing motion	Diaphragm [mm]	Diaphragm <sub>Ref</sub> [mm]	Liver CC [mm]	Liver <sub>Ref</sub> CC [mm]	Kidney CC [mm]	Kidney <sub>Ref</sub> CC [mm]
Shallow	11.4	11.6	6.5	7.1	3.3	3.9
Free	20.3	20.6	11.8	12.9	5.7	6.6
Deep	32.7	33.1	21.5	23.6	11.5	8.3

Breathing motion	Spleen CC [mm]	Spleen <sub>Ref</sub> [mm]	Pancreas CC [mm]	Pancreas <sub>Ref</sub> CC [mm]
Shallow	3.3	3.1	6.5	4.4
Free	6.1	7.1	6.6	6.2
Deep	16.1	20.4	15.6	13.3

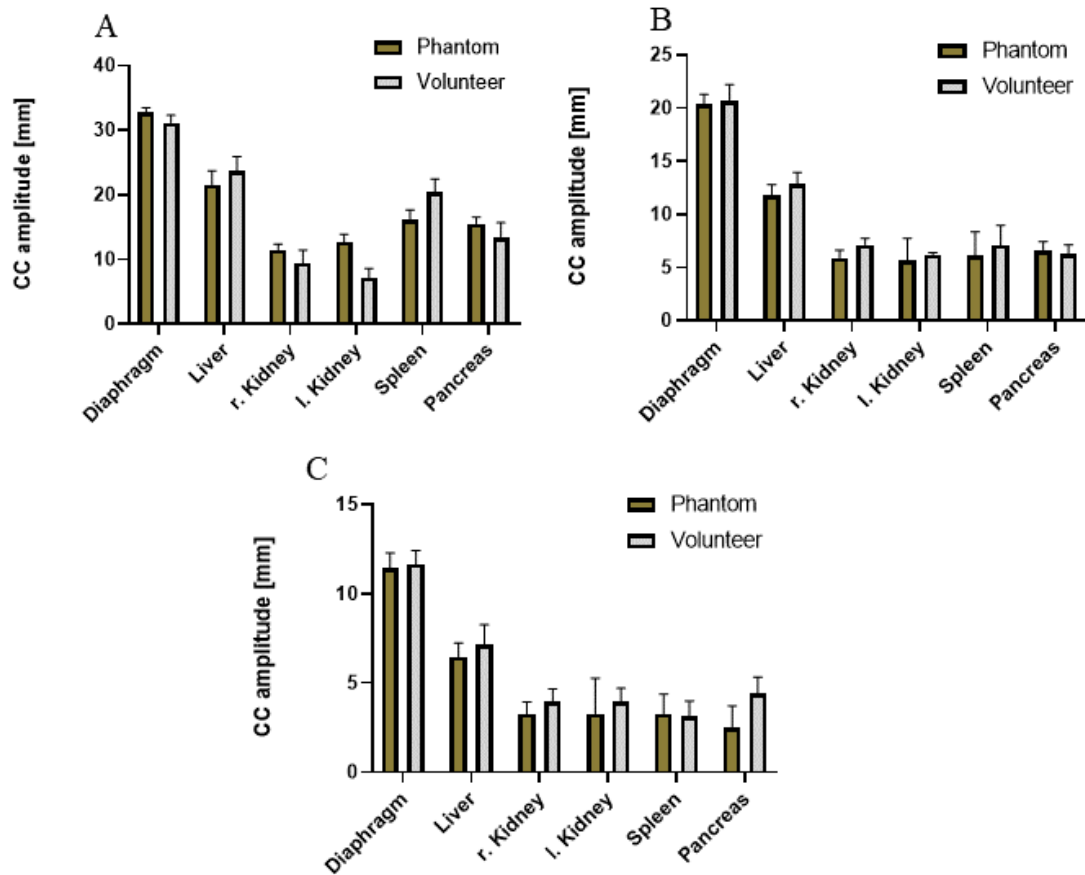


Figure 32: Comparison between second experimental setup and volunteer. The deflection amplitudes in cc direction for the diaphragm, liver and kidneys, spleen and pancreas for shallow (A), free (B) and deep (C) breathing motion (Source: Own figure).

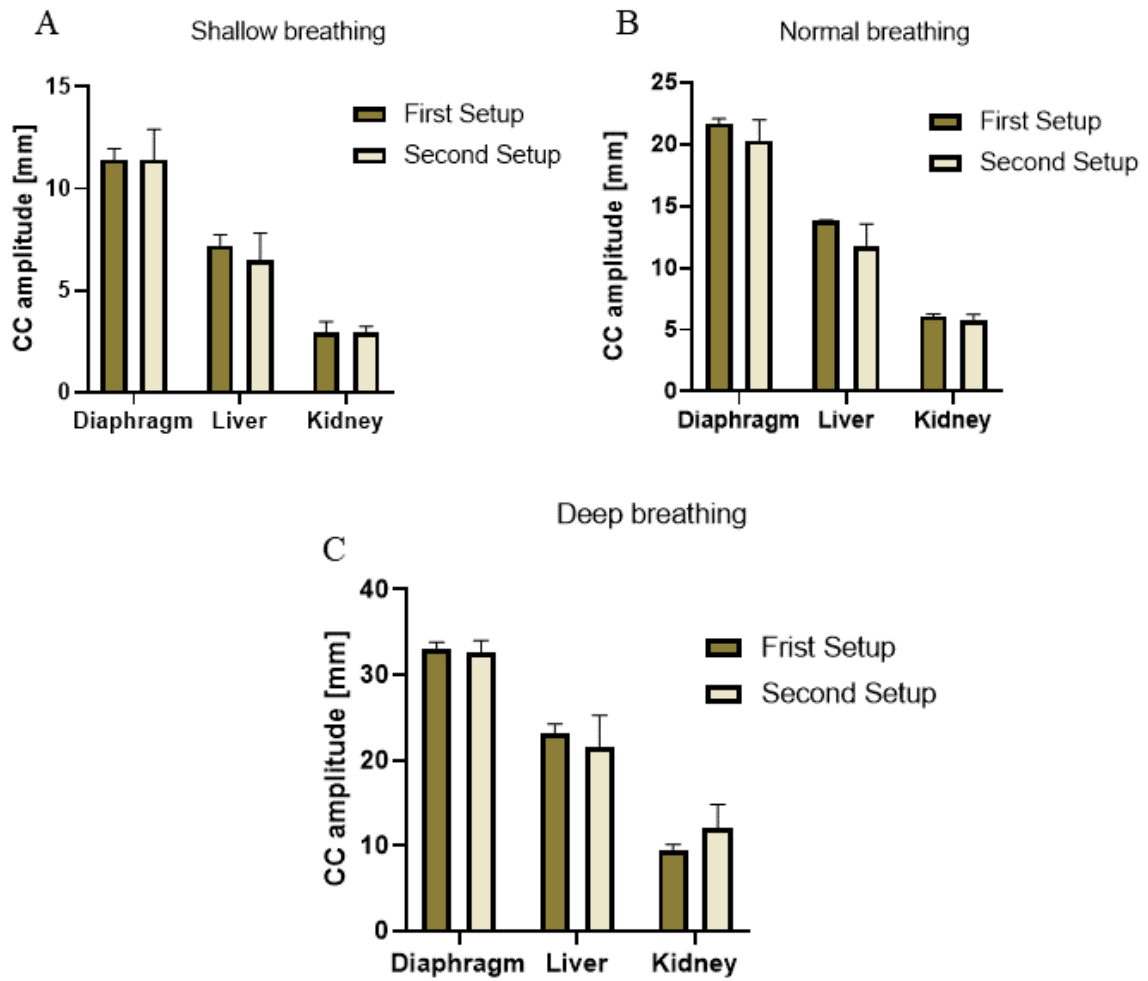


Figure 33: Comparison between the first and second experimental setup. The deflection amplitudes in cc direction for the diaphragm, liver and kidneys for shallow (A), free (B) and deep (C) breathing motion (Source: Own figure).

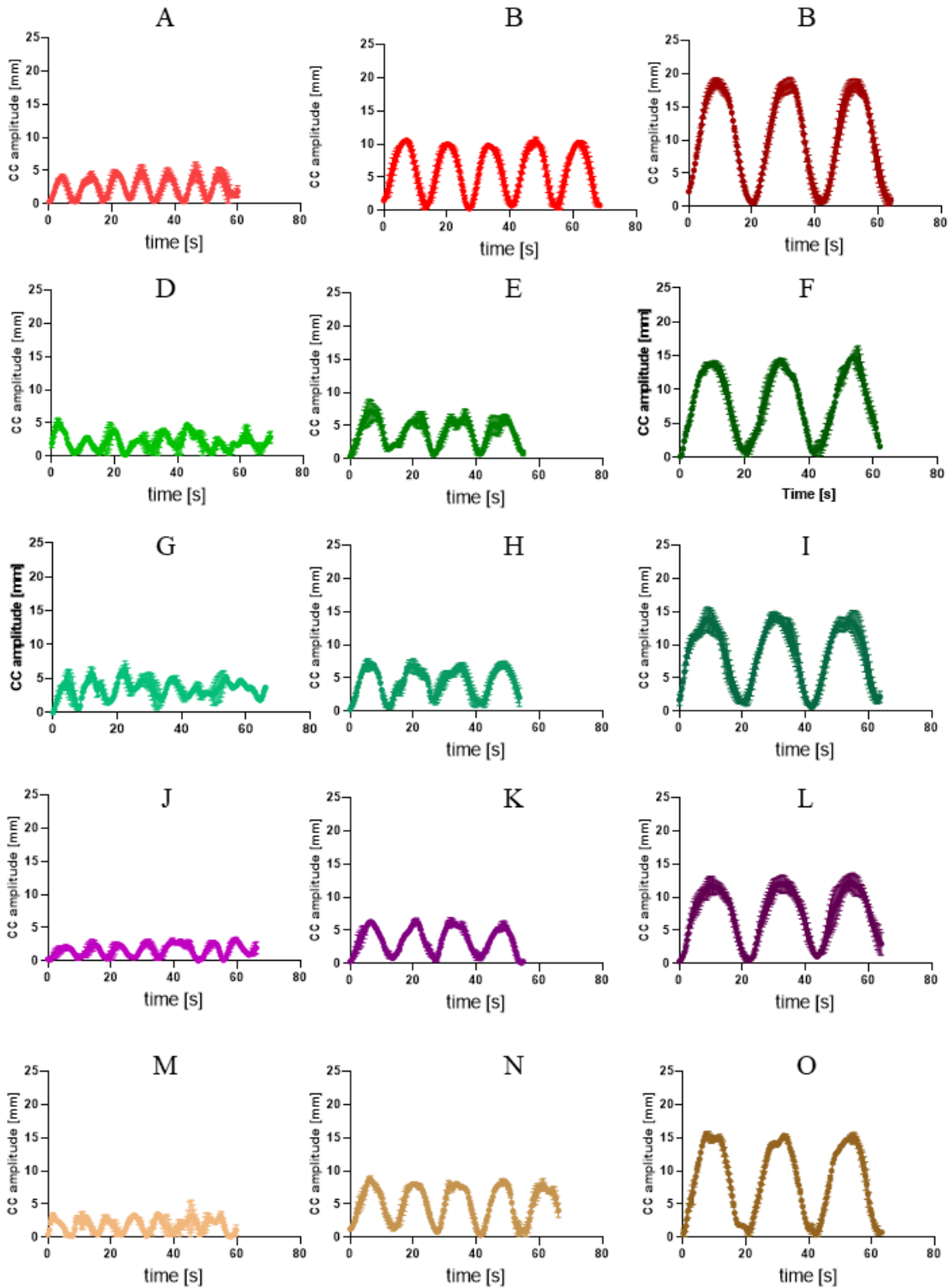


Figure 34: Movement trajectories of each organ model in cc direction. The displacement trajectory of the liver for shallow A, free B and deep C breathing motion as well as for the right kidney (D-F), left kidney (G-I), the spleen (J-L), and the pancreas (M-O) (Source: Own figure).

In addition to the healthy volunteer imaging data, anonymized patient respiratory data from PACS was also analyzed. However, these CT scans were static and different expiration and inspiration phases were automatically detected and scanned. For comparison with organ shifts in the phantom, the maximum amplitudes of the individual organs were therefore evaluated from the patient data. Since it can be assumed that the patient data were recorded during free breathing with breathing commands, a comparison to the amplitudes of the free phantom breathing is carried out in this case. The comparison between the cohort of 10 patients and the phantoms free breathing motion revealed no significant differences for all organ amplitudes (Fig. 35). It can also be observed, that the standard deviation of the patients data is higher than the phantoms.

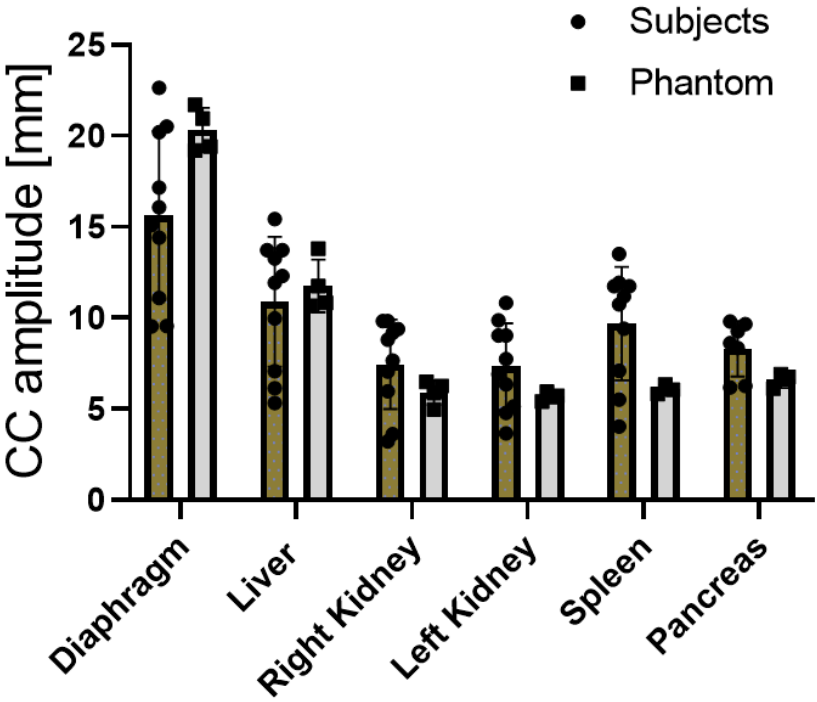


Figure 35: Comparison of the breathing motion during free breathing in the phantom to the patient data gathered from PACS (Source: Own figure).

As already calculated in the first experimental setup, the relative motion of the organ models compared to the diaphragm motion, was also carried out for the second setup. As LDMR (Fig. 36 A) a percentage of  $60.61 \pm 9 \%$  was calculated. For the KDMR (Fig. 36 B) a value of  $31 \pm 9.2 \%$ , for SDMR (Fig. 36 C) of  $36 \pm 9 \%$  and PDMR (Fig. 36 D) of  $34.4 \pm 12.3 \%$  was evaluated for the phantom. Since the LDMR and KDMR

for volunteer was already calculated and specified when comparing with the first setup, this value was adopted. In addition, the SDMR and PDRM were calculated. The SDMR resulted in  $38 \pm 19\%$  and the PDRM in  $36.5 \pm 10.4 \%$ . In comparison to the phantom the organ to diaphragm motion ration of the healthy volunteer shows no significant difference throughout all breathing amplitudes.

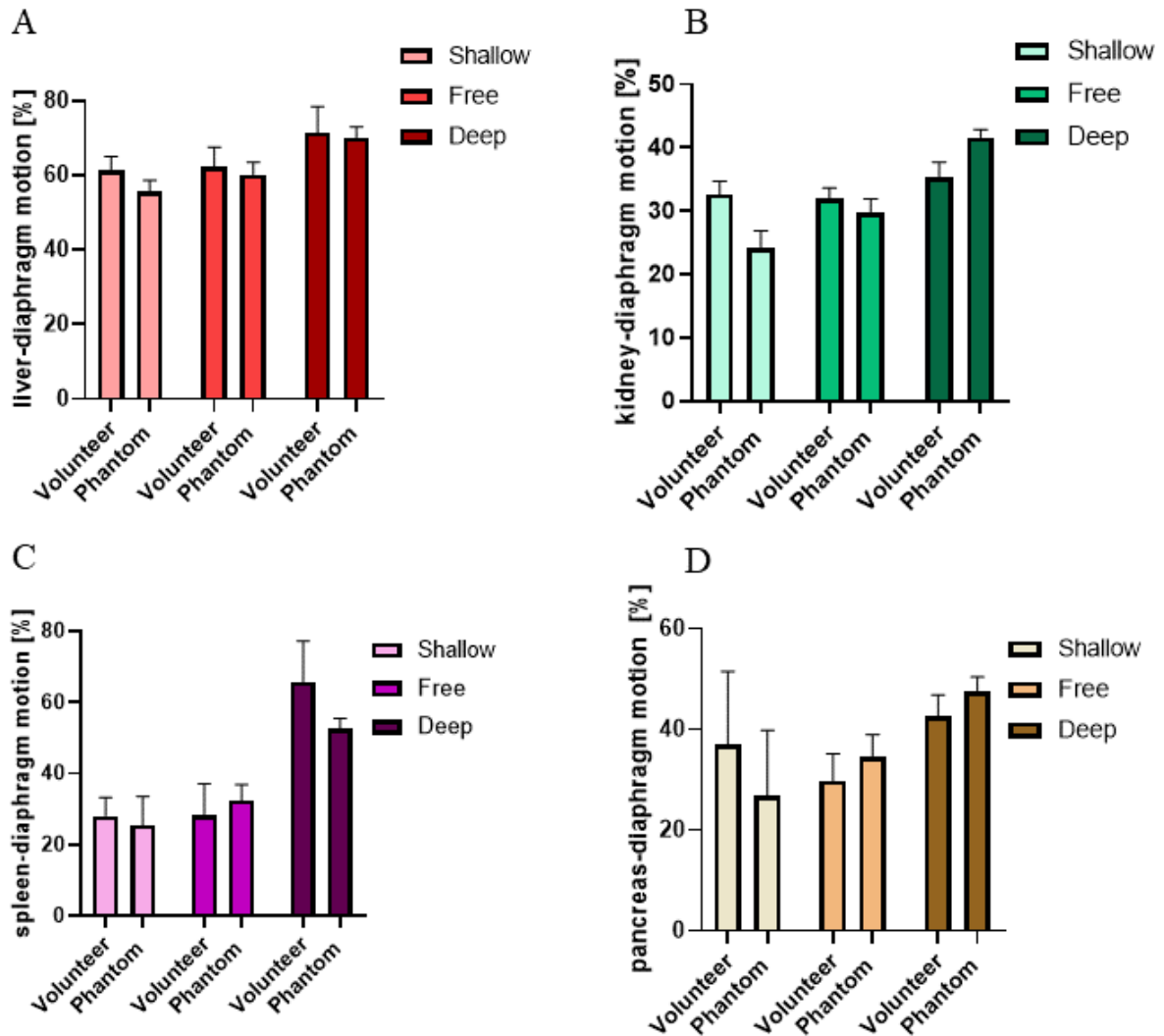


Figure 36: Comparison of the LDRM (A), KDMR (B), SDMR (C) and the PDRM (D) between the phantom and the volunteer for all three breathing amplitudes (Source: Own figure).

Besides static and dynamic scans for the analyzation of respiration-induced organ movement, newly developed sequences were also used that perform automatic movement detection. One of these sequences is the starVIBE 991, which automatically detects the diaphragm movement and then generates five different breathing phases in so-called bins. This sequence was used to acquire imaging data of the volunteers' deep

breathing motion as well as the phantoms'. The evaluation of the volunteer data as well as the phantom shows that the breathing motion could be detected and also different breathing levels were assigned to individual bins (Fig. 37). For the phantom, two identical measurement were performed on two different days to investigate the reproducibility of the phantoms organ motion. These two different scans are shown in the graphs as phantom 1 and phantom 2. The different bins for phantom 1 and 2 are detected almost identically for all organ models. Furthermore, compared to the volunteer, it can be observed that the maximum amplitude in particular shows only very slight differences.

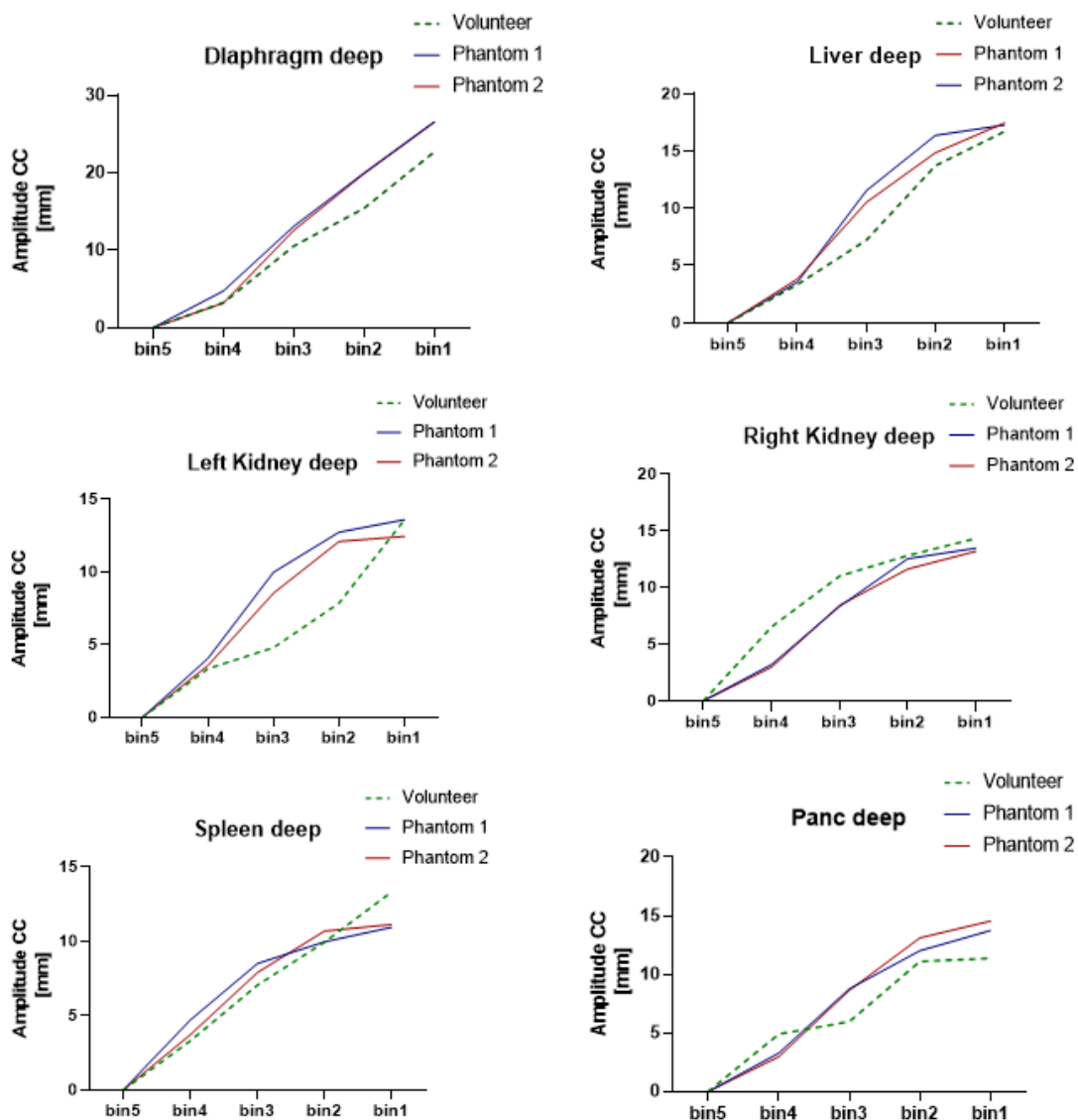


Figure 37: Comparison of the bin1 to bin 5 for the different organs between volunteer and phantom for deep breathing motion (Source: Own figure).

### **3.3.3 End-to-end test with breathing motion and a liver tumor model**

For the end-to-end test, the third experimental setup was used. For this purpose, a new modified liver was utilized, which allows the insertion of a tumor model in the shape of a sphere with a diameter of 30 mm. An EBT3 film with dimensions of 20 x 20 mm was then placed exactly in the center of this sphere. Afterwards planning CT scans were carried out in order to subsequently create a radiation planning for the phantom. Unfortunately, an incorrect orientation of the phantom was chosen during the preparation of the planning CT scans, therefore the phantom is upside down on the radiation planning figures. Figure 38 (A) shows an axial slice through the phantom in which the tumor model, the liver (L) and the spleen (S) are shown. The tumor model has been contoured with a green circle demonstrating the planning target volume (PTV). The safety margin is represented by the red circles around the PTV. Figure 38 (B) shows an axial, sagittal and coronal section through the phantom. All organ models such as the spine model, the pelvis and kidneys were also contoured. In addition, the phantom container, the frame and adapters attached to the phantom were contoured in the treatment planning software in order to be taken into account for the plan calculation.

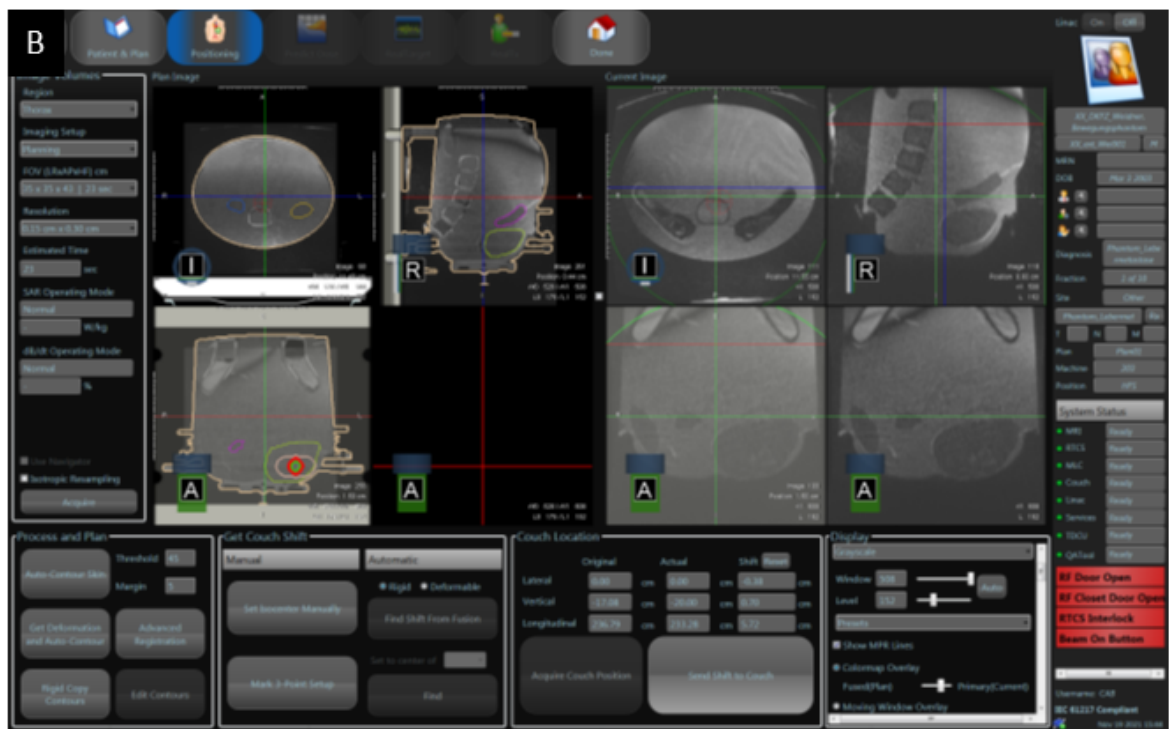
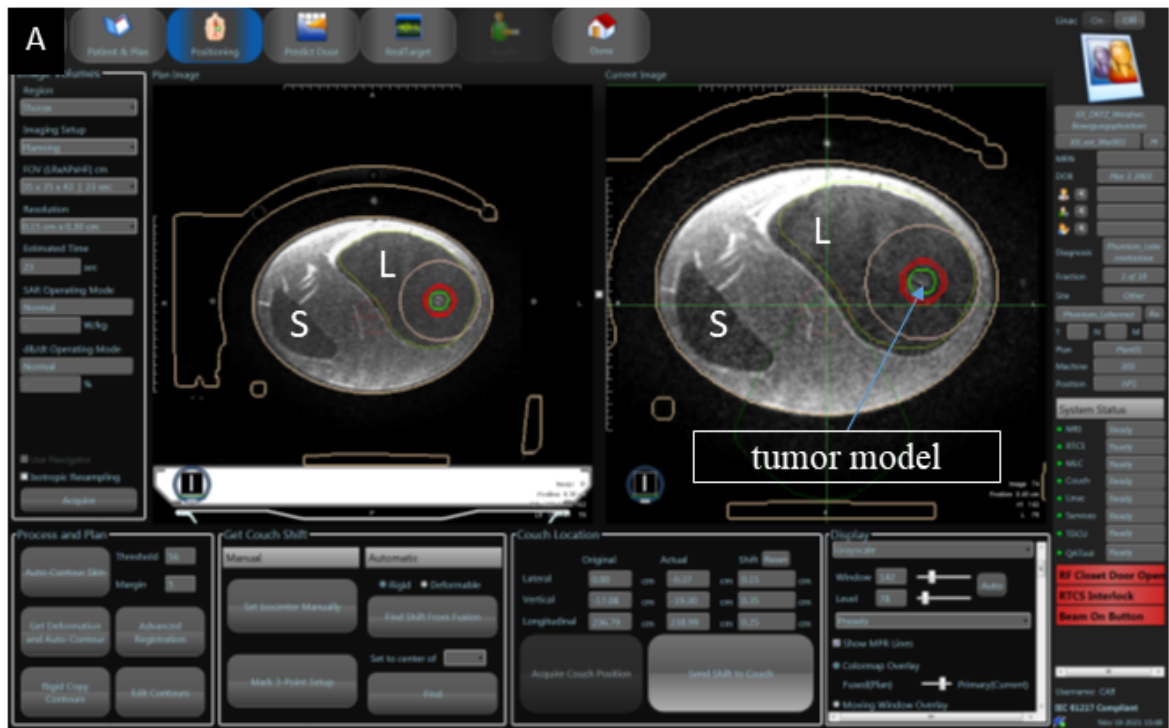


Figure 38: Treatment plan with contoured tumor model (green circle), safety margins (red circles) and all considered structures A. Axial, sagittal and coronal slice through the phantom showing contoured organ models and structures (Source: Own figure).

Furthermore, the automatic detection and contouring of the organ shapes of the phantom was possible by the software and required only minor manual adjustments. However, these are also necessary for the radiation planning of patients. An important requirement for the phantom was that it could be used with the MR-Linac and is capable of breathing simulation. This requirement could be fulfilled by a hydraulic drive that is entirely free of ferrous materials (Fig. 39).



Figure 39: The abdominal phantom is positioned on the patient couch in front of the MR Linac inside the MR-Linac treatment room (Source: Own figure).

As prescription dose per fraction for the PTV a dose of 5 Gy to 95% per fraction were chosen. To apply this dose to the tumor volume, a total of 11 beams were calculated, each delivering a certain dose from 11 different gantry angles. Since the irradiation at the MR-Linac is gated, a modified deep breathing sequence was used for this experiment. For this purpose, a breath-holding phase of 10s was incorporated into the movement trajectory so that gating could be enabled. As shown by the irradiation of the phantom, the tumor model in the liver could be detected by MRI imaging during irradiation. As soon as the tumor model (red circle) moved outside the defined

boundaries (yellow circle) due to respiration (Fig. 40 left), the irradiation was immediately interrupted. Only when the tumor was again within the defined boundary, the irradiation was continued (Fig. 40 right).

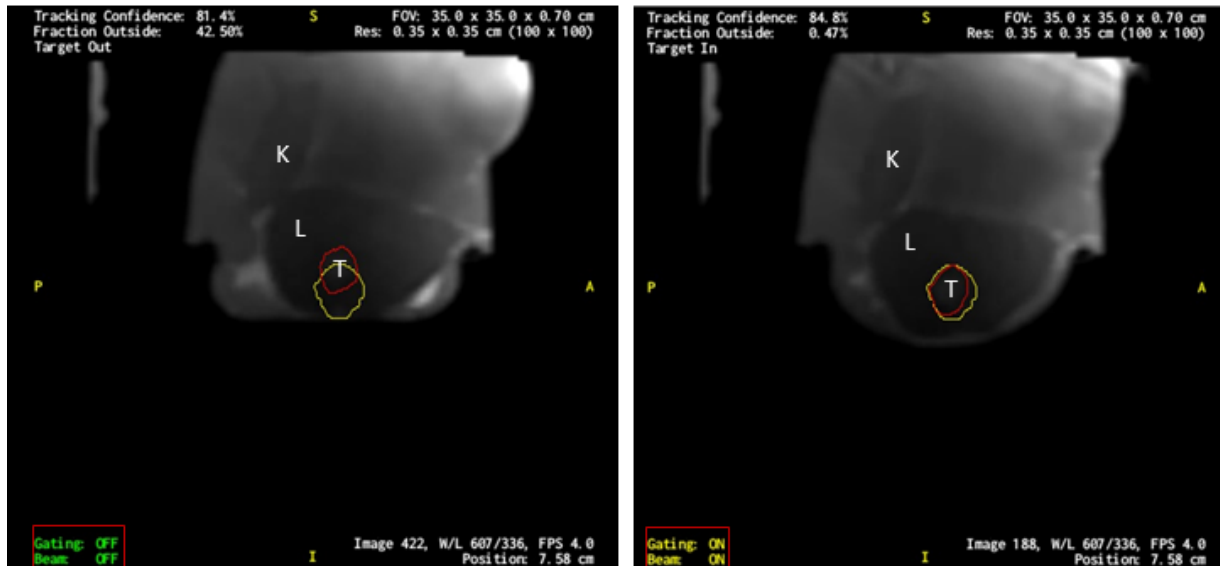


Figure 40 Irradiation of the tumor model using gating at the MR-Linac. Tumor model is partially outside the defined boundaries therefore, the irradiation stopped (left). On the right: beam is on as long as the tumor is inside the defined boundaries. K: Kidney, L: Liver, T: Tumor model (Source: Own figure).

After irradiation of the phantom, the EBT3 films required to calculate the calibration curve were irradiated. For this, a total of eight equally sized EBT3 films with dimensions of 30 x 30 mm were irradiated between RW3 plates at a depth of 5 cm, a source to surface distance (SSD) of 85 cm and a field size of 5 x 5 cm. Each film was irradiated with a different dose except for the first film with 0 Gy. The exact dose values that were applied to calibration films are shown in figure 41. It is very clearly visible that with increasing dose, the optical density of the film also changes.

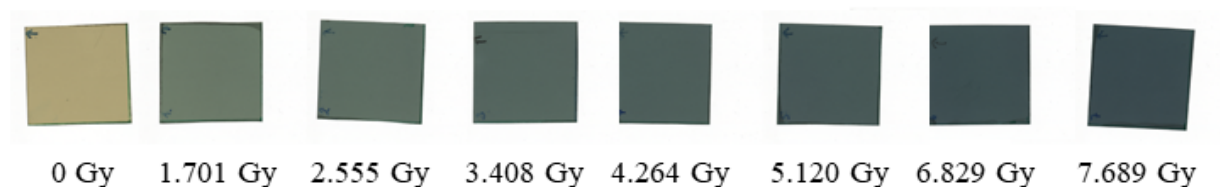


Figure 41: EBT3 Film irradiation with different dose from 0 Gy to 7.689 Gy in order to calculate the calibration curve (Source: Own figure).

The EBT 3 film inside the tumor model as well as the films irradiated for the calibration, were stored protected from light in an envelope. 48 hours after the irradiation, the films were scanned and analyzed with an in house developed MATLAB script. The dose evaluation considered also the offset that was generated by the planning CT and the manufacturing process.

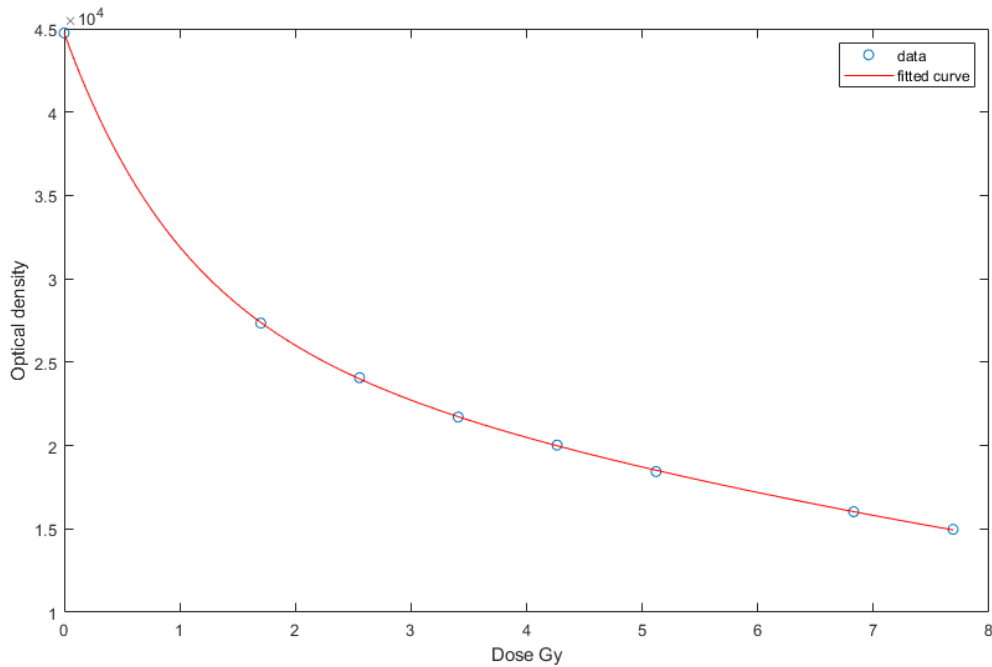


Figure 42: Calculated calibration curve. Optical density values are plotted over the corresponding gray values (Source: Own figure).

The calculated calibration curve in figure 37 was also used to determine the dose values of the offsets. Thus, a mean dose value of  $2.46 \pm 0.08$  Gy was determined for the manufacturing offset and 0.63 Gy for the planning CT offset. As indicated in figure 43 uniform rectangles with the size of 13 x 13 mm were used as ROIs for the calculation of all offset films. Taking into account the calculated offset values, the dose of the film located in the tumor model was determined. Lying a ROI 13x13 mm in the middle of the film a dose of  $5.3 \pm 0.42$  Gy was calculated.

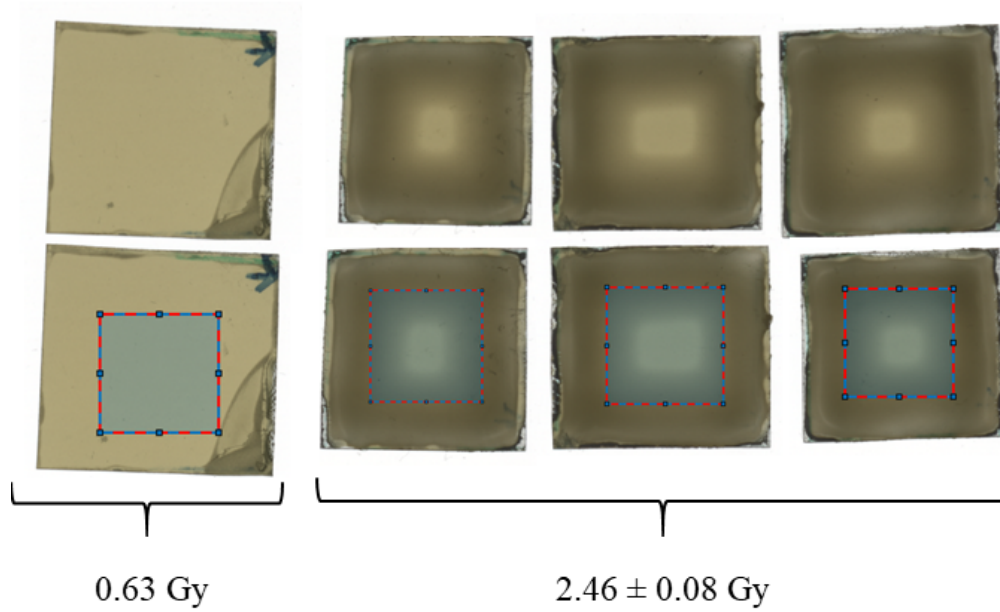


Figure 43: Evaluated offset value of 0.63 Gy for the planning CT and a mean of  $2.46 \pm 0.08$  Gy for the manufacturing process (Source: Own figure).

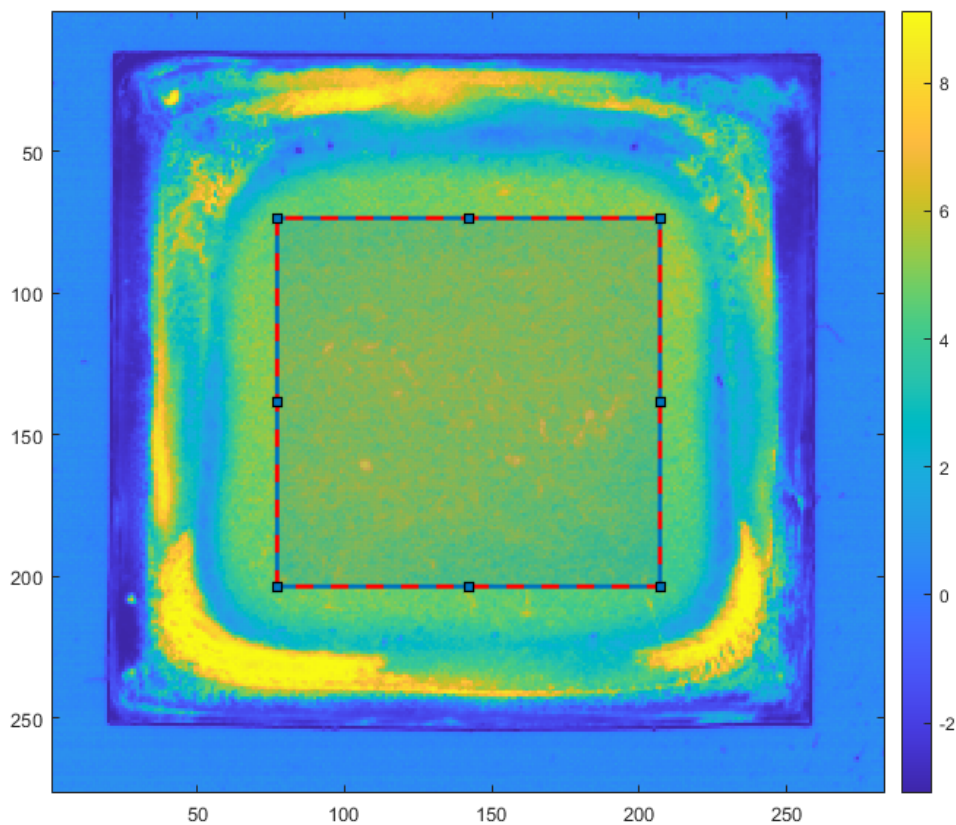


Figure 44: A 13 x 13 mm ROI is placed in the middle of the tumor ET3 film. The colored bar on the right side indicates the dose values in Gray to the corresponding colors in the graph (Source: Own figure).

## 4 Discussion

### 4.1 Long-term experiment

The evaluation of the contrast stability phantom provides important insights into the behavior of two types of contrast agents: OEAMs and AMs. This study investigates the impact of foil protection on the stability of T1 and T2 contrast over an extended period of 166 days.

The results demonstrate a visible decrease in T1 contrast for both OEAMs and AMs without foil protection after 166 days, as shown in figure 22 A. This decrease is evident even as early as 2 hours after preparation, as indicated by the qualitative T1-weighted image. However, no loss in T2 contrast is observed, suggesting that the foil protection primarily affects T1 contrast stability.

In contrast, the OEAMs and AMs sealed with foil exhibit no visible difference in T1 contrast compared to their initial state. Additionally, there is no significant difference in T2 contrast for the sealed samples. These findings suggest that the foil protection effectively prevents the deterioration of T1 contrast over time.

Interestingly, a significant increase in quantitative T1 relaxation time is observed for OEAM1 and OEAM2, with values of 43.26% and 49.97% respectively, one day after preparation (Fig. 22 C). In contrast, AM1 and AM2 demonstrate a reduction in T1 relaxation time of 51.33% and 32.84% respectively (Fig. 10 C). These results indicate variations in T1 relaxation behavior between the different artifact types.

Further analysis revealed a complete ion exchange of Ni-DTPA, a contrast agent used in the phantom, after 21 days. This suggests that the contrast agents undergo significant changes over time, which can impact their stability and effectiveness in providing consistent contrast.

Comparing the vessels with foil protection to those without, the vessels with foil shows stable T1 contrast over time. Additionally, the change in T1 relaxation time for OEAM1, OEAM2, AM1, and AM2 is non-significant, with variations of less than 10% (Fig. 22 D).

Overall, this experiment highlights the importance of foil protection in maintaining the stability of T1 contrast for OEAMs and AMs. It also underscores the dynamic nature of contrast agents, with changes observed in T1 relaxation times and ion exchange over time. These findings contribute to our understanding of contrast agent behavior and inform strategies for optimizing contrast stability in medical imaging applications.

## 4.2 Temporal contrast stability of organ models

The discussion in this chapter focuses on the temporal contrast stability of organ models used in the contrast stability phantom experiments. The organs were packed and vacuum sealed in foil to ensure stable T1 and T2 relaxation times throughout the duration of the experiments.

By maintaining the same organ models for at least 60 days across all experiments, the study aimed to assess the long-term stability of T1 and T2 relaxation times. It should be noted that additional organ models were manufactured only for new versions of the experimental setup, ensuring consistency in the evaluation process.

The results of the evaluation demonstrate that covering the organs in foil effectively preserves their temporal contrast stability. For the organ models prepared for 1.5T, the analysis reveals a non-significant change of less than 4.5% for the T2 relaxation time and less than 2.6% for the T1 relaxation time. This suggests that the foil protection successfully maintains the stability of both T1 and T2 contrast over time.

In comparison, the organ models prepared for 3.0T exhibit slightly higher changes in relaxation times, but still within an acceptable range. The calculated non-significant change is less than 0.8% for the T1 relaxation time and 7.6% for T2 relaxation time. Although there is a slightly larger variation for T2 relaxation time in the organs prepared for 3.0 T, it remains within an acceptable limit.

The evaluation of quantitative T1 and T2 relaxation times further supports the findings of stable contrast over time. No significant changes are observed, indicating that the foil-covered organ models maintain consistent relaxation times throughout the experiments.

Figure 18 provides a visual representation of the T1 and T2 relaxation time changes for each individual organ model prepared for either 1.5T or 3.0T. The specific points in time at which additional measurements were taken are indicated above the corresponding bar. This information helps to identify any potential trends or variations in relaxation times for specific organ models over time.

Overall, the chapter emphasizes the effectiveness of foil coverage in ensuring the temporal contrast stability of the organ models used in the phantom experiments. The results demonstrate that the foil protection minimizes changes in T1 and T2 relaxation times, providing reliable and consistent contrast for both 1.5T and 3.0T preparations. These findings contribute to the development of techniques and protocols for maintaining stable contrast in various imaging scenarios.

### **4.3 Evaluation of organ models for experiments**

This result conducts quantitative relaxation times (T1 and T2) and HU values for different organ models at both 1.5T and 3.0T MRI settings. These measurements are essential, as they reflect the physical properties of the organ models and their responses to different magnetic field strengths. The HU values from CT scans are also important, as they relate to the attenuation of X-rays and play a critical role in CT imaging. The presented data is compared to reference values, which are average values established for typical human tissues. The results show that the measured T1 and T2 relaxation times for the liver and kidney models used in the experiments are in close agreement with the reference values for both 1.5T and 3.0T MRI settings. This indicates that the organ models effectively mimic the relaxation characteristics of real human organs under different MRI field strengths. In this thesis, HU values for the organ models were also evaluated using CT. HU values are crucial for quantifying tissue density in CT scans. The results reveal that the measured HU values for the organ models match well with reference values. This suggests that the organ models provide realistic CT representations, which is vital for the calculation of radiation treatment plans and imaging procedures. It is worth noting that the organ models remained the same for subsequent experimental setups. To enhance the clarity of the results and facilitate comparison, the chapter includes figure 24, displaying the relaxation times and HU values in relation to the reference values. This graphical representation aids in visualizing any potential variations or deviations. The inclusion of standard deviation provides a measure of the data's dispersion and offers insights into the variability of the measurements.

### **4.4 Comparison between the phantom's MRI and CT imaging data**

The primary requirement for the abdominal phantom is to mimic tissue-equivalent T1 and T2 relaxation times, as well as attenuation values in CT imaging. The qualitative MRI and CT scans performed in the context of this thesis show that the phantom successfully accomplishes this. This is a critical achievement, as it ensures that the phantom accurately simulates the radiological characteristics of human tissues, which

is vital for various medical imaging procedures. The results show a direct comparison of axial and sagittal CT scan slices between patients and the phantom. These visual comparisons are valuable, as they clearly demonstrate how well the phantom mimics the patients organ anatomy. The corresponding MRI scans (T1w and T2w) are also compared, which is important because MRI and CT scans are widely used for different clinical purposes. The evaluation of the comparison underscores that while the phantom employs a 0.4% agarose gel to simplify the representation of surrounding fat tissue, it still results in a relatively homogeneous model. It is worth noting that some human tissues are inherently inhomogeneous, and the presence of air resulting from different intestinal filling introduces further complexity to the human body, leading to a more heterogeneous image compared to the phantom. Despite these simplifications for practical reasons, the phantom successfully recreates the overall anatomical structures and organs at risk. This is fundamental for ensuring that medical imaging techniques can be tested and optimized with a reasonable degree of fidelity to the complexity of real human tissues, even though it cannot fully replicate the full heterogeneity of *in vivo* conditions. Another significant finding is that the anatomical positioning of the organ models within the phantom closely matches the patient scans. This accuracy is crucial for validating the phantom's usefulness in simulating specific clinical scenarios where precise organ positioning is essential. This work also underlines that the overall contrasts of the organ models in the phantom closely match those of the patients' tissues. This is particularly important for ensuring that the phantom can accurately represent the differences in tissue densities and compositions that are vital for medical diagnoses.

#### **4.5 Organ motion of the 1st experimental setup**

The results show that the diaphragm's movement significantly increases with the depth of breathing, which is to be expected. The liver and kidney also exhibit larger displacements during deep breathing. This information is important for medical imaging and treatment planning, as organ motion can affect the accuracy of radiation therapy and imaging techniques. The motion comparison between the phantom and the volunteer data is essential for validating the phantom's suitability for simulating human organ movements. The results indicate that there are no significant differences in the motion amplitudes between the phantom and the volunteer for all three breathing patterns. This is a positive result, suggesting that the phantom is a suitable

representation of human organ motion in this context. These ratios KDMR and LDMR are used to quantify the relative motion between organs. The comparison reveals that there are no significant differences between the phantom and the healthy volunteer for LDMR and KDMR across all breathing patterns. This further reinforces the validity of the phantom as a representation of human organ motion. The findings have significant implications for various medical applications, such as radiation therapy and diagnostic imaging. If the phantom accurately mimics the organ motion of a healthy individual, it can be used for testing and optimizing these techniques without the need for real patients. This can help reduce the potential risks and uncertainties associated with such procedures. It is important to acknowledge the limitations of the study. The results are based on a single healthy volunteer, and a larger sample size may be needed to establish broader generalizability. Additionally, the study does not explore potential differences in organ motion based on factors like age, gender, or health conditions. Future research could delve into these aspects for a more comprehensive understanding.

#### **4.6 Evaluation of the 2nd experimental setup**

Using the second experimental setup, the movements of various internal organ models, including the diaphragm, liver, kidneys, spleen, and pancreas, were analyzed during different types of breathing motions, such as shallow, free, and deep breathing. These measurements are essential for understanding how organs shift and deform with respiration. The results indicate that the measured displacements of individual organ models during breathing sequences exhibit no significant differences in comparison to volunteer reference data. This finding suggests that the phantom effectively mimics the organ motion observed in real human subjects. It underscores the suitability of the phantom as a representation of human anatomy for experimentation and validation purposes. Furthermore, the reproducibility of the phantom's organ motion was investigated by conducting identical measurements on two different days. This evaluation showcases the consistency of organ motion patterns between different scans on different days. Furthermore, a comparative analysis between the first and second experimental setups was conducted to assess the reproducibility of results. This comparison revealed no significant differences in the maximum movement amplitudes of organ models, including the diaphragm, liver, and kidneys, across shallow, normal, and deep breathing motions as illustrated in figure 33. The consistency observed

between experimental setups underscores the reliability and robustness of the experimental methodology employed.

Comparisons with volunteer data showed slight differences in maximum amplitude but an overall alignment in movement patterns. The scope of the study was expanded by comparing the organ movement data obtained from the phantom with anonymized patient data. The results showed that the maximum amplitudes of individual organs from the patient data align closely with the free breathing motion of the phantom. This demonstrates that the phantom's motion is comparable to patient data and can serve as an effective tool for clinical simulations. Additionally, the relative organ motion was calculated. Therefore, the motion of organ models was compared to diaphragm motion, expressed as LDMR, KDMR, SDMR, and PDMR. These ratios provide insights into how organs move in relation to the diaphragm. The analysis demonstrated that the phantom closely resembles the relative organ motion observed in healthy volunteers during different breathing amplitudes.

#### **4.6.1 Automatic movement detection using starVIBE 991 sequence**

Considering the starVIBE 991 bin measurement results, it is evident that the maximum amplitude between phantoms 1 and 2 and the volunteer exhibits minimal variation, suggesting a high level of comparability between the phantom and the volunteer. Furthermore, a notable consistency is observed within the individual bins for phantoms 1 and 2, indicating good reproducibility in the design and construction of the phantom. Upon closer examination of the left kidney, disparities are identified in bins 3 and 2 when compared to the corresponding bins of the phantom (Fig. 45 A). This divergence may be attributed to nuanced differences in the movement patterns of the phantom, particularly in the left kidney, in contrast to that of the patient. However, when assessing other organs, particularly the right kidney, smaller differences are noted (Fig. 45 B), with the spleen exhibiting notably similar movement patterns (Fig. 45 C). In summary, the phantom demonstrates suitability for simulating various breathing positions, as these can be detected sufficiently by the starVIBE 991 sequence. Moreover, these simulations align well with the volunteer's deep breathing patterns, establishing a basis for effective comparability.

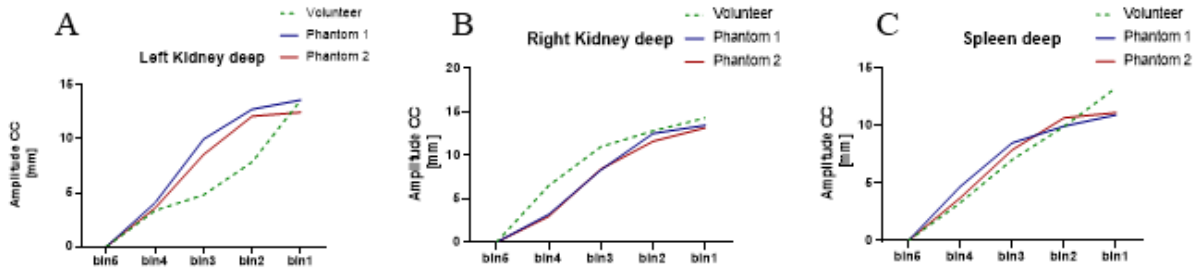


Figure 45: Evaluation of detected bins for deep breathing for the left (A) and right (B) kidney and for the spleen (C) (Source: Own figure).

## 4.7 End-to-end test

In the end-to-end test, it was possible to employ software for the automatic detection and contouring of organ shapes within the phantom using the imaging data of previously acquired planning CT images. This is a decisive step in radiation therapy planning, as it allows for precise targeting and treatment of tumors. The ability to contour organs with only minor manual adjustments demonstrates the effectiveness of the phantom in replicating human anatomical structures. It also underlines the phantom's potential as a tool for simulating radiation therapy processes. This thesis also emphasizes that the phantom fulfils a vital requirement by being compatible with the MR-Linac and is capable of simulating breathing. This is a significant advantage, as it allows for the development and testing of radiation therapy techniques under conditions that closely resemble clinical practice. The use of a hydraulic drive that is free of ferrous materials ensures that the phantom is suitable for MR-guided radiation therapy. Additionally, this thesis outlines the radiation planning process, including the choice of a prescription dose per fraction for the PTV. It is notable that a modified deep breathing sequence was used for the experiment, incorporating a breath-holding phase to enable gating. Gating is a technique that synchronizes radiation delivery with the respiratory cycle to minimize organ motion during treatment. The ability to implement gating with the phantom allows for testing and optimization of this technology. The immediate interruption of irradiation when the tumor moves outside the defined boundaries demonstrates that the phantom provides a suitable imaging contrast and a breathing movement of the organs similar to a human being, and this could be detected very accurately and reliably by the gating system. An important aspect of the analysis is the consideration of offsets. These offsets can be generated

during the planning CT scan and the manufacturing process. The offsets are essential for ensuring that the calculated dose values accurately reflect the delivered dose. The study determined a mean dose value of 2.46 Gy, with a small uncertainty of 0.08 Gy for the manufacturing offset and 0.63 Gy for the planning CT offset, as shown in figure 38. Uniform rectangles with a size of 13 x 13 mm were employed as ROI for calculating these offset values. Accounting for these offsets is an important step in dose quantification. After accounting for the offsets, the study determined the dose for the film located within the tumor model. A 13x13 mm ROI in the middle of the film was chosen for dose calculation. The calculated dose within the tumor model was determined to be 5.3 Gy, with a small uncertainty of 0.42 Gy.

In summary, this end-to-end test not only validates the capabilities of the phantom in replicating clinical scenarios but also underscores its significance as a tool for research, testing, and quality assurance in the field of radiation therapy. The successful integration of MR-Linac compatibility, breathing simulation, real-time tumor tracking, and precise dose calibration positions the phantom as a valuable asset for advancing radiation therapy techniques and ensuring the delivery of safe and effective treatments to patients. These findings contribute to the ongoing progress in the field of medical physics and radiation therapy.

## 5 Conclusion

In conclusion, this thesis has provided robust evidence of the capabilities and utility of the phantom in various medical imaging and radiation therapy applications. The organ models used in the experiments effectively replicate the relaxation times and HU values of real human organs, validating the suitability of the phantom for medical imaging research. The close agreement with reference values underscores the reliability of the phantom for testing and optimizing MRI and CT imaging techniques. The comparison of the phantom with patient and volunteer data demonstrates its ability to faithfully replicate tissue properties, anatomical structures, and radiological characteristics. This validation is a crucial step in establishing the phantom's utility for calibration, quality control, and optimization of medical imaging techniques. The assessment of organ motion during different breathing patterns highlights the phantom's ability to accurately mimic human organ motion. The results emphasize the importance of considering organ motion in treatment planning and imaging procedures. Furthermore, the comprehensive assessment of organ motion in the first and second experimental setups demonstrates the phantom's capability to accurately replicate respiratory-induced motion observed in real human subjects. The phantom's consistency and reproducibility over time, along with its strong agreement with patient data, validate its utility as a reliable tool for medical imaging research and experimentation. In summary, this thesis not only validates the capabilities of the phantom in replicating clinical scenarios but also underscores its significance as a tool for research, testing, and quality assurance in the fields of medical physics, radiation therapy, and medical imaging. The evaluation of the end-to-end test utilizing radiation planning and dose calculation using a modified liver phantom demonstrates the potential of the phantom, which is capable of breathing simulation, and suitable for gating techniques of the MR-Linac. Despite small planning errors, the experiment showcases the capabilities of the phantom for refining radiation therapy procedures and provides a novel setup to further investigate new treatment methods that consider organ motion during respiration. These findings contribute to ongoing progress in the field of medical imaging, radiation therapy, and medical physics, providing a valuable asset for advancing research and patient care.

## 6 Summary

The continuous progress in the field of radiation therapy has led to significant improvements in the diagnosis and treatment of cancer, resulting in enhanced quality of life and increased life expectancy. The development of the MR-Linac marked a paradigm shift in radiation therapy. This advancement enables real-time visualization of tumors during radiation therapy using magnetic resonance imaging. Consequently, treatment plans can be adjusted to account for changes in tumor size between sessions, such as tumor shrinkage, and to incorporate tumor movements during each radiation session, for example, due to breathing. This precision allows for the delivery of a higher radiation dose directly to the target volume while minimizing radiation exposure to nearby organs.

The aim of this work was to develop an anthropomorphic abdominal phantom that meets several requirements: reproducible breathing motions with induced organ motions in a composite, realistic image contrast in both magnetic resonance imaging and computed tomography, anthropomorphically shaped organ models, and an MRI-compatible motion control unit.

In this thesis, an innovative anthropomorphic abdominal phantom for medical imaging and radiation therapy applications was developed. Through a series of experiments and analyses, the capabilities and usefulness of the phantom were rigorously evaluated.

The organ models used in the experiments demonstrate remarkable accuracy in replicating the relaxation times and Hounsfield Units of real human organs. This validation underscores the suitability of the phantom for medical imaging research, with the results showing close agreement with reference values without significant differences.

Comparisons between the phantom and patient/volunteer data showed good agreement in simulating respiration-induced organ motions in a composite during various breathing patterns (shallow, free, and deep breathing), anatomical shapes, image contrast, and radiological characteristics.

Furthermore, the analysis of organ motion under different breathing patterns highlights the phantom's ability to simulate human organ movements, emphasizing the importance of considering organ motions in treatment planning and imaging procedures.

In summary, this work demonstrated that the developed phantom effectively simulates various respiratory movements and corresponding organ motions within a composite structure. Additionally, compared to volunteer data, the phantom exhibited comparable image contrast in magnetic resonance imaging and computed tomography imaging, and stability of image contrast over a period of more than 400 days was demonstrated. Moreover, the phantom proved

suitable for an end-to-end test, encompassing the entire radiation therapy process from imaging and radiation planning to dose calculation and delivery. This included the insertion of dosimetric EBT3 films into the liver tumor model. An important outcome was that the phantom's liver tumor model was successfully detected by the MR-Linac and radiation was stopped as soon as the tumor moved outside the target volume due to breathing motion. Ultimately, a dose of  $5.3 \pm 0.42$  Gy was calculated within the tumor model, which demonstrates excellent alignment with the planned dose of 5 Gy, considering the minimal deviation.

## Zusammenfassung

Der kontinuierliche Fortschritt auf dem Gebiet der Strahlentherapie hat zu erheblichen Verbesserungen bei der Diagnose und Behandlung von Krebs geführt, was zu einer verbesserten Lebensqualität und einer erhöhten Lebenserwartung führt. Die Entwicklung des MR-Linac markierte daher einen Paradigmenwechsel in der Strahlentherapie. Diese Weiterentwicklung ermöglicht die Echtzeit-Visualisierung von Tumoren während der Strahlentherapie mittels Magnetresonanztomographie. Folglich können Behandlungspläne angepasst werden, um Veränderungen in der Tumorgöße zwischen den Sitzungen, wie Tumorverkleinerung, zu berücksichtigen, und um Tumorbewegungen während jeder Strahlungssitzung, beispielsweise aufgrund von Atmung, einzubeziehen. Diese Präzision ermöglicht die Verabreichung einer höheren Strahlendosis direkt an das Zielvolumen, während die Strahlenexposition für nahegelegene Organe minimiert wird.

Das Ziel dieser Arbeit war es, ein anthropomorphes abdominal Phantom zu entwickeln, welches mehreren Anforderungen gerecht werden muss: reproduzierbare Atembewegungen mit induzierten Organbewegungen im Verbund, realistischer Bildkontrast sowohl in der Magnetresonanztomographie als auch in der Computertomographie, anthropomorph geformte Organmodelle und eine Magnetresonanztomographie-kompatible Bewegungssteuerung.

Im Rahmen dieser Arbeit wurde ein innovatives anthropomorphes abdominales Phantom für medizinische Bildgebung und Strahlentherapieanwendungen entwickelt. Durch eine Reihe von Experimenten und Analysen wurden die Fähigkeiten und die Nützlichkeit des Phantoms rigoros bewertet.

Die in den Experimenten verwendeten Organmodelle zeigen eine bemerkenswerte Genauigkeit bei der Nachbildung der Relaxationszeiten und Hounsfield-Units realer menschlicher Organe. Diese Validierung unterstreicht die Eignung des Phantoms für die medizinische Bildgebungsforschung, dabei zeigen die Ergebnisse eine enge Übereinstimmung mit Referenzwerten ohne signifikante Unterschiede.

Vergleiche zwischen dem Phantom und Patienten-/Probandendaten zeigten eine gute Übereinstimmung bei der Simulation von ateminduzierten Organbewegungen in einem Verbund während verschiedener Atemmuster (flaches, freies und tiefes Atmen), anatomischer Formen, Kontrast in der Bildgebung und radiologischer Eigenschaften.

Darüber hinaus unterstreicht die Analyse der Organbewegung unter verschiedenen Atemmustern die Fähigkeit des Phantoms, menschliche Organbewegungen zu simulieren, was die Bedeutung der Berücksichtigung von Organbewegungen bei der Behandlungsplanung und Bildgebungsverfahren unterstreicht.

Zusammenfassend zeigte diese Arbeit, dass das entwickelte Phantom verschiedene Atembewegungen und entsprechende Organbewegungen innerhalb einer Verbundstruktur effektiv simuliert. Darüber hinaus wies das Phantom im Vergleich zu Probandendaten einen vergleichbaren Bildkontrast in der Magnetresonanztomographie und Computertomographie Bildgebung aus und zusätzlich konnte die Stabilität des Bildkontrasts über einen Zeitraum von mehr als 400 Tagen nachgewiesen werden. Darüber hinaus erwies sich das Phantom als geeignet für einen End-to-End-Test, der den gesamten Strahlentherapieprozess von der Bildgebung und Strahlungsplanung bis hin zur Dosisberechnung und -verabreichung umfasste. Dies beinhaltete das Einsetzen von dosimetrischen EBT3-Filmen in das Lebertumormodell. Ein wichtiges Ergebnis war, dass das Lebertumormodell des Phantoms erfolgreich vom MR-Linac erkannt wurde und die Bestrahlung stoppte, sobald der Tumor aufgrund der Atembewegung das Zielvolumen verließ. Letztendlich wurde eine Dosis von  $5,3 \pm 0,42$  Gy innerhalb des Tumormodells berechnet, was eine ausgezeichnete Übereinstimmung mit der geplanten Dosis von 5 Gy darstellt, unter Berücksichtigung der minimalen Abweichung.

## 7 Bibliography

- Bazelaire, Cedric M. J. de; Duhamel, Guillaume D.; Rofsky, Neil M.; Alsop, David C. (2004): MR imaging relaxation times of abdominal and pelvic tissues measured in vivo at 3.0 T: preliminary results. In: *Radiology* 230 (3), S. 652–659. DOI: 10.1148/radiol.2303021331.
- Bostel, Tilman; Pfaffenberger, Asja; Delorme, Stefan; Dreher, Constantin; Echner, Gernot; Haering, Peter et al. (2018): Prospektive Machbarkeitsstudie eines neuen Offline-Ansatzes für die MR-geführte Radiotherapie. In: *Strahlenther Onkol* 194 (5), S. 425–434. DOI: 10.1007/s00066-017-1258-y.
- Brandner, Edward D.; Wu, Andrew; Chen, Hungcheng; Heron, Dwight; Kalnicki, Shalom; Komanduri, Krishna et al. (2006): Abdominal organ motion measured using 4D CT. In: *International journal of radiation oncology, biology, physics* 65 (2), S. 554–560. DOI: 10.1016/j.ijrobp.2005.12.042.
- Brown, Robert W.; Cheng, Yu-Chung N.; Haacke, E. Mark; Thompson, Michael R.; Venkatesan, Ramesh (2014): *Magnetic resonance imaging. Physical principles and sequence design*. Second edition. Hoboken, New Jersey: John Wiley & Sons, Inc.
- Bushong, Stewart C. (2003): *Magnetic resonance imaging. Physical and biological principles*. 3rd edition. St. Louis: Mosby.
- Caillet, Vincent; Booth, Jeremy T.; Keall, Paul (2017): IGRT and motion management during lung SBRT delivery. In: *Physica medica : PM : an international journal devoted to the applications of physics to medicine and biology : official journal of the Italian Association of Biomedical Physics (AIFB)* 44, S. 113–122. DOI: 10.1016/j.ejmp.2017.06.006.
- Chen, S. N.; Gauthier, M.; Bazalova-Carter, M.; Bolanos, S.; Glenzer, S.; Riquier, R. et al. (2016): Absolute dosimetric characterization of Gafchromic EBT3 and HDv2 films using commercial flat-bed scanners and evaluation of the scanner response function variability. In: *The Review of scientific instruments* 87 (7), S. 73301. DOI: 10.1063/1.4954921.
- CIRS (2021): Triple Modality 3D Abdominal Phantom - CIRS. Online verfügbar unter <https://www.cirsinc.com/products/all/65/triple-modality-3d-abdominal-phantom/>, zuletzt aktualisiert am 02.07.2021, [Stand 09.01.2024].
- Decker, Georges; Mürtz, Petra; Gieseke, Jürgen; Träber, Frank; Block, Wolfgang; Sprinkart, Alois M. et al. (2014): Intensity-modulated radiotherapy of the prostate: dynamic ADC monitoring by DWI at 3.0 T. In: *Radiotherapy and oncology : journal of the European Society for Therapeutic Radiology and Oncology* 113 (1), S. 115–120. DOI: 10.1016/j.radonc.2014.07.016.

DeWerd, Larry A.; Kissick, Michael (Hg.) (2014a): The Phantoms of medical and health physics. Devices for research and development. New York, NY, Heidelberg, Dordrecht, London: Springer (Biological and Medical Physics, Biomedical Engineering).

DeWerd, Larry A.; Kissick, Michael (Hg.) (2014b): The Phantoms of Medical and Health Physics. Devices for Research and Development. New York, NY: Springer New York (SpringerLink Bücher). Online verfügbar unter <http://swbplus.bsz-bw.de/bsz398197601cov.htm>.

Dhont, J.; Harden, S. V.; Chee, L. Y. S.; Aitken, K.; Hanna, G. G.; Bertholet, J. (2020): Image-guided Radiotherapy to Manage Respiratory Motion: Lung and Liver. In: Clinical oncology (Royal College of Radiologists (Great Britain)) 32 (12), S. 792–804. DOI: 10.1016/j.clon.2020.09.008.

Drake, Richard L.; Vogl, Wayne; Mitchell, Adam W. M. (2021): Gray's atlas of anatomy. Third edition, international edition. Philadelphia, PA: Elsevier.

Elter, A.; Hellwich, E.; Dorsch, S.; Schäfer, M.; Runz, A.; Klüter, S. et al. (2021): Development of phantom materials with independently adjustable CT- and MR-contrast at 0.35, 1.5 and 3 T. In: Physics in medicine and biology 66 (4), S. 45013. DOI: 10.1088/1361-6560/abd4b9.

Filippou, Valeria; Tsoumpas, Charalampos (2018): Recent advances on the development of phantoms using 3D printing for imaging with CT, MRI, PET, SPECT, and ultrasound. In: Medical physics 45 (9). DOI: 10.1002/mp.13058.

Gill, S.; Li, J.; Thomas, J.; Bressel, M.; Thursky, K.; Styles, C. et al. (2012): Patient-reported complications from fiducial marker implantation for prostate image-guided radiotherapy. In: BJR 85 (1015), S. 1011–1017. DOI: 10.1259/bjr/68127917.

Gosling, J. A. (2008): Human anatomy. Color atlas and textbook. 5th ed. [Edinburgh]: Mosby/Elsevier.

Hannah Ritchie; Max Roser (2023): Causes of Death. In: Our World in Data. Online verfügbar unter <https://ourworldindata.org/causes-of-death#citation> [Stand: 20.03.2024].

Hashemi, Ray H.; Bradley, William G.; Lisanti, Christopher J. (2018a): MRI. The basics. Fourth edition. Philadelphia: Wolters Kluwer Health. Online verfügbar unter <https://search.ebscohost.com/login.aspx?direct=true&scope=site&db=nlebk&db=nlabk&AN=2013143> [Stand: 03.2024].

Hashemi, Ray H.; Bradley, William G.; Lisanti, Christopher J. (2018b): MRI. The basics. Fourth edition. Philadelphia: Wolters Kluwer Health. Online verfügbar unter <https://search.ebscohost.com/login.aspx?direct=true&scope=site&db=nlebk&db=nlabk&AN=2013143> [Stand: 03.2024].

- Henke, L. E.; Contreras, J. A.; Green, O. L.; Cai, B.; Kim, H.; Roach, M. C. et al. (2018): Magnetic Resonance Image-Guided Radiotherapy (MRIgRT): A 4.5-Year Clinical Experience. In: *Clinical oncology (Royal College of Radiologists (Great Britain))* 30 (11), S. 720–727. DOI: 10.1016/j.clon.2018.08.010.
- Hsieh, Jiang (2015): *Computed Tomography: Principles, Design, Artifacts, and Recent Advances*: SPIE PRESS.
- Jiang, Steve B. (2006): Technical aspects of image-guided respiration-gated radiation therapy. In: *Medical dosimetry : official journal of the American Association of Medical Dosimetrists* 31 (2), S. 141–151. DOI: 10.1016/j.meddos.2005.12.005.
- Jong, Tonke L. de; Moelker, Adriaan; Dankelman, Jenny; van den Dobbelsteen, John J. (2019): Designing and validating a PVA liver phantom with respiratory motion for needle-based interventions. In: *International journal of computer assisted radiology and surgery* 14 (12), S. 2177–2186. DOI: 10.1007/s11548-019-02029-6.
- Kang, Sang-Won; Chung, Jin-Beom; Kim, Kyeong-Hyeon; Eom, Keun-Yong; Song, Changhoon; Lee, Jeong-Woo et al. (2017): Evaluation of Dual-channel Compound Method for EBT3 Film Dosimetry. In: *Prog Med Phys* 28 (1), S. 16. DOI: 10.14316/pmp.2017.28.1.16.
- Keall, Paul J.; Mageras, Gig S.; Balter, James M.; Emery, Richard S.; Forster, Kenneth M.; Jiang, Steve B. et al. (2006): The management of respiratory motion in radiation oncology report of AAPM Task Group 76. In: *Medical physics* 33 (10), S. 3874–3900. DOI: 10.1118/1.2349696.
- Khachonkham, Suphalak; Dreindl, Ralf; Heilemann, Gerd; Lechner, Wolfgang; Fuchs, Hermann; Palmans, Hugo et al. (2018): Characteristic of EBT-XD and EBT3 radiochromic film dosimetry for photon and proton beams. In: *Physics in medicine and biology* 63 (6), S. 65007. DOI: 10.1088/1361-6560/aab1ee.
- Kim, Young Seok; Park, Sung Ho; Ahn, Seung Do; Lee, Jeong Eun; Choi, Eun Kyung; Lee, Sang-wook et al. (2007): Differences in abdominal organ movement between supine and prone positions measured using four-dimensional computed tomography. In: *Radiotherapy and Oncology* 85 (3), S. 424–428. DOI: 10.1016/j.radonc.2007.10.031.
- Kirilova, Anna; Lockwood, Gina; Choi, Perry; Bana, Neelufer; Haider, Masoom A.; Brock, Kristy K. et al. (2008): Three-dimensional motion of liver tumors using cine-magnetic resonance imaging. In: *International Journal of Radiation Oncology\*Biophysics* 71 (4), S. 1189–1195. DOI: 10.1016/j.ijrobp.2007.11.026.
- Klüter, Sebastian (2019): Technical design and concept of a 0.35 T MR-Linac. In: *Clinical and translational radiation oncology* 18, S. 98–101. DOI: 10.1016/j.ctro.2019.04.007.

- Korin, H. W.; Ehman, R. L.; Riederer, S. J.; Felmlee, J. P.; Grimm, R. C. (1992): Respiratory kinematics of the upper abdominal organs: a quantitative study. In: *Magnetic resonance in medicine* 23 (1), S. 172–178. DOI: 10.1002/mrm.1910230118.
- Korreman, S. S. (2015): Image-guided radiotherapy and motion management in lung cancer. In: *BJR* 88 (1051), S. 20150100. DOI: 10.1259/bjr.20150100.
- Kostiukhina, Natalia; Georg, Dietmar; Rollet, Sofia; Kuess, Peter; Sipaj, Andrej; Andrzejewski, Piotr et al. (2017): Advanced Radiation DOSimetry phantom (ARDOS): a versatile breathing phantom for 4D radiation therapy and medical imaging. In: *Physics in medicine and biology* 62 (20), S. 8136–8153. DOI: 10.1088/1361-6560/aa86ea.
- Kubiak, Tomasz (2016): Particle therapy of moving targets-the strategies for tumour motion monitoring and moving targets irradiation. In: *The British journal of radiology* 89 (1066), S. 20150275. DOI: 10.1259/bjr.20150275.
- Kurz, Christopher; Buizza, Giulia; Landry, Guillaume; Kamp, Florian; Rabe, Moritz; Paganelli, Chiara et al. (2020): Medical physics challenges in clinical MR-guided radiotherapy. In: *Radiat Oncol* 15 (1), S. 93. DOI: 10.1186/s13014-020-01524-4.
- Lamba, Ramit; McGahan, John P.; Corwin, Michael T.; Li, Chin-Shang; Tran, Tien; Seibert, J. Anthony; Boone, John M. (2014): CT Hounsfield numbers of soft tissues on unenhanced abdominal CT scans: variability between two different manufacturers' MDCT scanners. In: *AJR. American journal of roentgenology* 203 (5), S. 1013–1020. DOI: 10.2214/AJR.12.10037.
- Liao, Yuliang; Wang, Linjing; Xu, Xiangdong; Chen, Haibin; Chen, Jiawei; Zhang, Guoqian et al. (2017): An anthropomorphic abdominal phantom for deformable image registration accuracy validation in adaptive radiation therapy. In: *Medical physics* 44 (6), S. 2369–2378. DOI: 10.1002/mp.12229.
- Mann, P.; Witte, M.; Moser, T.; Lang, C.; Runz, A.; Johnen, W. et al. (2017): 3D dosimetric validation of motion compensation concepts in radiotherapy using an anthropomorphic dynamic lung phantom. In: *Physics in medicine and biology* 62 (2), S. 573–595. DOI: 10.1088/1361-6560/aa51b1.
- Marroquin, Elsa Y. León; Herrera González, José A.; Camacho López, Miguel A.; Barajas, José E. Villarreal; García-Garduño, Olivia A. (2016): Evaluation of the uncertainty in an EBT3 film dosimetry system utilizing net optical density. In: *J Appl Clin Med Phys* 17 (5), S. 466–481. DOI: 10.1120/jacmp.v17i5.6262.
- Matrosic, Charles K.; Bednarz, Bryan; Culberson, Wesley (2020): An improved abdominal phantom for intrafraction image guidance validation. In: *Physics in medicine and biology* 65 (13), 13NT02. DOI: 10.1088/1361-6560/ab9456.

- Matrosic, Charles K.; Hull, Jennifer; Palmer, Benjamin; Culberson, Wesley; Bednarz, Bryan (2019): Deformable abdominal phantom for the validation of real-time image guidance and deformable dose accumulation. In: *J Appl Clin Med Phys* 20 (8), S. 122–133. DOI: 10.1002/acm2.12687.
- Modus QA (2021): Modus QA. QUASAR™ MRI<sup>4D</sup> Motion Phantom. Online verfügbar unter <https://modusqa.com/products/quasar-mri4d-motion-phantom/>, zuletzt geprüft am [Stand: 29.10.2021].
- Moerland, M. A.; van den Bergh, A.C.M.; Bhagwandien, R.; Janssen, W. M.; Bakker, C.J.G.; Legendijk, J.J.W.; Battermann, J. J. (1994): The influence of respiration induced motion of the kidneys on the accuracy of radiotherapy treatment planning, a magnetic resonance imaging study. In: *Radiotherapy and Oncology* 30 (2), S. 150–154. DOI: 10.1016/0167-8140(94)90045-0.
- Mutic, Sasa; Dempsey, James F. (2014): The ViewRay system: magnetic resonance-guided and controlled radiotherapy. In: *Seminars in radiation oncology* 24 (3), S. 196–199. DOI: 10.1016/j.semradonc.2014.02.008.
- Netter, Frank H. (2014): *Atlas of human anatomy. Sixth edition. 25 anniversary edition.* Philadelphia, PA: Saunders; Saunders/Elsevier (Netter Basic Science).
- Niebuhr, N. I.; Johnen, W.; Echner, G.; Runz, A.; Bach, M.; Stoll, M. et al. (2019): The ADAM-pelvis phantom—an anthropomorphic, deformable and multimodal phantom for MRgRT. In: *Phys. Med. Biol.* 64 (4), 04NT05. DOI: 10.1088/1361-6560/aafd5f.
- Niroomand-Rad, Azam; Chiu-Tsao, Sou-Tung; Grams, Michael P.; Lewis, David F.; Soares, Christopher G.; van Battum, Leo J. et al. (2020): Report of AAPM Task Group 235 Radiochromic Film Dosimetry: An Update to TG-55. In: *Medical physics* 47 (12), S. 5986–6025. DOI: 10.1002/mp.14497.
- Noel, Camille E.; Parikh, Parag J.; Spencer, Christopher R.; Green, Olga L.; Hu, Yanle; Mutic, Sasa; Olsen, Jeffrey R. (2015): Comparison of onboard low-field magnetic resonance imaging versus onboard computed tomography for anatomy visualization in radiotherapy. In: *Acta oncologica (Stockholm, Sweden)* 54 (9), S. 1474–1482. DOI: 10.3109/0284186X.2015.1062541.
- Nolden, Marco; Zelzer, Sascha; Seitel, Alexander; Wald, Diana; Müller, Michael; Franz, Alfred M. et al. (2013): The Medical Imaging Interaction Toolkit: challenges and advances : 10 years of open-source development. In: *International journal of computer assisted radiology and surgery* 8 (4), S. 607–620. DOI: 10.1007/s11548-013-0840-8.
- Pallotta, Stefania; Calusi, Silvia; Masi, Laura; Talamonti, Cinzia; Marrazzo, Livia; Foggi, Leonardo et al. (2019): ADAM phantom to test 4D medical imaging and dose delivery devices. In: *Physics in medicine and biology* 64 (10), S. 105002. DOI: 10.1088/1361-6560/ab1a49.

Pelc, Norbert J. (2014): Recent and future directions in CT imaging. In: *Annals of biomedical engineering* 42 (2), S. 260–268. DOI: 10.1007/s10439-014-0974-z.

Raaymakers, B. W.; Jürgenliemk-Schulz, I. M.; Bol, G. H.; Glitzner, M.; Kotte, A. N. T. J.; van Asselen, B. et al. (2017): First patients treated with a 1.5 T MRI-Linac: clinical proof of concept of a high-precision, high-field MRI guided radiotherapy treatment. In: *Physics in medicine and biology* 62 (23), L41-L50. DOI: 10.1088/1361-6560/aa9517.

Raaymakers, B. W.; Lagendijk, J. J. W.; Overweg, J.; Kok, J. G. M.; Raaijmakers, A. J. E.; Kerkhof, E. M. et al. (2009): Integrating a 1.5 T MRI scanner with a 6 MV accelerator: proof of concept. In: *Physics in medicine and biology* 54 (12), N229-37. DOI: 10.1088/0031-9155/54/12/N01.

Reiser, Maximilian F.; Semmler, Wolfhard; Hricak, Hedvig (2008): *Magnetic Resonance Tomography*. Berlin, Heidelberg: Springer Berlin Heidelberg.

RKI (2023): RKI – Krebs in Deutschland – 2019/2020. Online verfügbar unter [https://www.krebsdaten.de/Krebs/DE/Content/Publikationen/Krebs\\_in\\_Deutschland/krebs\\_in\\_deutschland\\_2023.pdf?\\_\\_blob=publicationFile](https://www.krebsdaten.de/Krebs/DE/Content/Publikationen/Krebs_in_Deutschland/krebs_in_deutschland_2023.pdf?__blob=publicationFile), zuletzt geprüft am 08.03.2024.

RSD Breathing Phantom (2024). Online verfügbar unter <http://www.pnwx.com/Accessories/Phantoms/CT/RSD/Respiring/>, zuletzt aktualisiert am 09.01.2024, zuletzt geprüft am [Stand: 09.01.2024].

Schindelin, Johannes; Arganda-Carreras, Ignacio; Frise, Erwin; Kaynig, Verena; Longair, Mark; Pietzsch, Tobias et al. (2012): Fiji: an open-source platform for biological-image analysis. In: *Nature methods* 9 (7), S. 676–682. DOI: 10.1038/nmeth.2019.

Schulthess, Gustav K. von (2017): *Röntgen, Computertomografie & Co. Wie funktioniert medizinische Bildgebung?* 1. Auflage. Berlin, Heidelberg: Springer Berlin Heidelberg (Springer eBook Collection Medicine). Online verfügbar unter <http://swbplus.bsz-bw.de/bsz48216543xcov.htm> [Stand: 09.02.2021].

Shah, Amish P.; Kupelian, Patrick A.; Waghorn, Benjamin J.; Willoughby, Twyla R.; Rineer, Justin M.; Mañon, Rafael R. et al. (2013): Real-time tumor tracking in the lung using an electromagnetic tracking system. In: *International journal of radiation oncology, biology, physics* 86 (3), S. 477–483. DOI: 10.1016/j.ijrobp.2012.12.030.

Siemens Healthcare GmbH (2021): Siemens Somatom Force. Online verfügbar unter <https://www.siemens-healthineers.com/de-ch/computed-tomography/dual-source-ct/somatom-force>, [Stand: 08.11.2021].

Testphantom für Strahlentherapie - RS-1500 - Radiology Support Devices - Oberkörper (2024). Online verfügbar unter <https://www.medicalexpo.de/prod/radiology-support-devices/product-97853-718042.html>, zuletzt aktualisiert am 09.01.2024, [Stand: 09.01.2024].

The Diaphragm - Actions - Innervation - TeachMeAnatomy. Dynamic Anatomical Respiring Humanoid Phantom (2022). Online verfügbar unter <https://teachmeanatomy.info/thorax/muscles/diaphragm/>, zuletzt aktualisiert am 29.06.2022, [Stand: 29.06.2022].

Thiyagarajan, Rajesh; Sinha, Sujit Nath; Ravichandran, Ramamoorthy; Samuvel, Kothandaraman; Yadav, Girigesh; Sigamani, Ashok Kumar et al. (2016): Respiratory gated radiotherapy-pretreatment patient specific quality assurance. In: *Journal of Medical Physics / Association of Medical Physicists of India* 41 (1), S. 65–70. DOI: 10.4103/0971-6203.177279.

Thorwarth, Daniela; Low, Daniel A. (2021): Technical Challenges of Real-Time Adaptive MR-Guided Radiotherapy. In: *Front. Oncol.* 11, S. 634507. DOI: 10.3389/fonc.2021.634507.

Tino, Rance; Yeo, Adam; Leary, Martin; Brandt, Milan; Kron, Tomas (2019): A Systematic Review on 3D-Printed Imaging and Dosimetry Phantoms in Radiation Therapy. In: *Technol Cancer Res Treat* 18, 153303381987020. DOI: 10.1177/1533033819870208.

Tofts, P. S.; Shuter, B.; Pope, J. M. (1993): Ni-DTPA doped agarose gel—A phantom material for Gd-DTPA enhancement measurements. In: *Magnetic Resonance Imaging* 11 (1), S. 125–133. DOI: 10.1016/0730-725X(93)90420-I.

University of Sulaimani / College of Medicine (2017): Anatomy of the Thoracic Cavity & Diaphragm. Video: Ahmad Jabar. Online verfügbar unter [https://www.youtube.com/watch?v=\\_\\_bQ7Zo2SjMk](https://www.youtube.com/watch?v=__bQ7Zo2SjMk), [Stand: 20.03.2024].

Weidner, Artur; Stengl, Christina; Dinkel, Fabian; Dorsch, Stefan; Murillo, Carlos; Seeber, Steffen et al. (2022): An abdominal phantom with anthropomorphic organ motion and multimodal imaging contrast for MR-guided radiotherapy. In: *Physics in medicine and biology* 67 (4), S. 45009. DOI: 10.1088/1361-6560/ac4ef8.

Weishaupt, Dominik; Köchli, Victor D.; Marincek, Borut (2006): *How Does MRI Work? An Introduction to the Physics and Function of Magnetic Resonance Imaging*. Second edition. Berlin, Heidelberg: Springer Berlin Heidelberg (SpringerLink : Bücher).

Wen, Ning; Lu, Siming; Kim, Jinkoo; Qin, Yujiao; Huang, Yimei; Zhao, Bo et al. (2016): Precise film dosimetry for stereotactic radiosurgery and stereotactic body radiotherapy quality assurance using Gafchromic™ EBT3 films. In: *Radiat Oncol* 11 (1), S. 132. DOI: 10.1186/s13014-016-0709-4.



## 8 Appendix

### 8.1 List of Publications

The following publications were published during this work.

#### Published papers:

- C. Stengl, K. Panow, E. Arbes, I.D. Muñoz, J.B. Christensen, C. Neelsen, F. Dinkel, **A. Weidner**, A. Runz, W. Johnen, J. Liermann, G. Echner, J. Vedelago and O. Jäkel. „A phantom to simulate organ motion and its effect on dose distribution in carbon ion therapy for pancreatic cancer.” *Physics in Medicine & Biology* (2023), <https://doi.org/10.1088/1361-6560/ad0902>
- **Artur Weidner**, Christina Stengl, Fabian Dinkel, Stefan Dorsch, Carlos Murillo, Steffen Seeber, Regula Gnirs, Armin Runz, Gernot Echner, Christian P. Karger, Oliver Jäkel. “An abdominal phantom with anthropomorphic organ motion and multimodal imaging contrast for MR-guided radiotherapy.” *Physics in Medicine & Biology* (2022), <https://doi.org/10.1088/1361-6560/ac4ef8>
- C. Stengl, S. Ghafoory, **A. Weidner**, B. Murphy, S. Wöfl. “Development of an Artificial 3D Liver Phantom for Analysis of Radiotherapeutic Effects In Vitro.” *Applied Sciences* (2022), <https://doi.org/10.3390/app122110867>

#### Conference contributions as first author:

- Presentation: **A. Weidner**, C. Stengl, F. Dinkel, S. Dorsch, A. Runz, G. Echner. „Development of an anthropomorphic real-time breathing phantom for image-guided radiotherapy.” *Joint Conference of the ÖGMP, DGMP & SGSMF Dreiländertagung der Medizinischen Physik*, virtual conference (2021)
- Poster Presentation: **A. Weidner**, C. Stengl, F. Dinkel, A. Runz, G. Echner. „Multimodal anthropomorphic abdomen phantom with real-time breathing motion for IGRT.” *40<sup>th</sup> European Society for Radiotherapy and Oncology (ESTRO)*, virtual conference (2021)

- Presentation: **A. Weidner**, T. Buening, A. Runz, G. Echner.” Multimodal anthropomorphic abdomen phantom with real-time breathing motion for IGRT.” *39<sup>th</sup> European Society for Radiotherapy and Oncology (ESTRO)*, virtual conference (2020)
- Presentation: **A. Weidner**, T. Buening, A. Runz, G. Echner. “ Anthropomorphes abdominal Phantom für multimodale Bildgebung und MR-bildgestützte Strahlentherapie.” *DGMP 50. Jahrestagung Deutsche Gesellschaft für Medizinische Physik*, Stuttgart (2019)
- Poster Presentation: **A. Weidner**, A. Runz, W. Johnen G. Echner. ” Development of an anthropomorphic lung phantom for imaging and radiotherapy.” *38<sup>th</sup> European Society for Radiotherapy and Oncology (ESTRO)*, Milano (2019)
- Poster Presentation: **A. Weidner**, T. Buening, A. Runz, G. Echner. “Development of an anthropomorphic abdominal 4D Phantom for multimodal imaging and MR-guided Radiotherapy.” *DKFZ PhD Poster Presentation Heidelberg* (2019)
- Poster Presentation: **A. Weidner**, T. Buening, A. Runz, G. Echner. “Development of an anthropomorphic abdominal 4D Phantom.” *National Center for tumor diseases (NCT) Retreat*, Heidelberg and Dresden (2019)

## 8.2 List of Figures

Figure 1: Anthropomorphic phantoms.....	9
Figure 2: Construction image of the deformable abdominal phantom .....	10
Figure 3: Plastinated diaphragm anatomy .....	19
Figure 4: Linear stage unit for motion control.....	24
Figure 5: Motion control setup.....	26
Figure 6: Phantom container and organ models.....	27
Figure 7: Casting molds were designed with CAD.....	29
Figure 8: Manufacturing of organ models.....	30
Figure 9: The pelvis with attached lumbar spine model .....	31
Figure 10: Phantom container filling and organ placement.....	32
Figure 11: Markings on the organ models and the phantom container.....	33
Figure 12: Organ placement .....	34
Figure 13: Phantom with attached adapter and diaphragm-shaped actuator.....	35
Figure 14: Third experimental setup.....	38
Figure 15: Liver casting mold with tumor model .....	40
Figure 16: Manufacturing of the spherical tumor model .....	41
Figure 17: Saturation recovery and multi-spin-echo sequence.....	44
Figure 18: Orientation and slices that were acquired with the cine sequence .....	45
Figure 19: Example of acquired image data in the coronal plane .....	46
Figure 20: Axial, sagittal, and coronal slices of CT patient data.....	49
Figure 21: Sagittal slice of the acquired volunteer cine sequence MRI data .....	50
Figure 22: Quantitative T1 weighted images of the contrast phantom.....	52
Figure 23: Illustration of ion exchange.....	52
Figure 24: Phantom to investigate contrast stability over a period of time.....	53
Figure 25; Qualitative T1w (A) and T2w images of OEAMs and AMs.....	57
Figure 26: Relaxation time stability over a period of time for all organ models .....	59
Figure 27: Comparison between the T1, T2 and HU values.....	62
Figure 28: Comparison of axial and coronal CT scans between patient and phantom.....	64
Figure 29: Comparison of axial and coronal T1w MRI scans.....	65
Figure 30: Comparison of axial and coronal T2w MRI scans.....	66
Figure 31: Motion amplitude of the phantom’s liver and kidneys .....	68
Figure 32: Comparison between second experimental setup and volunteer.....	70
Figure 33: Comparison between the first and second experimental setup. ....	71
Figure 34: Movement trajectories of each organ model in cc direction. ....	72
Figure 35: Comparison between phantom and volunteer for free breathing. ....	73
Figure 36: Comparison of the LDRM, KDMR, SDMR and the PDMR.....	74
Figure 37: Comparison of the bin1 to bin 5 for the different organs.....	75
Figure 38: Treatment plan.....	77
Figure 39: The abdominal phantom is positioned on the patient couch.....	78
Figure 40 Irradiation of the tumor model using gating at the MR-Linac.....	79
Figure 41: EBT3 Film irradiation with different dose.....	79
Figure 42: Calculated calibration curve.....	80

Figure 43: Evaluated offset value.....	81
Figure 44: A 13 x 13 mm ROI is placed in the middle of the tumor ET3 film.....	81
Figure 45: Evaluation of detected bins for deep breathing. ....	88

### 8.3 List of Tables

Table 1: Comparison between different phantoms and their properties. ....	12
Table 2: Organ displacement measured in different studies .....	22
Table 3: Chemical composition of liver, kidney, spleen, pancreas and vertebrae models .....	28
Table 4: Overview of the different experimental setup versions.....	37
Table 5: Comparison of T1 and T2 relaxation times for 1.5 T and 3.0 T .....	60
Table 6: Comparison of T1 and T2 relaxation times for 1.5T and 3.0T.....	61
Table 7: Comparison of diaphragm, liver and kidney motion amplitudes .....	67
Table 8: Comparison of diaphragm, liver, kidneys, spleen and pancreas motion .....	70

## 8.4 List of Abbreviations

RT	Radiation therapy
OAR	Organs at risk
3D	Three-dimensional
CT	Computed tomography
MRI	Magnetic resonance imaging
IGRT	Image-guided radiation therapy
CTV	Clinical target volume
ITV	Internal target volume
PTV	Planning target volume
ART	Adaptive radiotherapy
MR-Linac	Magnetic resonance linear accelerator (combination of an MRI scanner and a linear accelerator)
MR	Magnetic resonance
MRgRT	Magnetic resonance guided radiation therapy
PVA	Polyvinyl alcohol
PVCP	Polyvinyl chloride plastisol
HU	Hounsfield unit
RF	Radio-frequency
DSCT	Dual source computer tomography
Linac	Linear accelerator
PLC	Programmable logic controller
FB	Function blocks
CSV	Comma-separated values
DICOM	Digital imaging and communications in medicine
MITK	Medical imaging interaction toolkit
CAD	Computer aided design
Ni-DTPA	Nickel (Ni) Diethylenetriaminepentaacetic Acid
KCl	potassium chloride
OD	Optical density
SR	Saturation recovery
TI	Inversion time
SE	Spin echo

TE	Echo time
PACS	picture archiving and communication system
4D	Four-dimensional
DKFZ	Deutsches Krebsforschungszentrum
GUI	Graphical user interface
ROI	Region of interest
COM	Center of mass
OEAM	Organ equivalent agarose mixture
AM	Agarose mixture
LDMR	Liver to diaphragm movement ratio
KDMR	Kidney to diaphragm movement ratio
SDMR	Spleen to diaphragm movement ratio
PDMR	Pancreas to diaphragm movement ratio
SEM	Standard error of mean
STD	Standard deviation



## **LEBENS LAUF**

### **PERSONALIEN:**

Name und Vorname: Weidner Artur  
Geburtsdatum: 08.12.1990  
Geburtsort: Stawropol, Russland  
Staatsangehörigkeit: deutsch

### **SCHULISCHER WERDEGANG:**

1997-1998 Grundschole Russland: Mbou Litsey 8 G.  
Stawropolya Im. N.g. Golodnikova  
1998 – 2001 Freihof Grundschole Kirchheim unter Teck  
2001 – 2010 Schlossgymnasium Kirchheim unter Teck  
24.06.2010 Abitur

### **UNIVERSITÄRER WERDEGANG:**

09/2011 – 02/2015 Studium der Medizintechnik (Bachelor of Science) an  
der Hochschule Mannheim in Kooperation mit der  
Universität Heidelberg  
02/2015 – 02/2018 Studium der Medizintechnik (Master of Science) an  
der Hochschule Mannheim

## EIDESSTATTLICHE VERSICHERUNG

Bei der eingereichten Dissertation zu dem Thema:

**An abdominal phantom with anthropomorphic organ motion and multimodal imaging contrast for magnetic-resonance-guided radiotherapy**

handelt es sich um meine eigenständig erbrachte Leistung.

Ich habe nur die angegebenen Quellen und Hilfsmittel benutzt und mich keiner unzulässigen Hilfe Dritter bedient. Insbesondere habe ich wörtlich oder sinngemäß aus anderen Werken übernommene Inhalte als solche kenntlich gemacht.

Die Arbeit oder Teile davon habe ich bislang nicht an einer Hochschule des In- oder Auslands als Bestandteil einer Prüfungs- oder Qualifikationsleistung vorgelegt.

Die Richtigkeit der vorstehenden Erklärungen bestätige ich.

Die Bedeutung der eidesstattlichen Versicherung und die strafrechtlichen Folgen einer unrichtigen oder unvollständigen eidesstattlichen Versicherung sind mir bekannt. Ich versichere an Eides statt, dass ich nach bestem Wissen die reine Wahrheit erklärt und nichts verschwiegen habe.

Ort und Datum

Unterschrift